Short- and Intermediate-Range Structures in $GeTe$-Sb_2Te_3 and Ag-$GeSe_3$ Glasses Studied by Anomalous X-Ray Scattering

Inaugural-Dissertation

zur Erlangung des

Doktorgrades der Naturwissenschaften

(Dr. rer. nat.)

dem Fachbereich Chemie

der Philipps-Universität Marburg

vorgelegt von

Jens Rüdiger Stellhorn, M.Sc.

aus Paderborn

Marburg, 2015

Einreichungstermin:	07.08.2015
Prüfungstermin:	17.09.2015
Erstgutachter:	Prof. Dr. Wolf-Christian Pilgrim
Zweitgutachter:	Prof. Dr. Bernd Harbrecht
Hochschulkennziffer:	1180

Einreichungstermin:	07.08.2015
Prüfungstermin:	17.09.2015
Erstgutachter:	Prof. Dr. Wolf-Christian Pilgrim
Zweitgutachter:	Prof. Dr. Bernd Harbrecht
Hochschulkennziffer:	1180

gewidmet meinen Eltern

dedicated to my parents

Abstract

The present dissertation describes the atomic structures of two systems of ternary chalcogenide glasses with the composition $Ag_x(GeSe_3)_{1-x}$ and $(GeTe)_{1-x}(Sb_2Te_3)_x$. To be able to gain new insight especially in the structures on intermediate length scales, the method of anomalous x-ray scattering (AXS) in combination with Reverse Monte Carlo modelling (RMC) is applied. The theoretical and experimental basis for the interpretation of the scattering data is given in the first part of the work, whereas the results of the experiment and the RMC modelling are presented and discussed in the second part.

Both systems under investigation are of distinct technological importance, hence reliable information on their structure is needed in order to contribute to the ongoing discussion about their structure-property relations. The results are presented within the framework of the various other investigations already published on these materials, and the possibilities and limitations of the different applied approaches are discussed.

Thereby, it is shown that important features of the materials, like the phase-change properties of the GeSbTe glasses and the superionic conductivity in the AgGeSe glasses, are closely connected not only to the near-, but also to the intermediate-range order in the amorphous structures.

Zusammenfassung

Die vorliegende Dissertation beschreibt die atomare Struktur von zwei Systemen ternärer Chalkogenid-Gläser mit der Zusammensetzung $Ag_x(GeSe_3)_{1-x}$ und $(GeTe)_{1-x}(Sb_2Te_3)_x$. Um neue Erkenntnisse besonders im Hinblick auf die Struktur auf intermediären Längenskalen zu erhalten, wird die Methode der anomalen Röntgenstreuung (AXS) in Kombination mit Reverse Monte Carlo-Simulationen (RMC) angewandt. Die theoretischen und experimentellen Grundlagen für die Interpretation der Messdaten werden im ersten Teil der Arbeit beschrieben, während die Ergebnisse der Experimente und der RMC-Simulationen im zweiten Teil präsentiert und interpretiert werden.

Beide betrachteten Systeme sind von besonderem technologischem Interesse, daher werden zuverlässige Informationen über ihre Struktur benötigt, um zur anhaltenden Diskussion über die Struktur-Eigenschafts-Beziehungen in diesen Materialien beizutragen. Die

Ergebnisse werden im Kontrast zu den diversen weiteren Arbeiten präsentiert, die zu diesen Materialien bereits publiziert worden sind, und die Möglichkeiten und Grenzen der verschiedenen verwendeten Ansätze werden erörtert.

Dadurch wird aufgezeigt, dass wichtige Materialeigenschaften, wie die Phasenwechsel-Eigenschaften der GeSbTe-Gläser und die superionische Leitfähigkeit in den AgGeSe-Gläsern, eng verknüpft sind sowohl mit der Nah- als auch mit der mittelreichweitigen Ordnung in den amorphen Strukturen.

Table of contents

I Theoretical and experimental basis **1**

1 Introduction **2**

2 Theoretical background **5**

2.1 Scattering experiments on disordered systems 5

2.2 Differential anomalous x-ray scattering 11

2.3 Reverse Monte Carlo Modelling 16

2.4 Structural hierarchy in amorphous systems 19

3 Experimental details **22**

3.1 Sample preparation 22

3.1.1 Ag-$GeSe_3$ glasses 22

3.1.2 GeTe-Sb_2Te_3 glasses 23

3.1.3 Sample container 24

3.2 Practical aspects of the AXS experiments 26

3.2.1 General considerations 27

3.2.2 Data reduction 29

3.2.3 Definition of the absorption edge 33

3.2.4 Analyzer specific corrections 34

3.3 Methodology 39

3.4 The AXS/RMC approach summarized 40

II Data evaluation and discussion **43**

4 Ag-$GeSe_3$ glasses **44**

4.1 Raw data and applied corrections 47

4.2 Reverse Monte Carlo Simulations on Ag-$GeSe_3$ 50

4.2.1 Partial structure factors 52

4.2.2 Partial pair correlation functions 54

4.2.3 Intermediate range order 59

4.2.4 Extended range order 64
4.3 Impact of the structure on the ion conduction mechanism 67

5 GeTe-Sb_2Te_3 glasses **69**
5.1 Raw data and applied corrections 72
5.1.1 Analyzer specific corrections 74
5.1.2 Structure from total measurements 77
5.2 Reverse Monte Carlo Simulations on GeSbTe glasses 80
5.2.1 Partial structure factors of the GeSbTe glasses 83
5.2.2 Partial pair correlation functions 86
5.2.3 Bond angle analysis 95
5.2.4 Intermediate range order 99
5.2.5 Comparison with AIMD results 106
5.3 Impact of the structure on the phase change properties 111
5.3.1 Temperature of the glass transition and crystallization 111
5.3.2 The optical contrast in GST 115
5.3.3 Crystallization time 117

6 Summary and outlook **119**

7 Appendix **123**

8 References **129**

List of Figures

1 Schematic view of the structural changes in Phase-Change Materials (PCMs) and the Programmable Metallization Cell (PMC). 3

2 Static and anomalous form factors for Ge and Se. 13

3 Weighting factors for $Ag_{0.15}(GeSe_3)_{0.85}$ for the total and differential $S(Q)$'s. 15

4 Extended-range order in $Ag_{0.50}(GeSe_3)_{0.50}$. 21

5 Photograph of an Ag-$GeSe_3$ sample. 23

6 Photograph of a GST sample with a thickness of about 1 μm, sputter-deposited on a glass substrate. 24

7 Exemplary graph of an EDX analysis of GeTe. 24

8 Raw data of GeTe measured with a Cu-K_α source. 25

9 Schematic representation of the sample container. 26

10 Schematic experimental setup for AXS experiments in transmission geometry. 27

11 Contribution of the Compton scattering to the overall scattered intensity and Compton energy in the case of GeTe. 31

12 Section of the analyzer scan at 9 $Å^{-1}$ at the Ge near edge of $Ag_{0.50}(GeSe_3)_{0.50}$, showing the contributions of inelastic scattering to the elastic peak. 32

13 Exemplary energy scans to define the Ge K-edge in $Ag_{0.15}(GeSe_3)_{0.85}$ and the Te K-edge in $Ge_8Sb_2Te_{11}$. 34

14 Analyzer scans at the Ge edges for $Ag_{0.50}(GeSe_3)_{0.50}$. 36

15 Ratio of the intensity at the peak position of the elastic signal and the actual measurement position extracted from fig. 14 and for the Ag edge in $Ag_{0.15}(GeSe_3)_{0.85}$. 36

16 Analyzer scans at the Te edges for $Ge_1Sb_4Te_7$ using a LiF analyzer. 37

17 Ratio of the intensity at the peak position of the elastic signal and the actual measurement position extracted from fig. 16 38

18 Full view of the analyzer scan at 2 $Å^{-1}$ from fig. 16. 38

19 Flow chart of the AXS/RMC method, indicating important steps and parameters. 41

20 Ternary phase diagram for the system Ag-Ge-Se. 44

21 Ionic conductivity σ in $Ag_x(GeSe_3)_{1-x}$ as a function x. 46

22 Raw data $I(Q)$ measured for the three Ag-$GeSe_3$ glasses at the Ge, Se and Ag K edges. 48
23 Intensity ratios of the actual measurement and the maximum of the elastic peak as described in section 3.2.4. 49
24 Total structure factors $S(Q)$ and differential structure factors at the Ag edge $\Delta_{Ag}S(Q)$ calculated from the raw data for AgGeSe. 50
25 Experimentally determined total structure factor $S(Q) - 1$ at 25.214 keV and $\Delta_k S(Q) - 1$ around the Ag, Ge and Se K edges, for Ag4 and Ag20. . . 51
26 Partial structure factors $S_{ij}(Q) - 1$ obtained by RMC, for Ag4 (x=0.15) and Ag20 (x=0.50). 53
27 Partial pair correlation functions $g_{ij}(r)$ obtained by RMC, for Ag4 and Ag20. 55
28 32×32 Å^2 sections of the configuration of Ag4 and Ag20 obtained by RMC, showing Ge-Se coordination polyhedra. 56
29 Radial distribution functions of the Se-Se and Ge-Ge correlation. 57
30 Bond angle distributions of Se-Ge-Se, Ge-Se-Ge, Ge-Se-Ag and Se-Se-Ag in Ag4 and Ag20. 59
31 Schematic view of the expansion in the $GeSe_4$ network upon increase of Ag content x (red: Ag, green: Se, blue: Ge). 60
32 64×64 Å^2 sections of the configuration of Ag4 and Ag20 obtained by RMC. 62
33 Probability of finding an Ag ion with the indicated number of neighbouring Ag ions in the respective coordination shells of Ag4 and Ag20. 63
34 Bond angles of Ag-Ag-Ag chains on the level of the first and second coordination shell. 63
35 Extended range order for Ag4 and Ag20, as illustrated by the function $\rho_{ij}(Q)$. 65
36 Sections of the partial structure factors of the Se-Se and Ge-Se correlations. 65
37 Illustration of the effect of a phase shift in $g(r)$ to the sign of the signal in $S(Q)$. 66
38 Location of the pseudo-binary line GeTe-Sb_2Te_3 in the ternary phase diagram Ge-Te-Sb. 71
39 Raw data $I(Q)$ measured for the three GeSbTe glasses at the Ge, Sb and Te K edges. 74
40 Uncorrected structure factors $S(Q)$ at the Sb absorption edge of GST-8,2,11. 75

41 Measured intensity for 24 individual scans at the Sb near egde of GST-8,2,11. 75
42 Ratio of the uncorrected intensity to the segmented scans at the Sb edges of GST-8,2,11. 76
43 Structure factors $S_{\mathrm{Sb}}(Q)$ of GST-8,2,11 after the correction shown in fig. 41 and 42. 76
44 Total structure factors for each composition and the corresponding total pair distribution functions. 79
45 A typical starting configuration of 10,000 atoms with a random distribution in the simulation box, for GST-8,2,11. 81
46 Experimentally determined total structure factors $S(Q)$ and $\Delta_k S(Q)$'s for the Ge, Sb and Te K edges. 82
47 Partial structure factors $S_{ij}(Q) - 1$ obtained by RMC for the GST compositions, by correlation. 85
48 Partial pair correlations functions $g_{ij}(r)$ obtained by RMC for the GST compositions, by correlation. 87
49 Bond angle distributions around each element in GST glasses. 97
50 Te-Ge-Te, Te-Sb-Te and Ge-Ge-Ge bond angle distributions in the GST glasses. 97
51 Evolution of the Te-Ge-Te bond angle with the cut-off distance in GST glasses. 98
52 Sections of the four GST configurations, illustrating the Ge network structure. 100
53 Ge network in GeTe. 102
54 Ge network in GST-8,2,11. 102
55 Ge network in GST-2,2,5. 102
56 Distribution of irreducible ring structures in GST glasses. 105
57 Partial structure factors and pair correlation functions obtained from AIMD in comparison with experimental results. 107
58 Partial pair correlation functions from AIMD with and without dispersion correction and detailed comparison for the Ge-Te correlation. 109
59 Comparison of the distribution of irreducible ring structures in GeTe by experimental and theoretical approaches. 110
60 T_g and T_c in GeTe-Sb_2Te_3. 112

List of Tables

2 Actual compositions of the GeSbTe samples and deviations to nominal composition by EDX. 25

3 Overview of the beamline specifications of BM02 and BL13XU. 26

4 Overview about the AXS experiments conducted for the $Ag_x(GeSe_3)_{1-x}$ glasses. 47

5 Weighting factors W_{ij} for each dataset at Q=2.0 Å^{-1} near the first peak position in $S(Q)$, for Ag4 and Ag20. 54

6 Partial and total coordination numbers of the first and second coordination shell obtained by AXS/RMC in comparison with other studies. 58

7 Interatomic distances in Å for the pairs ij obtained by AXS/RMC in comparison with other experiments. 58

8 Overview about the AXS experiments conducted for the GeSbTe glasses. . 73

9 Weighting factors W_{ij} of $S_{ij}(Q)$ for each dataset at Q=2.0 Å^{-1} near the first peak position in $S(Q)$, for the GST glasses. 81

10 Interatomic distances for the GST glasses obtained by RMC. 89

11 Higher order coordination shell distances for the GST glasses. 90

12 Partial and total coordination numbers of the first coordination shell in the GST glasses obtained by AXS/RMC. 90

13 Homopolar bond contributions in GST. 91

14 Coordination numbers of GeTe in comparison with other studies. 92

15 Coordination numbers of GST-8,2,11 in comparison with other studies. . . 92

16 Coordination numbers of GST-2,2,5 in comparison with other studies. . . . 94

17 Characteristics of the Ge-Ge FSDP. 101

18 Experimentally obtained optical dielectric constants ε_∞ of GeSbTe and related elements and the optical contrast for the PCM's. 116

List of Abbreviations

Abbreviations (in alphabetical order)

AIMD	*ab-initio* molecular dynamics
AXS	anomalous x-ray scattering
CN	coordination number
DFT	density functional theory
ERO	extended-range order
ESRF	European Synchrotron Radiation Facility in Grenoble, France
FSDP	first sharp diffraction peak (or "pre-peak")
FWHM	full width half maximum
IRO	intermediate-range order (also: MRO, medium-range order)
MAD	multi-wavelength anomalous diffraction
PCM	phase-change material
PMC	programmable metallization cell
PP	principal peak
RMC	Reverse Monte Carlo (simulation)
(A)SAXS	(anomalous) small angle x-ray scattering
SPring-8	Super Photon ring-8 GeV in Hyogo, Japan
SRO	short-range order
(E)XAFS	(extended) x-ray absorption fine structure (spectroscopy)

Symbols

A	absorption factor
C	normalization constant
E	energy
ε_∞	optical dielectric constant
$\langle f \rangle$	averaged form factor
f	form factor
f'	real part of the anomalous dispersion term
f''	imaginary part of the anomalous dispersion term
I	intensity

i, j	label for different elements
k	label for an element with reference to its absorption edge
L_c	coherence length
λ	wavelength
N	number of particles
Q	modulus of the scattering vector
r	distance (in real space)
R	electrical resistance
R_c	characteristic length
R_w	goodness of fit value
ρ_{N}	number density
τ_{cryst}	time of crystallization
T_c	temperature of crystallization
T_g	temperature of glass transition
2Θ	scattering angle
w_{ij}	weighting factor for partial structure factors
$\Delta_k w_{ij}$	differential weighting factor for partial structure factors at the absorption edge of element k
x_i	molar fraction of element i

Note: Correlations are labelled with a hyphen, e.g. Ge-Te, except when used as a subscript, e.g. $S_{\mathrm{GeTe}}(Q)$.

For the AgGeSe glasses, the designation is Agx for $\mathrm{Ag}_x(\mathrm{GeSe}_3)_{1-x}$.

Germanium telluride as the chemical compound is denoted without a hyphen, i.e. GeTe.

The nomenclature for the other GeSbTe glasses is GST-x,y,z for $\mathrm{Ge}_x\mathrm{Sb}_y\mathrm{Te}_z$.

Part I

Theoretical and experimental basis

1 Introduction

This work analyses the atomic structure of two classes of chalcogenide glasses which are employed as data storage materials. Germanium selenide or germanium telluride compounds are the materials of choice for this application, as they possess very high glass forming abilities and can be alloyed with other elements (as silver or antimony) in order to achieve desirable characteristics. Two different approaches for the long-term storage of digital data are realized in these materials: The "classical" procedure is based on so-called phase change materials, or PCMs. These materials can switch reversibly between an amorphous and a crystalline phase via laser irradiation or resistive heating. The concomitant major differences in optical and electrical properties are then used to encode binary data. Another more recent approach is represented by the so-called "programmable metallization cell", or PMC, which makes use of the oppositional properties of the glass for low conductivity of electrical current on the one hand and fast conductivity of ions on the other hand. The difference in the electrical resistance in an "unmetallized" cell (i.e. the glass in its usual structure) and a "metallized" cell (i.e. the glass pervaded by small metal-like conduction pathways) is used for data storage applications.

A schematic overview of the structural changes that enable the functioning of data storage devices based on phase-change materials and programmable metallization cells is given in fig. 1. In a PCM, a short intense laser pulse or resistive heating to a temperature above the melting point followed by rapid cooling transforms the crystal into the glass, and a long weak laser pulse or resistive heating just above the crystallization point, respectively, transforms the glass back into a crystal. In a PMC, the application of a voltage (typically a few hundred mV) is supposed to lead to the formation of a metallized "nano-path" through the material, which acts as a conductor for an electric current. The same voltage applied in the opposite direction leads to the dissolution of the nano-path. The transitions between the different states take place on the nanosecond time scale and are accompanied by a major change in the optical dielectric constant ε_∞ and the electrical resistance R.

It is the structural characterization of the amorphous state of the PCMs or PMCs that still triggers considerable research interest. Lacking the long-range order typical for crystals, amorphous compounds are usually regarded as largely random networks,

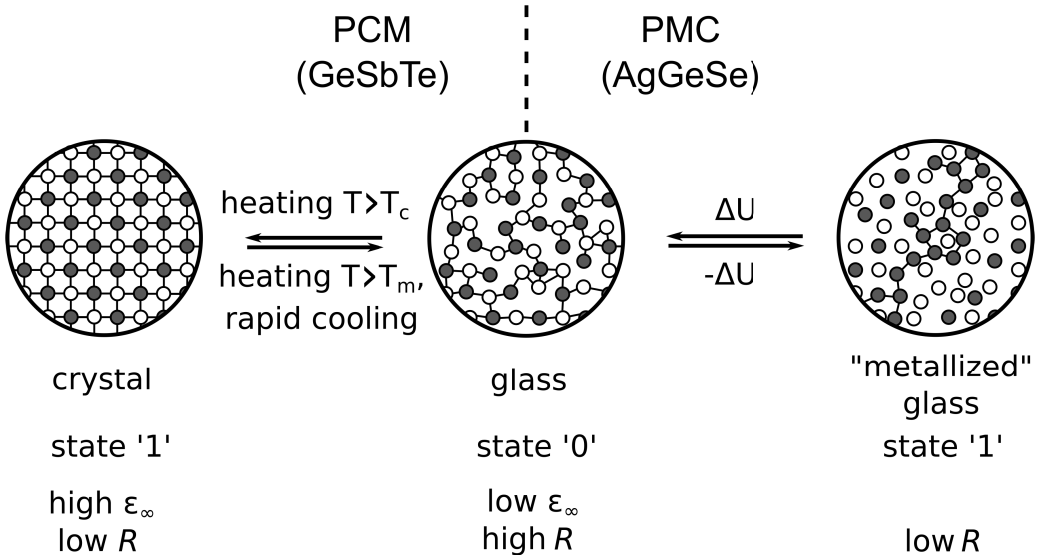

Figure 1: Schematic view of the structural changes which the phase-change materials (PCMs) and the programmable metallization cell (PMC) are based on (see text for further description). T_c: crystallization temperature and T_m: melting temperature. The transition between the different states is accompanied by a major change in the optical dielectric constant ε_∞ and the electrical resistance R.

exhibiting only an order on the atomic nearest neighbour range due to the formation of chemical bonds. This level of order is commonly rationalized using the so-called "$8 - N$ rule", which just predicts the average number of nearest neighbouring atoms by the number of valence electrons N of the respective element. The actual short-range order, however, can be much more complex than predicted by this model. The aim of the research presented in this work therefore is to gain a deeper insight into the short-range order in chalcogenide glasses and its relationship to the intermediate range order (SRO and IRO, respectively; in corresponding reports, the descriptions "near-range" and "medium-range order" are found as well). In contrast to the definition of the SRO, the definition of the IRO is still strikingly elusive, and includes for example second and third coordination shells and the distribution of bond angles and irreducible ring structures. The importance of correlations on these longer length scales has become apparent in the last years, and indeed I will try to show the peculiar consequences for the material properties that stem from a variation of the IRO with the elemental composition of the glass.

However, the determination of the atomic configuration in such disordered materials even today remains a challenging task. A considerable effort is still invested to develop new experimental techniques and to establish new and high-performance radiation sources

for such investigations. Complex experimental methods need to be applied and great care must be taken during the data reduction and analysis before the experimental data can straightforwardly be interpreted. One of the more powerful tools to determine the partial structure correlations in disordered multi-component materials along a broad range of length scales is anomalous x-ray scattering (AXS) in combination with appropriate modelling procedures, like Reverse Monte Carlo (RMC) computer simulations. This approach allows to investigate the relation between the microscopic structure and physical properties in a broad variety of amorphous materials, and offers a range of advantages compared to other methods that probe similar structural characteristics. The AXS technique therefore is becoming increasingly important and may offer the key to unveil the final relations to understand the structure of amorphous systems and the correlation with their unique properties.

The structure of this dissertation is as follows: The first part introduces the theoretical basis for the anomalous scattering technique, i.e. an appropriate overview about the interaction of x-rays with disordered matter and about the RMC modelling procedure, and it presents a short introduction into the experimental details of AXS. The second part outlines the experiments on the two families of chalcogenide glasses. In this respect, each chapter will firstly examine the experimental data and the direct results of the RMC simulations, followed by a discussion and interpretation of the impact of the presented structure for the materials' properties. At the end, a concise conclusion summarizes briefly the relevant findings in a common framework.

2 Theoretical background

As stated above, models and theoretical frameworks for the evaluation of scattering experiments on disordered systems are well established, and are described in a number of publications. It is therefore not the aim of the following section to give a complete overview, but rather to present a short summary of the theoretical basics necessary for the analysis and interpretation of the experimental data gathered in this work. The interested reader may be referred to further reading as provided in references [1–5].

2.1 Scattering experiments on disordered systems

Scattering experiments on disordered materials represent the outcome of a diffraction experiment as a function of the so called scattering vector $\vec{Q}$ or its modulus $|\vec{Q}|$. $\vec{Q}$ is defined as the vector difference between the wave vectors of the scattered and the incident radiation, $\vec{k'}$ and $\vec{k_0}$, respectively:

$$\vec{Q} = \vec{k'} - \vec{k_0} \tag{2.1}$$

Since x-ray scattering can be regarded as being elastic, the moduli of the wave vectors are equal, i.e. $|\vec{k'}| = |\vec{k_0}| = 2\pi/\lambda$ and the modulus of $\vec{Q}$ amounts to

$$|\vec{Q}| = Q = 2k_0 \sin\left(\frac{2\Theta}{2}\right) \tag{2.2}$$

in units of an inverse length. The scattering patterns usually obtained from diffraction experiments on disordered systems differ substantially from those obtained by conventional crystal diffraction. The Bragg peaks observed there are considerably more intense (in the order of magnitude of a factor $10^3 - 10^6$) than the scattering pattern obtained from disordered materials. This is due to the fact that if x-rays are deflected from crystal planes at a suitable scattering angle 2Θ, where the scattering vector $\vec{Q}$ matches a reciprocal lattice vector, the diffraction condition is simultaneously fulfilled for a vast number of atoms with identical interatomic separation. Also, their real space correlation extends periodically along extremely wide ranges causing the signal width in reciprocal space, i.e. the Bragg peak, to narrow correspondingly. In a liquid or glass, the interatomic distances are continuously distributed and the diffraction condition is fulfilled at any angle. Also, in disordered materials the correlation range in real space is usually

short, extending only to the next or second next atomic neighbours. As a consequence, the resulting diffraction peaks are widely broadened in reciprocal space leading to weak scattering amplitudes. Therefore, the experimental intensity must be carefully corrected with respect to background contributions from container materials and other radiation sources as well as intrinsic intensity contributions like Compton scattering or fluorescence effects. The pure scattering amplitude of a sample is solely given by the superposition of all the waves emerging from N atomic scattering centres situated at their individual average positions. The intensity is then the square of the sum over all these waves weighted by their individual atomic form factors $f_n(\vec{Q})$:

$$I(\vec{Q}) = \left| \left\langle \sum_{n=1}^{N} f_n(\vec{Q}) \cdot \mathrm{e}^{-iQr_n} \right\rangle \right|^2 = f(\vec{Q})^2 \left\langle \sum_n \sum_{n'} \mathrm{e}^{-iQ(r_n - r_{n'})} \right\rangle . \tag{2.3}$$

n and n' in eq. 2.3 indicate the atomic positions and the angle brackets denote that the spatial situation of the N atoms may be an ensemble averaged arrangement. To obtain the right hand side of eq. 2.3 it was assumed that all atoms in the sample are identical and contribute to the overall amplitude with the same form factor. Instead of eq. 2.3 we may then write

$$I(\vec{Q}) = N \cdot f(\vec{Q})^2 \frac{1}{N} \left\langle \sum_n \sum_{n'} \mathrm{e}^{-iQ(r_n - r_{n'})} \right\rangle = N \cdot f(\vec{Q})^2 \cdot S(\vec{Q}) \tag{2.4}$$

which defines the structure factor $S(\vec{Q})$, which is characteristic of the explored sample:

$$S(\vec{Q}) = \frac{1}{N} \left\langle \sum_n \sum_{n'} \mathrm{e}^{-iQ(r_n - r_{n'})} \right\rangle \tag{2.5}$$

The structure factor $S(\vec{Q})$ is the central function to be obtained in scattering experiments on disordered materials. According to eq. 2.4, it can directly be obtained from the corrected scattering intensity $I(\vec{Q})$. It contains the total interference as a function of scattering vector and can hence be interpreted as a distribution function of interatomic pair distances in reciprocal space. In fact, it can be shown within the framework of statistical mechanics that $S(\vec{Q})$ is related to the pair correlation function $g(\vec{r})$ in real space. $g(\vec{r})$ is a statistical function which indicates the probability of finding an atom at a position $\vec{r}$ with

respect to a reference atom located at the origin. The link between the pair correlation function $g(\vec{r})$ and the structure factor $S(\vec{Q})$ is given by a Fourier transformation:

$$g(\vec{r}) - 1 = \frac{1}{\rho_N (2\pi)^3} \int (S(\vec{Q} - 1) \mathrm{e}^{-i\vec{Q}\vec{r}} d\vec{Q}, \tag{2.6}$$

where ρ_N represents the particle density of the sample. Assuming complete structural isotropy, one may neglect the vector properties of Q and r. Switching also to polar coordinates, eq. 2.6 can be considerably simplified to give [6]:

$$g(r) - 1 = \frac{1}{2\pi^2 r \rho_N} \int Q \cdot (S(Q) - 1) \sin(Qr) dQ. \tag{2.7}$$

The pair correlation function $g(r)$ allows the characterization of the explored disordered sample with respect to interatomic distances and coordination numbers: The average number of particles n in a given coordination shell, delimited by r_1 and r_2, respectively, can be obtained from integrating the peaks of the corresponding radial distribution function $n(r)$:

$$n = \int_{r_1}^{r_2} n(r) dr = \int_{r_1}^{r_2} 4\pi \rho_N \cdot r^2 g(r) dr. \tag{2.8}$$

The identification of coordination numbers and interatomic distances is the purpose of basically any structure investigation on a disordered material. While this information characterizes simple mono-atomic systems unambiguously, the interpretation of scattering data from chemically complex samples becomes more difficult. The procedure to deduce an expression for the scattering intensity of such samples is initially identical to the derivation of eq. 2.3, i.e. the pure scattering intensity is determined by the square of the sum of all waves emerging from the irradiated atoms. Primarily, the sum index may run over all atoms irrespective of their chemical nature. Depending on the composition, many different combinations of the scattering length factors appear in the double sum, thus preventing a factorization as in case of a simple mono-atomic system. As a consequence, the structure factor of a mixture cannot be defined as a dimensionless quantity as in eq. 2.5 and it will retain the dimension of an area. Yet, all terms in the double sum have the same form and it appears more sensible to sum over the possible chemical combinations rather than over pairs of atom indices [7]. This approach leads to the following expression

for the pure scattering intensity:

$$I(Q) = N\left(\langle f(Q)^2\rangle - \langle f(Q)\rangle^2\right) + N \cdot \langle f(Q)^2\rangle S_{FZ}(Q), \tag{2.9}$$

where the structure factor is now defined as a weighted sum over *partial structure factors* $S_{ij}(Q)$:

$$S_{FZ}(Q) = \sum_i \sum_j w_{ij} \cdot S_{ij}(Q) \tag{2.10}$$

with $w_{ij} = \frac{x_i x_j f_i f_j}{\langle f(Q)\rangle^2}$. $S_{FZ}(Q)$ is the Faber-Ziman structure factor [7]. i and j run over all combinations of chemical compositions, f_i an f_j are the respective form factors and x_i and x_j denote the corresponding molar fractions. The angle brackets indicate an average over the chemical composition. It should be noted that the structure factor in eqs. 2.9 and 2.10 has subsequently been made dimensionless by normalizing it to the square of the average form factor in the sample. Rearranging eq. 2.9 finally gives a prescription how to extract the properly normalized Faber-Ziman total structure factor from an experimental intensity $I(Q)$:

$$S_{FZ}(Q) = \frac{\frac{C}{N} I(Q) - (\langle f(Q)^2\rangle - \langle f(Q)\rangle^2)}{\langle f(Q)\rangle^2}. \tag{2.11}$$

The normalization constant C has been introduced to ensure that the structure factor approaches unity for sufficiently large Q-values. $S_{FZ}(Q)$ in eq. 2.11 is the experimentally accessible total structure factor of a multi-component system. According to eq. 2.10, it is composed of the partial structure factors $S_{ij}(Q)$. These quantities represent the correlation between particles of species i to particles of species j in reciprocal space. The partial structure factors are related to corresponding pair correlation functions $S_{ij}(r)$ in the same way as is $S(Q)$ to $g(r)$ in eq. 2.7:

$$g_{ij}(r) - 1 = \frac{1}{2\pi^2 r \rho_N} \int Q \cdot (S_{ij}(Q) - 1)\sin(Qr) dQ. \tag{2.12}$$

The partial pair correlation function $g_{ij}(r)$, similar to the total $g(r)$ for a pure sample, determines the probability of finding a particle of species j at the distance r, if there is another particle of species i at the origin. Note that $g_{ij}(r) = g_{ji}(r)$. Analogous to the coordination number of eq. 2.8, there are also partial coordination numbers n_{ij}, which can be obtained from the partial radial distribution function $n_{ij}(r)$. In this case, the relative

fraction of the atom j under consideration has to be accounted for:

$$n_{ij} = \int_{r_1}^{r_2} n_{ij}(r)dr = 4\pi\rho_N x_j \int_{r_1}^{r_2} r^2 g_{ij}(r)dr. \tag{2.13}$$

Note that here $n_{ij} \neq n_{ji}$, except if $x_i = x_j$. Besides the FZ-approach presented here, there exist other schemes to separate the total structure factor into independent parts. The Ashcroft-Langreth or AL-approach [8] is in principle similar to the Faber-Ziman method but defines scattering functions which oscillate around zero. Of more practical use, however, is the formalism that has been derived by Bhatia and Thornton [9]. The BT-approach has been developed for binary mixtures, though it has been generalized for multi-component systems by Blétry [10]. It defines a set of partial structure factors representing density-density (NN), concentration-concentration (CC) and density-concentration (NC) correlations. It is also related to the Faber-Ziman approach as it can be shown that both can be expressed as a linear combination of the other [10, 11]. An excellent survey is given in reference [4].

Though the total structure factor can directly be measured in an experiment, the relevant structural information is contained in the partial correlation functions. For a system consisting of n components, there exist $n(n+1)/2$ partial functions, irrespective of the partition scheme (FZ, AL or BT). Their determination is the ultimate goal in the structure exploration on a chemical mixture, but the partials are not directly accessible from conventional scattering experiments and specific efforts must be undertaken for their determination. One possible approach to obtain the partial correlation functions for a multi-component system is to employ a Reverse Monte Carlo Simulation (see section 2.3) However, a direct determination of the $n(n+1)/2$ unknown $S_{ij}(Q)$-functions of an n-component system is in principle possible. In this case, an equal number of linear equations like eq. 2.10 were needed to form a linear set of inhomogeneous equations, which can be solved numerically if the corresponding coefficient determinant is nonzero. Such additional equations, however, can only be generated if the w_{ij}-factors in eq. 2.10 can be modified without changing the chemical composition. Basically, this is possible in both x-ray- and neutron scattering. In the latter this can be achieved by preparing three different samples with differing isotopic composition of the sample components. In this case, the form factors entering the weighting coefficients in eq. 2.10 have to be replaced by the average

neutron scattering length of the isotopically manipulated sample constituents. In x-ray scattering, a variation of the form factors is also possible by a suitable energy variation of the incident radiation. The general procedure can be easily understood considering a model system consisting of just two different chemical components A and B. According to eq. 2.10, the total structure factor is then given as

$$S_{FZ}(Q) = w_{AA}(Q) \cdot S_{AA}(Q) + 2 \cdot w_{AB}(Q) \cdot S_{AB}(Q) + w_{BB}(Q) \cdot S_{BB}(Q) \tag{2.14}$$

where the coefficients are determined by the composition and the form factors in the sample:

$$w_{AA}(Q) = \frac{x_A^2 f_A^2(Q)}{\langle f(Q)\rangle^2}, w_{BB}(Q) = \frac{x_B^2 f_B^2(Q)}{\langle f(Q)\rangle^2} \text{ and } w_{AB}(Q) = \frac{x_A x_B f_A(Q) f_B(Q)}{\langle f(Q)\rangle^2} \tag{2.15}$$

with x_i being the molar fractions of component i. The corresponding set of linear inhomogeneous equations then reads:

$$\begin{aligned} S_{FZ}^{I}(Q) &= w_{AA}^{I}(Q) \cdot S_{AA}(Q) + 2 \cdot w_{AB}^{I}(Q) \cdot S_{AB}(Q) + w_{BB}^{I}(Q) \cdot S_{BB}(Q) \\ S_{FZ}^{II}(Q) &= w_{AA}^{II}(Q) \cdot S_{AA}(Q) + 2 \cdot w_{AB}^{II}(Q) \cdot S_{AB}(Q) + w_{BB}^{II}(Q) \cdot S_{BB}(Q) \\ S_{FZ}^{III}(Q) &= w_{AA}^{III}(Q) \cdot S_{AA}(Q) + 2 \cdot w_{AB}^{III}(Q) \cdot S_{AB}(Q) + w_{BB}^{III}(Q) \cdot S_{BB}(Q) \end{aligned} \tag{2.16}$$

The superscripts I, II and III stand for the different experiments where the coefficients are altered either by isotopic substitution or by an appropriate variation of the x-ray energy. In matrix notation eq. 2.16 reads:

$$\begin{pmatrix} S^{I}(Q) \\ S^{II}(Q) \\ S^{II}(Q) \end{pmatrix} = \begin{pmatrix} w_{AA}^{I} & w_{AB}^{I} & w_{BB}^{I} \\ w_{AA}^{II} & w_{AB}^{II} & w_{BB}^{II} \\ w_{AA}^{III} & w_{AB}^{III} & w_{BB}^{III} \end{pmatrix} \cdot \begin{pmatrix} S_{AA}(Q) \\ 2S_{AB}(Q) \\ S_{BB}(Q) \end{pmatrix} \tag{2.17}$$

$$[S_{FZ}] = [W] \cdot [S_{ij}] \quad .$$

Hence, the vector containing the partial structure factors is easily evaluated from the experimentally determined vector of total structure factors and the matrix containing the weighting factors of eq. 2.16. The final accuracy of this method depends on the unavoidable experimental error on one hand, but also on the quality of the matrix $[W]$ on

the other hand. It is preferable to choose the variation of the coefficients as to produce as much scattering contrast between the three experiments as possible, i.e. the resulting total structure factors should differ greatly. The value of the normalized determinant $|W|_n$ can be used as a measure for this quality [12] where normalization is achieved by dividing each row r by $\sqrt{\sum_s w_{rs}^2}$, with s indicating the column index. A modulus of $|W|_n = 1$ corresponds to the optimal case [13]. Poorly conditioned matrices lead to an unpredictable enhancement of the statistical error and may cause unphysical features in the resulting partial scattering functions.

A method of choice to introduce a contrast in the matrix of the weighting factors is anomalous x-ray scattering, or AXS. This method constitutes an essential part of the work presented here, and will therefore be discussed in more detail in the following section.

2.2 Differential anomalous x-ray scattering

This section will give a summary on the method of anomalous x-ray scattering (or AXS), with special regard to the differential AXS approach that appears to be best suited for chemical applications. It will thus be demonstrated how the variation of the incident energy in a x-ray scattering experiment allows to discriminate between different partial correlations in a mixture. A closer inspection of the interaction between the x-ray photon and the atom reveals that there exists an energy dependent contribution to the atomic form factor:

$$f(Q, E) = f_0(Q) + f'(E) + if''(E). \tag{2.18}$$

$f_0(Q)$ in eq. 2.18 denotes the ordinary atomic form factor, which represents the Fourier transform of the atomic electron density, while $f'(E)$ and $f''(E)$ are the real and imaginary parts of the complex energy dependent contribution. The imaginary part is characteristic of the absorption behaviour, and the real part represents the main influence on the scattering strength of the element under consideration in a typical AXS experiment. These terms are usually small and can be neglected; however, they become significant when the incident energy is close to an absorption edge of the atom. This behaviour is denoted as *anomalous dispersion*. It is illustrated in figure 2 where the static atomic form factors for Ge and Se, as e.g. in Ag-$GeSe_3$ glasses, are exemplary shown in the upper diagram and the calculated energy dependent terms are depicted in the lower graph ($f_0(Q)$ data are

taken from [14] and the anomalous terms from [15, 16]). The anomalous dispersion gave rise to the development of several techniques aiming to distinguish between the scattering from different atomic species in chemical mixtures and alloys [13, 17, 18]. A direct determination as in eq. 2.16 is theoretically possible, if scattering experiments at $n(n+1)/2$ different incident energies E_k are conducted. These may then cause a contrast between the differently obtained total structure factors $S_{FZ}(Q, E_k)$ in an n-component mixture and a set of inhomogeneous linear equations similar as in eq. 2.16 may be formulated. The weighting coefficients then take the general form:

$$w_{ij}(Q, E_k) = \frac{x_i x_j f_i(Q, E_k) \cdot f_j^*(Q, E_k)}{|\langle f(Q, E_k)\rangle|^2}. \tag{2.19}$$

Here, i and j are again the indices of the chemical species. $f_i^*(Q, E_k)$ is the complex conjugate of the form factor in eq. 2.18. However, figure 2 already indicates that the variation of the form factors with the energy is only a few percent of the static $f_0(Q)$. This inevitably leads to a poorly conditioned coefficient matrix for the linear set of equations, i.e. the corresponding normalized determinant $|W|_n$ will always be much less than one. For example, in the case of the two-component systems GeTe and typical AXS measurement conditions (see below), $|W|_n$ is in the range 0.05 to 0.1. The determinant decreases for a multi-component system like $Ge_8Sb_2Te_{11}$, for which values in the order of magnitude of 0.001 are obtained. As already stated above, small errors in the measured $S_{FZ}(Q, E_k)$ will then cause capriciously large errors in the partial structure factors. This problem cannot even be compensated if intense third generation synchrotrons like the ESRF in Grenoble are used as x-ray sources to improve the statistical quality of the data.

While one has only restricted influence on the statistical error of a measurement, it can be shown that systematic errors in the scattering data mainly cancel out if the method of differential intensities (or "differential AXS") is employed [19]. Thereby, data measured at two different energies below an absorption edge of element k are subtracted to give the differential structure factor $\Delta_k S(Q)$ of that specific element. The idea behind this approach is simple: Close to the edge, say about 20-30 eV below (see for example E_{near} at the Ge-K-edge in figure 2), the scattering from correlations of this component is weaker while correlations between the other elements in the sample scatter with normal intensity. Still further below the edge, say about 200-300 eV, (see for example E_{far}

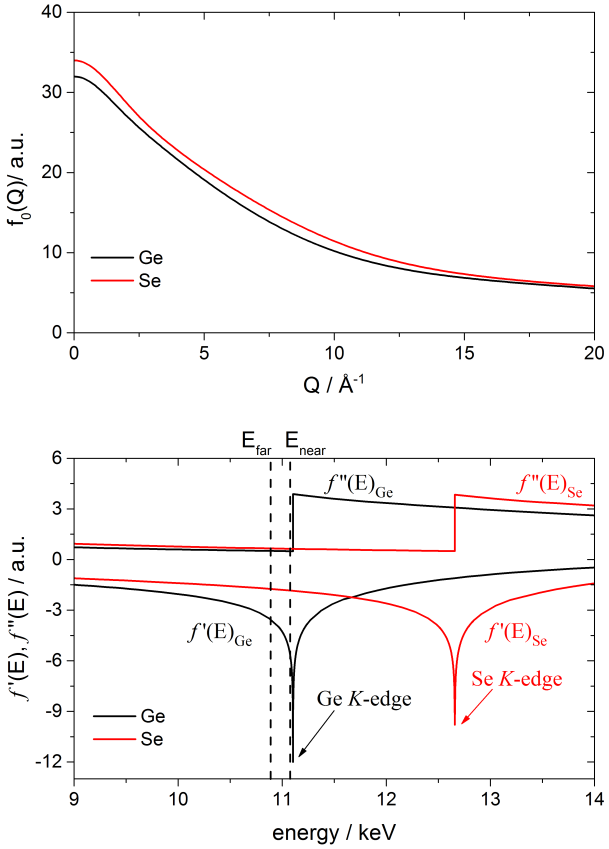

Figure 2: Static form factors $f_0(Q)$ for Ge (black line) and Se (red line) are shown in the upper graph. The lower graph gives the respective anomalous contributions $f'(E)$ and $f''(E)$. Both scales are given in electron units. As an example, E_{far} and E_{near} denote typical values used to determine differential scattering intensities at the Ge-K-edge.

at the Ge-K-edge in figure 2) scattering from the k-correlations is again increased. If the difference between the two measured intensities is taken, the scattering from the other correlations mainly drop out, since they are little affected by the energy variation. Thus, primarily correlations from the element under consideration will contribute to the differential scattering intensity. The differential structure factor $\Delta_k S(Q)$ can readily be obtained from the experimental intensities of eq. 2.9 taking into account an appropriate normalization:

$$\Delta_k S(Q) = \frac{\Delta_k \left[C \cdot I(Q, E_{far}, E_{near})\right] - \Delta_k \left[\langle f^2 \rangle - \langle f \rangle^2\right]}{\Delta_k \left[\langle f \rangle^2\right]}. \tag{2.20}$$

The Δ in eq. 2.20 denotes the difference of the subsequent quantity in square brackets taken between E_{far} and E_{near} close to the absorption edge of element k. This time normalization is achieved by dividing through the difference of the squared average form

factors. This kind of normalization is on the one hand chosen as to retain the structure factor again dimensionless, but also to obtain a reasonable scale for this quantity. Otherwise the values of the differential structure factor were extremely small along the entire Q-scale. Also, a constant C is once again introduced to ensure that the structure factor approaches unity for sufficiently large Q-values. The experimental procedure is then repeated at the absorption edges of the other elements as well. As a result, one obtains the differential structure factors $\Delta_k S(Q)$ for each component k of the mixture, each containing the correlations of this specific element to all elements in the sample. It is in principle possible to Fourier transform these functions in order to get the corresponding differential pair correlation functions $\Delta_k g(r)$, which can then directly be interpreted (see e.g. [17, 19]). However, other possibilities exist allowing to draw more detailed structural conclusions from the data. The differential structure factors can also be related to the partial structure factors if eq. 2.14 is used to calculate $\Delta_k S(Q)$:

$$\Delta_k S(Q) = \sum_i \sum_j \Delta_k w_{ij}(Q) \cdot S_{ij}(Q). \tag{2.21}$$

According to eq. 2.19 and accounting for the normalization of eq. 2.20 the coefficients are then defined as

$$\Delta_k w_{ij}(Q, E_{far}, E_{near}) = \frac{x_i x_j \Delta[f_i(Q) f_j^*(Q)]}{\Delta_k \left[\langle f(Q)\rangle^2\right]}. \tag{2.22}$$

Again, the Δ indicate the differences of the quantities in the square brackets calculated at the different incident energies E_{far} and E_{near} at the edge of element k. As for the w_{ij}'s in eg. 2.19, the Q-dependence of the weighting factors is generally weak, cf. fig. 3, which gives an impression of the general Q-dependence and of the effect of the differential AXS method on the $w_{ij}(Q)$ for amorphous $Ag_{0.15}(GeSe_3)_{0.85}$. For a two component system, it is still possible to further pursue the approach of solving a set of inhomogeneous equations directly. For this, a third measurement needs to be performed still further away from the aforementioned absorption edges of the sample elements. Then three measured structure factors exist and the set of inhomogeneous equations reads:

$$\begin{aligned} S(Q) &= w_{AA} \cdot S_{AA}(Q) + 2 \cdot w_{AB} \cdot S_{AB}(Q) + w_{BB} \cdot S_{BB}(Q) \\ \Delta_A S(Q) &= \Delta_A w_{AA} \cdot S_{AA}(Q) + 2 \cdot \Delta_A w_{AB} \cdot S_{AB}(Q) + [\Delta_A w_{BB} \cdot S_{BB}(Q)] \\ \Delta_B S(Q) &= [\Delta_B w_{AA} \cdot S_{AA}(Q)] + 2 \cdot \Delta_B w_{AB} \cdot S_{AB}(Q) + \Delta_B w_{BB} \cdot S_{BB}(Q). \end{aligned} \tag{2.23}$$

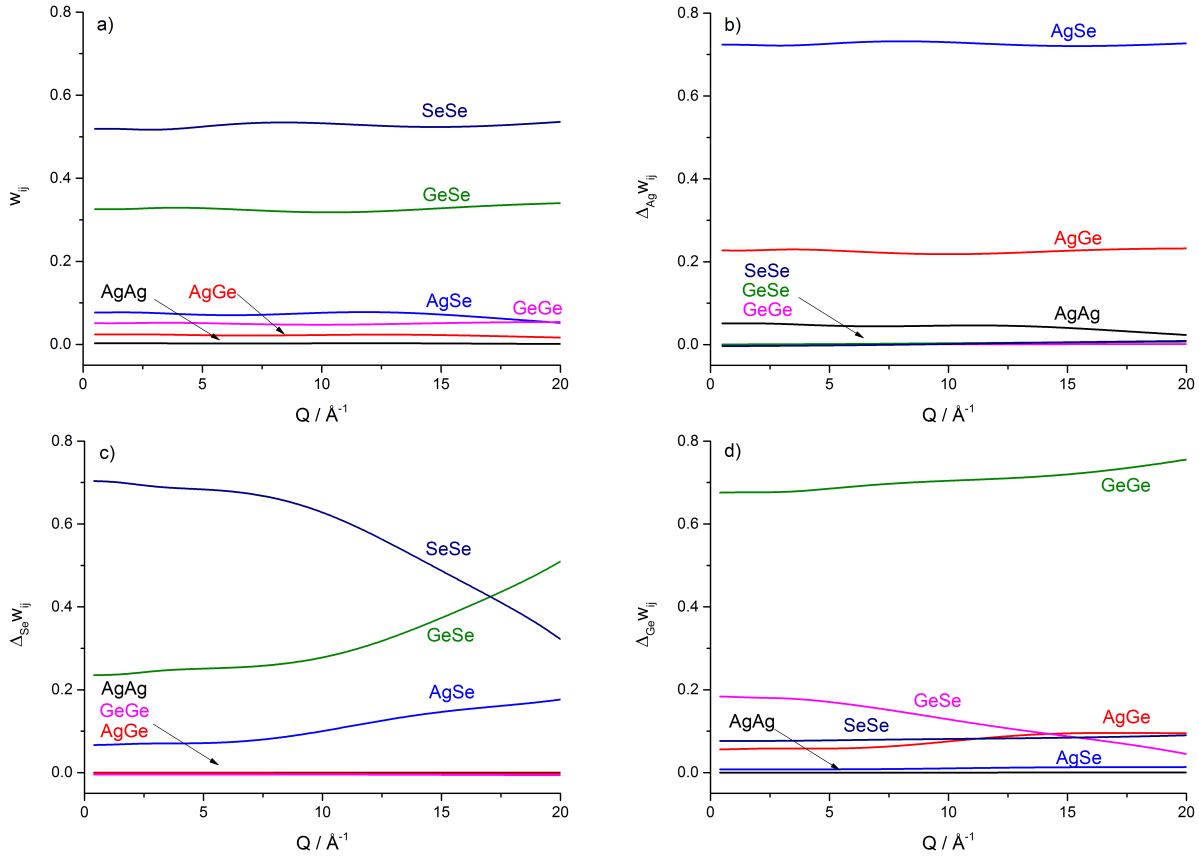

Figure 3: Weighting factors w_{ij} for $Ag_{0.15}(GeSe_3)_{0.85}$ along the Q-range of interest for the total (a) and each differential structure factor: (b) Ag, (c) Se, (d) Ge.

The first row in eq. 2.23 corresponds to the single $S(Q)$-measurement far away from the edges of the sample components, where the coefficients w_{ij} are then calculated using eq. 2.19. The other two rows are determined by the differential measurements at the absorption edge of element A and element B, respectively. Here, the coefficients are determined by eq. 2.22 (the Q-dependence of the coefficients in eq. 2.23 is neglected for clarity). The quantities written in square brackets, e.g. $[\Delta_A w_{BB}]$, are usually small, since no contributions from the element related to the absorption edge are included in the weighting factors (i.e. for example $B - B$ correlations at the A-absorption edge). Thus, they are sometimes omitted completely [13]. On the other hand, as will be shown in fig. 3, such an approximation is not always justified.

The advantage of solving eq. 2.23 instead of a set of equations obtained from directly measuring $S(Q, E_k)$ at three different energies is that the coefficient matrix of eq. 2.23 is considerably better conditioned. This is due to the fact that the differences in eq. 2.22 enhance those factors containing the form factors of the considered edge element and

suppress the others. This is illustrated in fig. 3 for an AXS experiment on $Ag_{0.15}(GeSe_3)_{0.85}$ (see section 4 for the measurement conditions): The w_{ij}'s in the total $S(Q)$ are dominated by Se contributions due to its large relative amount (71.9% Se, 23.9%, 4.2% Ag). In contrast, fig. 3 b) demonstrates the suppression of correlations that are not related to the element k in the $\Delta_k w_{ij}$'s, e.g. in the $\Delta_{Ag} w_{ij}$'s, for which all correlations not containing Ag are close to zero. The limitation of this effect can be seen in the $\Delta_{Ge} w_{ij}$'s, where Se contributions still constitute a considerable factor: This fact is easily rationalized by considering the large relative amount of Se, the characteristics of f'_{Se} near the absorption edge of Ge, where a small difference between the two measurements below the Ge edge is still visible (see fig. 2), and eq. 2.22. Nonetheless, the experimental $\Delta_k S(Q)$'s consequently comprise a considerably larger contrast than the directly measured $S(Q, E_k)$'s.

2.3 Reverse Monte Carlo Modelling

The Reverse Monte Carlo (or RMC) modelling procedure represents an alternative to a direct solution of eq. 2.23. In a nutshell, RMC simulates the real sample by an ensemble of atoms as hard spheres in a box (e.g. 10000 atoms for a typical simulation of an amorphous system). In each simulation step, individual atoms are moved and the partial $g_{ij}(r)$ are calculated from the atomic positions in the computer generated ensemble. Using the inverse of the Fourier transform in eq. 2.12, the respective $S_{ij}(Q)$ can be computed to determine the total structure factor $S_{FZ}(Q)$ according to eq. 2.10. The simulation is then repeated until satisfactory agreement between the experimental and the computed total structure factors is reached. However, it should be kept in mind that this approach is just a fitting procedure with $n(n+1)/2$ free parameters and that their number is growing steeply with the number of chemical components. It is therefore appropriate to also include other boundary conditions, like atomic diameters, into the simulation in order to make the result more unequivocal.

The basic idea of the Reverse Monte Carlo algorithm has been proposed by McGreevy and Pusztai in 1988 [20]. Since then, various program packages have been developed and continuously been improved. For the simulations presented in this work, the RMC_POT package coded by Gereben et al. [21, 22] has been employed. As input data for the RMC simulation, the individual differential structure factors for each element and one total

structure factor obtained at the highest measured energy are included. If not mentioned otherwise, an input configuration of 10,000 atoms with proper stoichiometry is chosen, with atoms randomly distributed in a cubic box corresponding to the number density of the material. Furthermore, minimum atomic distances are defined to avoid unphysical configurations, and if clearly known from other studies or based on chemical arguments, bond angle constraints are defined for selected correlations.

The following list will give a short overview and a discussion of important parameters for the RMC method as employed in this work.

- Cut-off distances, i.e. minimal interatomic distances, need to be included for all distinct atomic pairs. Atomic radii, e.g. covalent radii, are usually a good first approximation for these values. However, they need to be carefully adjusted during the RMC procedure, and can be raised considerably e.g. when certain correlations are proven to exhibit no chemical bonds. Such data can be obtained from EXAFS measurements, for example.

- Maximum move distances have to be given for each element. High values (ca. 1 - 3 Å) grant some flexibility to the system, but usually result in a low number of accepted moves. Small values (ca. 0.2 - 0.5 Å) raise the number of accepted moves considerably.

- r-space resolution determines the sampling rate of the three dimensional configuration and the corresponding pair distribution functions. Values of $2\pi/Q_{max}$ (with the highest measured Q-value Q_{max}) should not be exceeded. For practical purposes, smaller values of 0.1 - 0.15 Å are chosen.

- Sigma values (or σ-values) are weighting factors for the individual input datasets and for other constraints on the simulation. Thus, they are used to constrain RMC results to the experimental data. The usual order of magnitude in the simulations presented in this work is 0.001 to 0.01. The relative magnitude of the σ values determines a relative weighting of the different datasets; for example, the statistical error in the total $S(Q)$ measurements is smaller than the error in the $\Delta_k S(Q)$'s, and thus constitutes a reason to choose a smaller σ-value. Larger σ-values represent a "weak" constraint and smaller σ-values represent a "strong" constraint, i.e. the

relative weighting of a given constraint in the simulation is higher, the smaller the corresponding σ-value is chosen.

- Polynomial correction terms can be used as a correction to the experimental data. Polynomial functions of zeroth to third order and a correction of the amplitude can be employed, e.g. to account for experimental background intensities that cannot be corrected entirely. The amplitude correction is especially useful for differential intensities collected by AXS, since e.g. small errors resulting from the normalization procedure can be corrected.

- Bond angle constraints can be included for distinct atomic pairs. Such constraints are employed (usually with comparably high σ values) to exclude unphysical configurations.

- (Average) coordination constraints can be included to enforce a certain coordination around a specific element, e.g. a four-fold coordination of Ge atoms.

The agreement between the experimental data and the functions obtained from RMC are described via the squared error sum χ^2, weighted with the individual σ value. The goodness of the fit is defined independent of the σ's by the R_W values assigned to each dataset included in the simulation.

The RMC scheme is an efficient way to obtain a physical model which matches the experimental data; however, some problems concerning this data analysis procedure need to be addressed. First, configurations obtained by RMC will likely be the most disordered possible configurations. Furthermore, including the interatomic cut-off distances will sometimes result in unphysical atomic agglomeration or even sharp peaks close to the cut-off [23], which must be carefully scrutinized. Also, configurations with bond angles of about 60° are found very often in the three dimensional model, as this arrangement corresponds to the most space saving configuration, but may be an artifact from the simulation scheme.

Finally, it should always be kept in mind that - despite the apparent improvement of the structural information obtained from the AXS/RMC method - the resulting data still needs to be critically scrutinized. The formal solution of an under-determined system of linear equations can never lead to an unambiguous result. Therefore, the outcome of this

procedure should be carefully tested, e.g. against other starting configurations. Also, as already mentioned above, it certainly improves the reliability of the data if other constraints are additionally included into the RMC-simulation. It is also an inherent limitation to all structural descriptions of disordered materials that the investigated structures are regarded as being isotropic and are thus described with one-dimensional functions (i.e. $g(r)$ instead of $g(\vec{r})$). The resulting solution will therefore only be valid within the isotropic approximation.

2.4 Structural hierarchy in amorphous systems

As mentioned above, amorphous systems exhibit an order mainly on the range of nearest neighbours. This range is probed e.g. by EXAFS measurements. However, an order beyond the nearest neighbours can be observed with adequately sophisticated techniques. This level of order, which is still well below a long-range order as observed in crystals, has long been a subject of controversy. The discussion of this order is often based on an intense, narrow peak observed in the low-Q region between about 0.5 - 1.5 Å^{-1} in many disordered systems. This signal is called "pre-peak", since it appears well before the "principal" peak around 2 - 3 Å^{-1}, or "first sharp diffraction peak" (FSDP). Throughout this work, this peak will be referred to as FSDP in accordance with the established nomenclature. Most studies including diffraction experiments on amorphous samples agree that the existence of a FSDP is a sign for an intermediate range order in the system, and assign two significant values to it: the characteristic length R_c and the coherence length L_c, defined by:

$$R_c = \frac{2\pi}{Q_{FSDP}} \qquad \text{and} \qquad L_c = \frac{2\pi}{\Delta Q_{FSDP}} \tag{2.24}$$

with the position Q_{FSDP} and the half-width value ΔQ_{FSDP} of the FSDP. Due to the position characteristic for this peak, values for R_c are typically in the range of 4 - 10 Å; values for L_c vary more, but are typically in the range of 10 - 20 Å. Though these values are often listed in the respective studies, their meaning often remains somehow elusive.

Elliot gives a summary on the FSDP in covalent glasses and liquids [24], arguing that this peak is connected to the concentration-concentration structure factor (in the BT formalism). The proposed model is able to explain the temperature and pressure dependence of the FSDP in various liquids and glasses. It can also explain why the

observed FSDP generally occurs at approximately the same position when plotted against the reduced coordinate $Q_{FSDP} \cdot r_1$, with r_1 being the nearest neighbour distance. This value was determined to be $Q_{FSDP} \cdot r_1 \approx 2.5$.

A novel interpretation of the FSDP is given in a survey by Uchino et al. [25], analyzing the FSDP in silica glass. They interpret the characteristic length $R_c = 2\pi/Q_{FSDP} \approx 4.1$ Å as the interplanar separation lengths of "pseudo-Bragg planes" that are spanned by the second-neighbour correlations of Si and O atoms. Though the interatomic separation of Si-Si and O-O is about 5 Å, as seen in the pair correlation function, the parallel planes spanned by these correlations necessarily exhibit a shorter separation. They are thus a possible explanation for the FSDP with the indicated characteristic length (corresponding to the position 1.5 $Å^{-1}$ in the $S(Q)$) without an actual atomic accumulation at 4 Å in the $g(r)$. The density fluctuations associated to these planes vanish over a length of $L \approx 10 - 15$ Å. This model thereby provides a possible interpretation of the values R_c and L_c, and offers an explanation as to why there is generally no peak in the $g_{ij}(r)$ on length scales expected by the position of the FSDP.

The structural hierarchy associated to the different levels of order is discussed within three length scales, for which different definitions are given. Elliott defines the following three different length scales with distinct attributed interactions: [26–28]

- Short-range order (SRO): 2-5 Å, 2 and 3 body interactions, coordination numbers, bond length and angles.
- Medium-range order (MRO): 5-20 Å, 4 and 5 body interactions, dihedral and adjacent dihedral angle distributions.
- Extended-range order (ERO) also called long-range structure - LRS - in order to avoid confusion with a "long-range order" observed only in crystals: characterized by oscillations in $g(r)$ beyond 10-20 Å, extending to $15 \cdot r_{\text{nearest neighbour}}$.

Slightly different definitions are given by Salmon et al. They discuss the concept of "topological" vs. "chemical" order in disordered systems [29]. Using the Bhatia-Thornton formalism, they differentiate between chemical (via $g_{CC}(r)$) and topological order (via the $g_{NN}(r)$) in the binary glasses $ZnCl_2$ and $GeSe_2$. They provide evidence for three different length scales observable in all partial correlations, which are defined as:

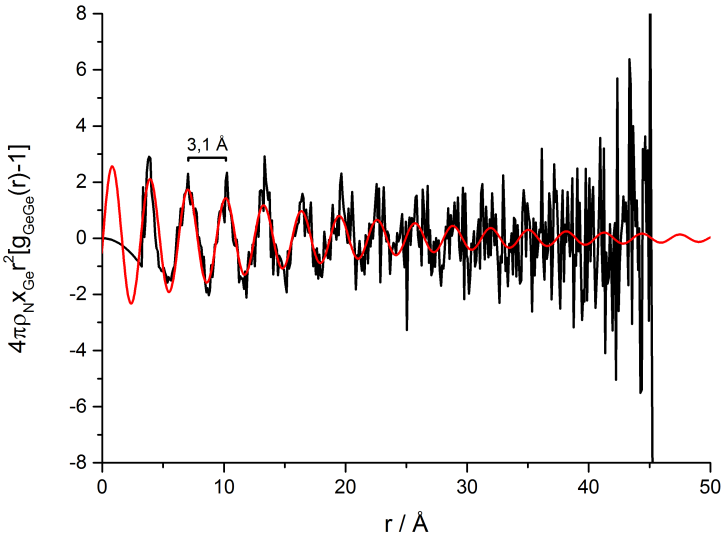

Figure 4: Extended range order in $Ag_{0.50}(GeSe_3)_{0.50}$. Black line: result of the RMC simulation for the Ge-Ge correlation. Red line: fit with a damped sine wave with a periodicity of 3.1 Å.

- Short-range order. This order is mainly associated to the principal peak at $Q_{PP} \approx 2$ Å^{-1}, thus obtaining a real space order of about 3 Å, corresponding to the nearest neighbour distance.

- Intermediate-range order. Dominated by the FSDP, in the range between the nearest neighbours and about 12 Å.

- Extended-range order. Oscillations in $g(r)$ with a periodicity of $\frac{2\pi}{Q_{\mathrm{PP}}}$ above $r = 12$ until about 62 Å, which are interpreted as a propagation of SRO.

As will be shown in section 4.2.4, similar levels of order are also found e.g. in Ag-$GeSe_3$ glasses. Figure 4 illustrates the concept of extended range order in the $Ag_{0.50}(GeSe_3)_{0.50}$ glass, employing the reduced RDF of the Ge-Ge correlation, with the general form

$$\rho_{ij}(r) = 4\pi\rho_N x_j r^2[g_{ij}(r) - 1]. \tag{2.25}$$

The resulting function exhibits clear oscillations with a periodicity of $\frac{2\pi}{Q}$=3.1 Å, corresponding to the position of the principal peak in the $S_{\mathrm{GeGe}}(Q)$ at $Q_{PP} = 2$ Å^{-1}. The oscillations vanish at length scales beyond 30 Å.

3 Experimental details

The following section focuses on practical aspects connected with the actual realization of the AXS experiments. First, the preparation of the different samples is presented as well as the employed sample containers. Furthermore, a short description is given of the experimental environment at the synchrotron facilities where the experiments were conducted. The AXS setup and data collection method necessitate a careful data reduction procedure and certain specific corrections, which are discussed and illustrated with some chosen examples.

3.1 Sample preparation

Two different kinds of chalkogenide glasses are the subject of this work: fast ionic conducting glasses of the general composition $Ag_x(GeSe_3)_{1-x}$, and Ge-Sb-Te phase-change materials with the general compositions $(GeTe)_{1-x}(Sb_2Te_3)_x$. The following subsections will present the preparation and initial characterization of these samples.

3.1.1 Ag-$GeSe_3$ glasses

The amorphous samples of $Ag_x(GeSe_3)_{1-x}$ with x=0.15, 0.33 and 0.50 were prepared by water-quenching from the sealed mixture of the respective ratios of Ag, $GeSe_2$ and Se into a silica tube under vacuum. The three values correspond to Ag concentrations of 4.2, 11 and 20 at.% of Ag. The resulting powder was pressed into a round pellet with a flat surface of about 13 mm in diameter, cf. fig. 5. The concentrations and homogeneity were examined by x-ray diffraction and differential thermal analysis at several positions of the quenched samples. The samples have been provided by Dr. Yokinobu Kawakita (J-PARC).

Note that the nomenclature is not consistent throughout the literature: The first studies on the ionic conductivity of these glasses by Kawasaki et al. [31] adopts the 'chemists notation' Ag-($GeSe_3$), which is not to be confused with the designation of the form $Ag_x(Ge_{0.25}Se_{0.75})_{1-x}$, for which the x directly indicates the atomic fraction of silver. In the following, I will abbreviate the compositions for the investigated samples using the latter definition with "Ag4" ($x_{Kawasaki} = 0.15$), "Ag11" ($x_{Kawasaki} = 0.33$) and "Ag20" ($x_{Kawasaki} = 0.50$).

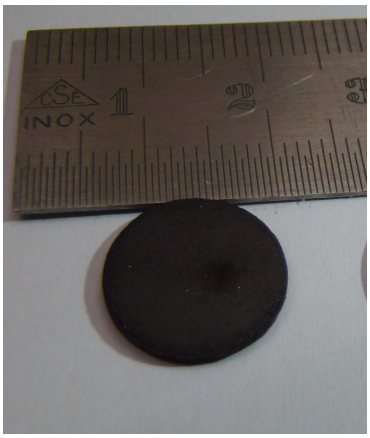

Figure 5: Photograph of an Ag-$GeSe_3$ sample. [30]

3.1.2 GeTe-Sb_2Te_3 glasses

The $(GeTe)_{1-x}(Sb_2Te_3)_x$ samples have been prepared by radio-frequency sputtering deposition. Sputter targets with the nominal compositions have been purchased from EvoChem. As substrate materials, SiO_2 glass disks with a diameter of 5 cm were used. The background pressure was adjusted to 10^{-7} to 10^{-6} mbar, the working pressure for the deposition from an Ar plasma was set to about 10^{-2} mbar, employing a continuous flow of Argon of 10 sccm. The target surface was cleaned during a pre-sputtering process for about 15 min prior to each experiment. The actual cathode power used was 20 - 50 W. See e.g. [32] for similar sputtering conditions to produce $Ge_2Sb_2Te_5$.

The composition of the sputtered samples was checked by energy dispersive x-ray (EDX) analysis (see. fig. 7), and the amorphicity has been confirmed prior to the experiment by in-house x-ray diffractometry using a Cu-K_α source (compare the exemplary graph in fig. 8). EDX analysis was performed at 6 - 7 different spots on the sputtered samples; table 2 summarizes the measured compositions and the deviation from the nominal composition. Three samples of GeTe, five samples of $Ge_8Sb_2Te_{11}$, one sample of $Ge_1Sb_4Te_7$ and two samples of Sb_2Te_3 have been characterized. Generally, longer sputtering times, higher values for the background pressure and higher RF powers lead to larger deviations from the nominal composition. The samples with the lowest deviation from the nominal composition, i.e. GeTe#6, GST-8,2,11#3 and GST-8,2,11#5 and GST-1,4,7#1 have been used for the actual AXS experiments. The Sb_2Te_3 samples were unstable, exhibiting a spontaneous crystallization, and thus were not be employed in the AXS experiments.

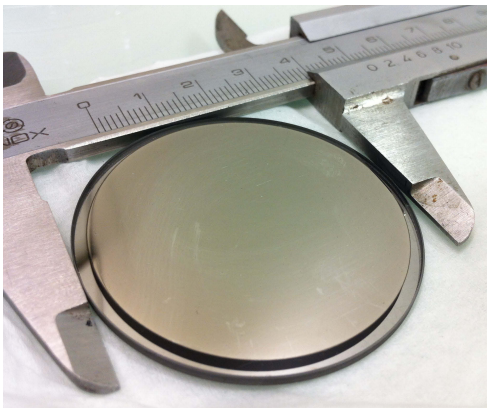

Figure 6: Photograph of a GST sample with a thickness of about 1 μm, sputter-deposited on a glass substrate.

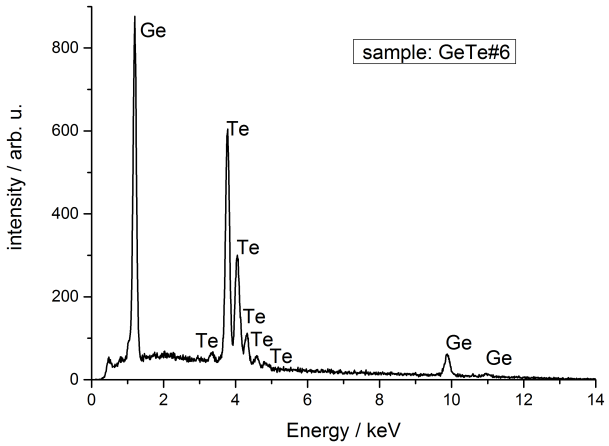

Figure 7: Exemplary graph of an EDX analysis of GeTe. Each peak is assigned to its corresponding element. Element ratios taken from this graph are illustrated in tab. 2.

Sample thicknesses have been monitored by profilometry and were found to be in the range of 0.6 to 3.8 μm; the sputtering rate is thus determined to be 0.57 μm/h (i.e. about 1.6 Å/s) for a RF power of 50 W.

3.1.3 Sample container

The amorphous samples of AgGeSe could be prepared in comparably large quantities due to the good glass forming ability of the material. These samples were measured in reflection geometry during the AXS experiment without the need for a sample container, thus facilitating the data reduction process.

The GeSbTe samples can only be prepared in small amounts (a few milligram per sputtered sample), so that they cannot be pressed into a pellet. These samples had to be

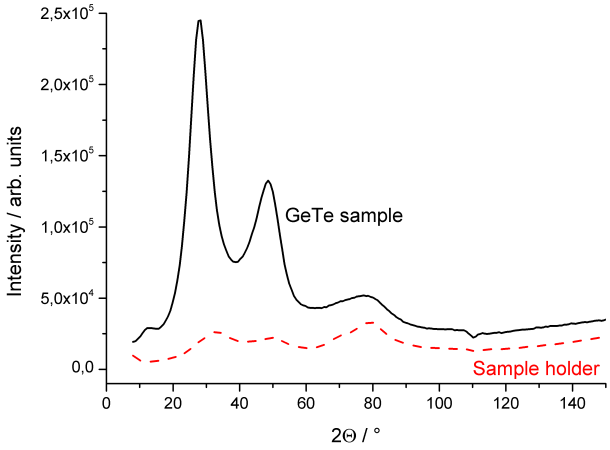

Figure 8: Raw data of GeTe measured with a Cu-K_α source. The dashed red line shows the background produced by the sample holder. Data points were collected in steps of 0.7° (equivalent to ∼0.05 $Å^{-1}$). Each data point was measured for 3384 seconds.

Table 2: Actual compositions of the GeSbTe samples and deviations to nominal composition by EDX.

Sample label	Composition / at%			Deviation / at%		
	Ge	Sb	Te	Ge	Sb	Te
GeTe ideal	**50**		**50**			
GeTe #03	47.04		52.96	-2.96		2.96
GeTe #04	41.69		58.31	-8.31		8.31
GeTe #06	49.45		50.55	-0.55		0.55
GST-8,2,11 ideal	**38.10**	**9.52**	**52.38**			
GST-8,2,11 #01	36.47	12.23	51.31	-1.63	2.70	-1.07
GST-8,2,11 #02	35.86	11.03	53.11	-2.24	1.50	0.73
GST-8,2,11 #03	37.26	10.42	52.32	-0.83	0.89	-0.06
GST-8,2,11 #05	37.14	10.49	52.37	-0.95	0.96	-0.01
GST-8,2,11 #06	36.27	10.53	53.20	-1.83	1.00	0.82
GST-1,4,7 ideal	**8.33**	**33.33**	**58.33**			
GST-1,4,7 #01	8.60	34.44	56.96	0.26	1.11	-1.38
Sb_2Te_3 ideal		**40.0**	**60.0**			
Sb2Te3 #2		40.65	59.35		0.65	-0.65
Sb2Te3 #3		40.48	59.52		0.48	-0.48

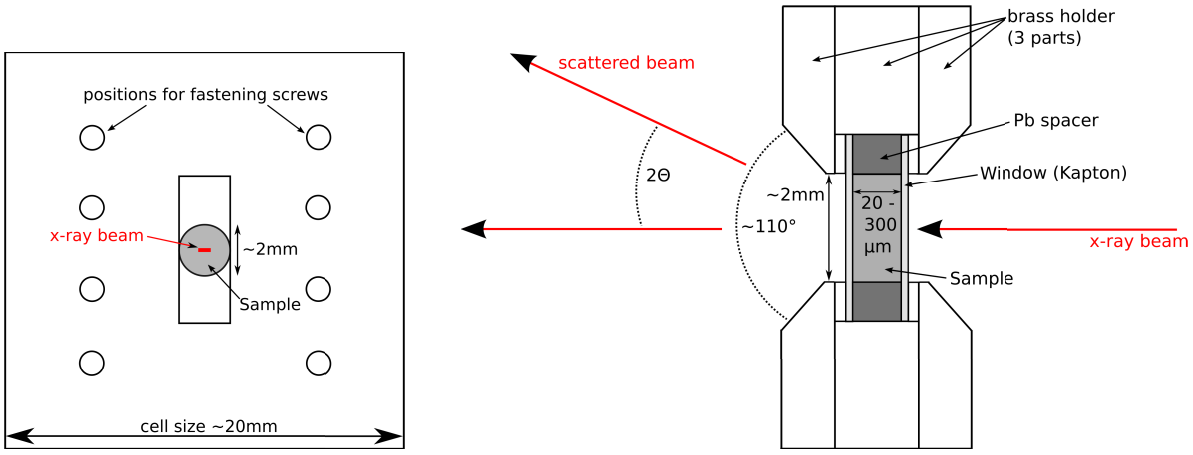

Figure 9: Schematic representation of the sample container (not to scale). Left: front view, right: side view.

enclosed in a custom-built brass sample container. This container allows to adjust sample thicknesses between 20 μm and 300 μm using a leaden spacer, as schematically shown in fig. 9. Kapton (i.e. polyimide) foil with a thickness of 7 μm was chosen as window material due to its high transmittance of x-rays in the desired energy region. This setup permits an angular opening of about 110°.

3.2 Practical aspects of the AXS experiments

The following subsection gives a short overview over the two beamlines used for the AXS experiments, i.e. beamline BM02 at the European Synchrotron Radiation Facility (ESRF) and beamline BL13XU at the Super Photon ring-8 GeV (SPring-8), and over the data reduction procedures necessary for data acquired there. The specific corrections, which are required due to the different analyzer crystals, are discussed in a separate subsection.

Table 3: Overview of the beamline specifications of BM02 [33] and BL13XU [34].

Parameter	BM02	BL13XU
Extraction method	bending magnet, 0.8 T	undulator
Primary monochromator	double crystal Si(111) or Si(311)	double crystal Si(111)
Intensity	10^{11} ph/s	$6 \cdot 10^{13}$ ph/s
Typical beam size	0.3 x 0.1 mm	0.5 x 0.3 mm
Primary energy resolution $\frac{\Delta E}{E}$	$2 \cdot 10^{-4}$	$1 \cdot 10^{-4}$
Analyzer crystal, res. $\frac{\Delta E}{E}$	bent graphite, $7 \cdot 10^{-3}$	LiF, $1 \cdot 10^{-3}$
Detector	NaI scintillator	NaI scintillator

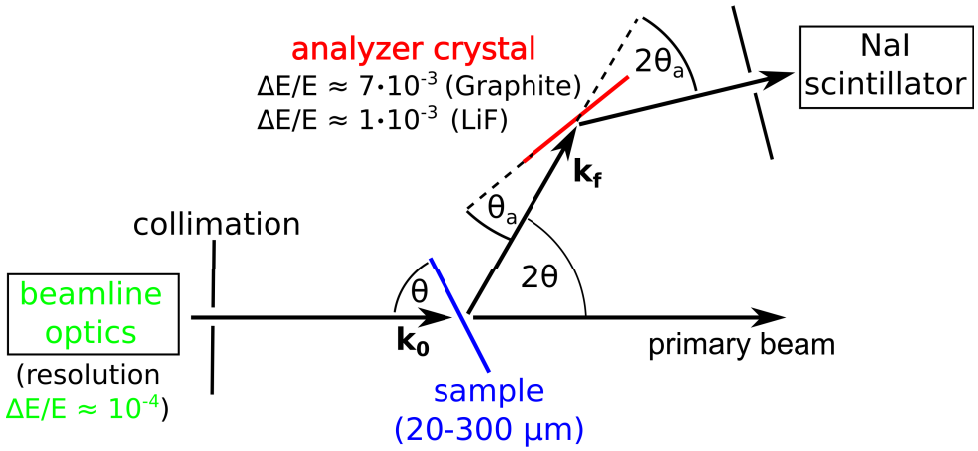

Figure 10: Schematic experimental setup for AXS experiments in transmission geometry.

The general setup for an AXS experiment is shown schematically in fig. 10 for the case of an experiment conducted in transmission geometry. The use of an analyzer crystal allows to discriminate contributions other than the purely elastic scattering. Scanning the position of this crystal at a given Q-value gives the energy dispersive intensity of the detected beam (called "analyzer scans" in the following), so that the various contributions, which are indistinguishable in a conventional scattering experiment, can be determined. This step is crucial for the AXS method as the error induced by a detection of only the integral intensity may be too large to be neglected when calculating the differential intensities.

3.2.1 General considerations

For the successful application of the AXS method, some general experimental aspects should be considered carefully, the main issues being the energy of the incident x-ray beam and the energy resolution of the experimental setup. The choice of the incident energy is the crucial factor for the AXS method. For elements between the atomic numbers 23 and 52 (Vanadium to Tellurium), there usually exist experimentally accessible K absorption edges. For elements heavier than Tellurium, L absorption edges become experimentally more feasible, and also offer a contrast which is higher than that obtained at K edges, as the variation of $f'(E)$ is more pronounced. Elements lighter than Vanadium, on the other hand, do not possess x-ray absorption edges in a suitable energy range. It should also be kept in mind that the choice of the incident energy defines the experimentally

accessible Q-range, as the scattering angle is given by the experimental setup. In practice, this represents a problem especially for absorption edges below 10 keV, which sets a maximum Q-value of about 9 Å^{-1} for a typical setup with a maximal detector angle $2\Theta_{max} = 120°$. Furthermore, the two energies close to the edge needed for the calculation of the differential structure factor should be chosen as to provide properly enhanced weighting factors. But also here, the choice is limited by two factors: On the near-edge side, theoretical values for the dispersion terms obtained from *ab-initio* calculations [15] can be employed for the calculations, if the energy is chosen not too close to the edge (usually in the range of a few ten eV below the edge). Closer to the edge, the effect of the chemical environment on the inner core electrons is strong, so that the calculated values are not accurate enough anymore, and an individual measurement of the absorption edge by means of x-ray absorption spectroscopy becomes necessary (cf. [35]). On the far-edge side, the energy range is mainly limited by the variation of the dispersion terms of other constituent elements and by considering that the energy difference may not be too large in order to profit from the error cancellation described above. Consequently, this energy is usually chosen to be only a few hundred eV below the edge. This choice is by far made most often, but it is not mandatory: An interesting example for an AXS experiment using energies very far from the absorption edge (i.e. 1.6 keV and 7 keV, respectively) can be found in reference [18], Chapter 5.1.

Another important aspect is the energy resolution. On the one hand, the necessary resolution of the incident beam is in the order of magnitude of a few eV (i.e. roughly $\Delta E/E = 10^{-4}$) and is usually unproblematic to achieve at a modern synchrotron facility. On the other hand, the resolution of the detecting system – that is preferably in the range of 50 to 150 eV or below (i.e. about $\Delta E/E = 1 \cdot 10^{-2}$) – requires some explanation. The detector resolution needs to be sufficient in order to discriminate inelastic scattering contributions from the elastic signal; in the case of wide-angle anomalous scattering, these contributions are due to the Compton and the Resonant Raman effect (see e.g. [4] for further explanations on these effects), and can be sufficiently well determined with the specified resolution. However, a better resolution at the detector is usually obtained by cutting off a part of the x-ray beam, and thus leads to a decrease of the measured intensity. This, in turn, has a direct effect on the statistical quality of the data, which is an essential factor for the calculation of the differential structure factors. Taking into account these

considerations, the use of an analyzer crystal (e.g. graphite) and a standard scintillating detector have proven to be the best experimental compromise for this method. The use of this setup instead of e.g. a solid state detector greatly simplifies the data reduction procedure [36] and usually grants a higher counting rate. At the moment, this kind of experimental setup is only available at the beamlines BM02 at the ESRF and at BL13XU at SPring-8. In the end, the concept of obtaining element specific information by use of the anomalous dispersion effect is of course not limited to the field of glassy structure determination or the differential AXS method. A contrast variation via the $f'(E)$ part of the form factor is also used in e.g. small angle scattering (ASAXS). [37] On the other hand, X-Ray Absorption Fine Structure (XAFS) [38, 39] spectroscopy methods employ the structured imaginary part $f''(E)$ of the form factor above the absorption edge; and last but not least, a technique that employs the changes in both anomalous dispersion parts of the form factor is e.g. the Multi-wavelength Anomalous Diffraction (MAD) [40].

3.2.2 Data reduction

The measured intensities have to be corrected for absorption effects and inelastic scattering contributions, and have to be normalized to an absolute scale. The basic methods for these corrections are described shortly in the following. For a more detailed look into the specific physical basis of the underlying effects, appropriate references for further reading are given.

Absorption When conducting a scattering experiment, the absorption of the x-ray photons generally depends on the scattering angle 2Θ and has to be corrected in order to calculate the scattering intensity arising purely from the sample. For an experiment in reflection geometry, this dependence can usually be neglected if the sample has an appropriate thickness [41]. Since furthermore, the experiments in reflection geometry in this work were performed without a sample container, usually no absorption correction is necessary. On the other hand, for experiments in transmission geometry, not only the 2Θ-dependence, but also the contribution from the sample container has to be corrected [41, 42]:

$$I_S(2\Theta) = \frac{1}{A_{S,SC}(2\Theta)} \cdot \left(I_{S,C}(2\Theta) - \frac{A_{C,SC}(2\Theta)}{A_{C,C}(2\Theta)} \cdot I_C(2\Theta) \right), \tag{3.1}$$

with

$$A_{S,SC}(2\Theta) = \exp\left(-\frac{\mu_C d_C + \mu_S d_S}{\cos(\frac{2\Theta}{2})}\right) \tag{3.2}$$

$$\frac{A_{C,SC}(2\Theta)}{A_{C,C}(2\Theta)} = \exp\left(-\frac{\mu_S d_S}{\cos(\frac{2\Theta}{2})}\right). \tag{3.3}$$

and using the following definitions:

$I_S(2\Theta)$, the scattering intensity arising purely from the sample

$I_C(2\Theta)$, the scattering intensity of the sample cell

$I_{S,C}$, the cumulative intensity of sample and cell (which is directly measured during the experiment)

$A_{S,SC}(2\Theta)$, the absorption factor for a scattering process in the sample and absorption in the sample and in the cell

$A_{C,SC}(2\Theta)$, the absorption factor for a scattering process in the cell and absorption in the sample and in the cell

$A_{C,C}(2\Theta)$, the absorption factor for a scattering process in the cell and absorption in the cell

μ_S, the mass attenuation coefficient of the sample

μ_C, the mass attenuation coefficient of the cell

(Values for the mass attenuation coefficients can be taken from [43].)

d_S, the sample thickness

d_C, the thickness of the cell windows.

Inelastic scattering contributions Contributions from inelastically scattered photons to the desired experimental data mainly arise from Compton scattering and the resonant Raman effect. Due to the high energy resolution that can be achieved by the use of an analyzer crystal, it is possible that the actual impact of inelastic scattering can be negligible in AXS experiments; nevertheless, these contributions have to be closely monitored, as will be shown in the following.

Compton scattering describes the process of photons scattered from quasi-free electrons in the sample (i.e. the energy of the photon is much larger than the binding energy of the scattering electron). The energy of the Compton radiation depends on the scattering angle 2Θ; it is well known that the difference in wavelength of the original (λ_0) and scattered photons (λ') is given by: [4]

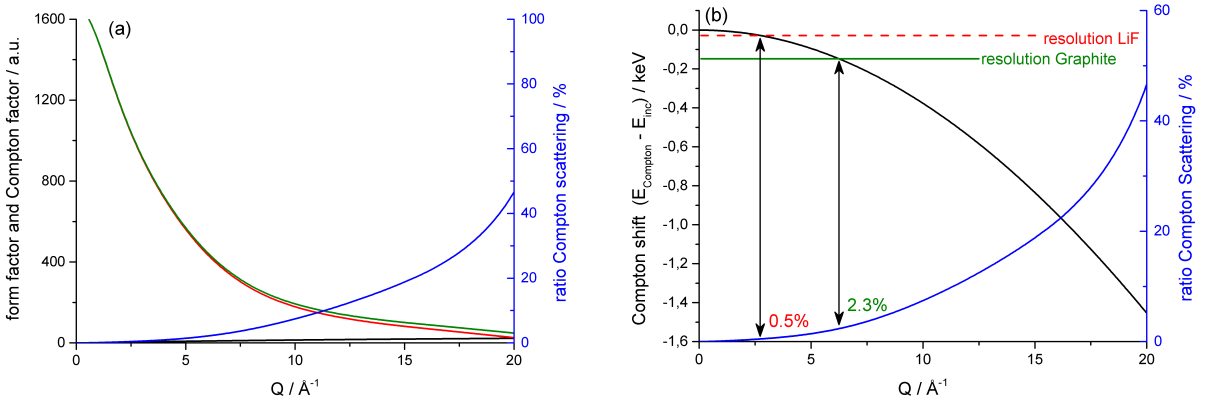

Figure 11: a) Contribution of the Compton scattering to the overall scattered intensity in the case of GeTe (Te far edge). Red: form factor $\overline{f^2}$, black: Compton factor C_{GeTe}, green: total intensity $\overline{f^2}+C_{GeTe}$, blue: contribution of the Compton scattering to the total intensity. b) Compton energy by eq. 3.5 as a function of Q. Displayed in red and green are the energy resolution values of the LiF and Graphite analyzer crystal, respectively, and the blue line is the contribution of the Compton scattering to the total intensity taken from (a). Indicated are the values of the Compton ratios where the energy curve intersects the analyzer resolution values.

$$\Delta\lambda = (\lambda' - \lambda_0) = \frac{h}{m_e c}[1 - \cos(2\Theta)]. \tag{3.4}$$

The resulting energy of the Compton radiation E' as a function of the original energy E_0 and the scattering vector Q is then obtained after some rearrangements:

$$E' = \frac{E_0}{1 + \frac{h^2}{8m_e\pi^2} \cdot \frac{Q^2}{E_0}}. \tag{3.5}$$

The relative intensity of the Compton radiation can be estimated through Compton scattering factors C_α[44], which have been tabulated for most elements α. The sum of the average squared form factor $\overline{f^2}$ and the Compton scattering factor is a good approximation of the theoretically expected intensity, thus the ratio of $C_\alpha/(\overline{f^2} + C_\alpha)$ can be used to calculate the intensity of the Compton scattering in the analyzer scans, as shown in fig. 11 for the case of GeTe. It is noteworthy that the relative contribution rises considerably as a function of Q; on the other hand the Compton energy decreases, thus the separation of the elastic signal also grows as a function of Q.

The resonant Raman effect (or resonant Raman scattering, RRS) constitutes another inelastic contribution. However, this effect becomes important only for measurements very close to an absorption edge, i.e. the "near-edge" scans about 20-30 eV below the

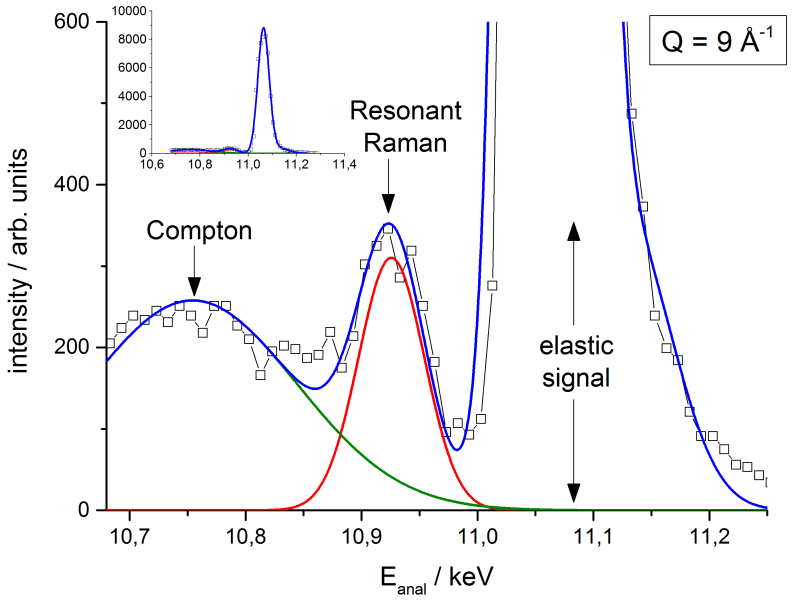

Figure 12: Section of the analyzer scan at 9 $Å^{-1}$ at the Ge near edge of $Ag_{0.50}(GeSe_3)_{0.50}$, showing the contributions of inelastic scattering to the elastic peak. The inset displays the complete intensity range. The three contributions are fitted with Gaussian functions as follows: overall intensity (blue), Resonant Raman (red) and Compton (green).

absorption edge. It has been described as an " 'anticipating' fluorescence"[4]. During a "normal" fluorescence process, the absorption of a photon with an incident energy E_0 higher than the energy of the absorption edge E_{edge} leads to the emission of typical K_α and K_β radiation. However, though the incident energy is still below the energy of the absorption edge, the incident photon can excite an electron to a virtual level. The "relaxation" from this state emits a photon with a resonant Raman energy $E_{R\alpha}$ or $E_{R\beta}$, which is shifted to the actual fluorescence energy by $\Delta E = E_{edge} - E_0$. See [4] and [45] for further reading on this effect.

Fig. 12 shows the contributions of the inelastic signals compared to the elastic peak at 9 $Å^{-1}$ at the Ge near edge of $Ag_{0.50}(GeSe_3)_{0.50}$. The actual share of the inelastic scattering in the energy range covered by the analyzer is rather small, i.e. usually less than 0.1% (confer as well fig. 14 in the next subsection). Nevertheless, the inelastic contributions have to be closely inspected, since the contribution to the measured intensity exhibits a complex Q-dependence. This is especially important for the calculation of the differential structure factors $\Delta_k S(Q)$, since the difference in intensity is only in the order of magnitude of a few percent.

Normalization The x-ray detecting system cannot provide an absolute scale for the measured photon intensity. It is therefore necessary to normalize the acquired data to atomic units after all correction schemes described before have been applied. A method that is commonly employed has first been described by Krogh-Moe [46] and Norman [47]. Therein, a normalization constant C is calculated, which is defined by

$$I_{\text{absolute}} = C \cdot I_{\text{experimental}}. \tag{3.6}$$

The constant C has already been introduced in eq. 2.11. Further details are provided in the original papers cited above. For multi-component chemical systems, C takes the following form:

$$C = \frac{\int_{Q_{min}}^{Q_{max}} \frac{\overline{f^2}}{\overline{f}^2} \cdot Q^2 dQ - 2\pi^2 \rho_N}{\int_{Q_{min}}^{Q_{max}} \frac{I(Q)}{\overline{f}^2} \cdot Q^2 dq}. \tag{3.7}$$

Technically, the lower and the upper limit for the integrals in eq. 3.7 should be zero and infinity, respectively. Naturally, only the minimal and the maximal value reachable in the experiment, Q_{min} and Q_{max}, can be used. The resulting error has been approximated for a typical Cu K_α diffraction experiment in the range 0.5-5Å^{-1} to be about 1% [46]. A larger Q-range reduces this error.

It should be noted that whereas the error resulting from the limited experimental Q-range is negligible in a usual x-ray scattering experiment, it may become problematic for the calculation of differential intensities. The normalization procedure therefore needs to be carefully checked in the case of the anomalous scattering experiments.

3.2.3 Definition of the absorption edge

The setup at the synchrotron facilities necessitates the determination of the absorption edge prior to each scattering experiment. Another reason for this step is that the actual position of the absorption edge may vary to some extent in a condensed sample due to the environment around the specific element. These problems are solved by first calibrating the incident energy employing a standard sample containing the desired element (usually a pure element). In a second step the sample is adjusted in the x-ray beam and the absorption edge is measured by the fluorescence radiation emitted from the sample as a

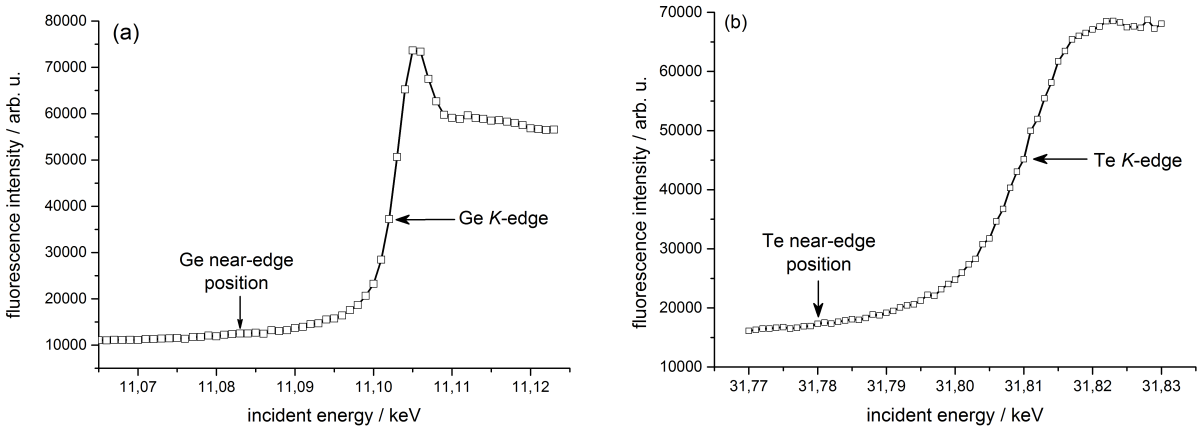

Figure 13: Exemplary energy scan to define (a) the Ge K-edge in $Ag_{0.15}(GeSe_3)_{0.85}$ and (b) the Te K-edge in $Ge_8Sb_2Te_{11}$. The position of the near-edge measurement (20-30 eV below the absorption edge) is indicated as well.

function of the energy of the incident radiation, which is varied about ±40 eV around the absorption edge. Thereby, the edge position is defined within an accuracy of ±1eV. Figure 13 a) displays such an energy scan around the Ge K-edge in $Ag_{0.15}(GeSe_3)_{0.85}$. Note that each edge possesses a unique form connected to the electronic structure of the element, as illustrated by a comparison with e.g. the Te K-edge in $Ge_8Sb_2Te_{11}$ shown in fig. 13 b).

3.2.4 Analyzer specific corrections

The previously described corrections to the data measured in a scattering experiment have been straightforward in the sense that they are needed for any diffraction experiment as a matter of principle. However, the practical implementation of the AXS setup usually requires the use of an analyzer crystal for secondary monochromatisation, in order to achieve the desired energy resolution. The use of such a device demands another correction procedure due to several factors, among else an imperfect alignment, inhomogeneity of the x-ray beam and the mosaicity of the crystals. This effect will be discussed in the following, and the differences of the two monochromator crystals at BM02/ESRF and at BL13XU/SPring-8 will be emphasized.

Bent graphite crystal At BM02/ESRF, a bent graphite crystal with a resolution of about 60 eV for energies in the range of the Ge K edge was employed for the AXS experiments, cf. table 3. The analyzer position is usually optimized at the $S(Q)$ maximum

around $Q = 2$ Å^{-1} for the investigated samples. As mentioned above, a scan of the angular position of the monochromator crystal is equivalent to measuring the energy spectrum of the scattered radiation. Thus, the angular position of the crystal can be translated into a corresponding energy, as shown in the two axis labels in fig. 14. Such a scan is performed at several Q-values after each measurement.

However, due to the problems mentioned above, a continuous shift of the x-ray beam on the monochromator crystal as a function of Q is often observed, manifested as a shift of the elastic peak in the analyzer scans, as shown in fig. 14 for the Ge near and far edges in $Ag_{0.50}(GeSe_3)_{0.50}$. Note that the energy axis in this case is only applicable to the scans near the Q value where the analyzer position has been optimized. For the other scans, the energy axis is actually shifting in such a way that the maximum of the curve corresponds to the elastically scattered radiation (11.083 keV and 10.903 at the Ge-near and far edge, respectively). However, since no correction of the analyzer position has been applied during the measurement, the situation in fig. 14 represents the intensity distribution actually observed in the experiment.

Figure 14 thus suggests that the measured intensity is too small in the high-Q region. A solution for this problem is to compare the intensity at the actual position of the analyzer crystal during the measurement (represented as a dashed line in fig. 14) and the intensity at the maximum of the elastic peak. The ratio between both quantities is visualized in fig. 15 a) for the scans shown in fig. 14. In this case, the effect is comparably small and the curves for the Ge near and Ge far edge only differ in the region above 7 Å^{-1}. However, the effect can be more prominent for different experiments and as a function of Q, as exemplarily shown in fig. 15 b) for the Ag edge in $Ag_{0.15}(GeSe_3)_{0.85}$. The data points in figures 15 a) and 15 b) have been fitted with a sigmoidal function, which was found to describe the data generally very well.

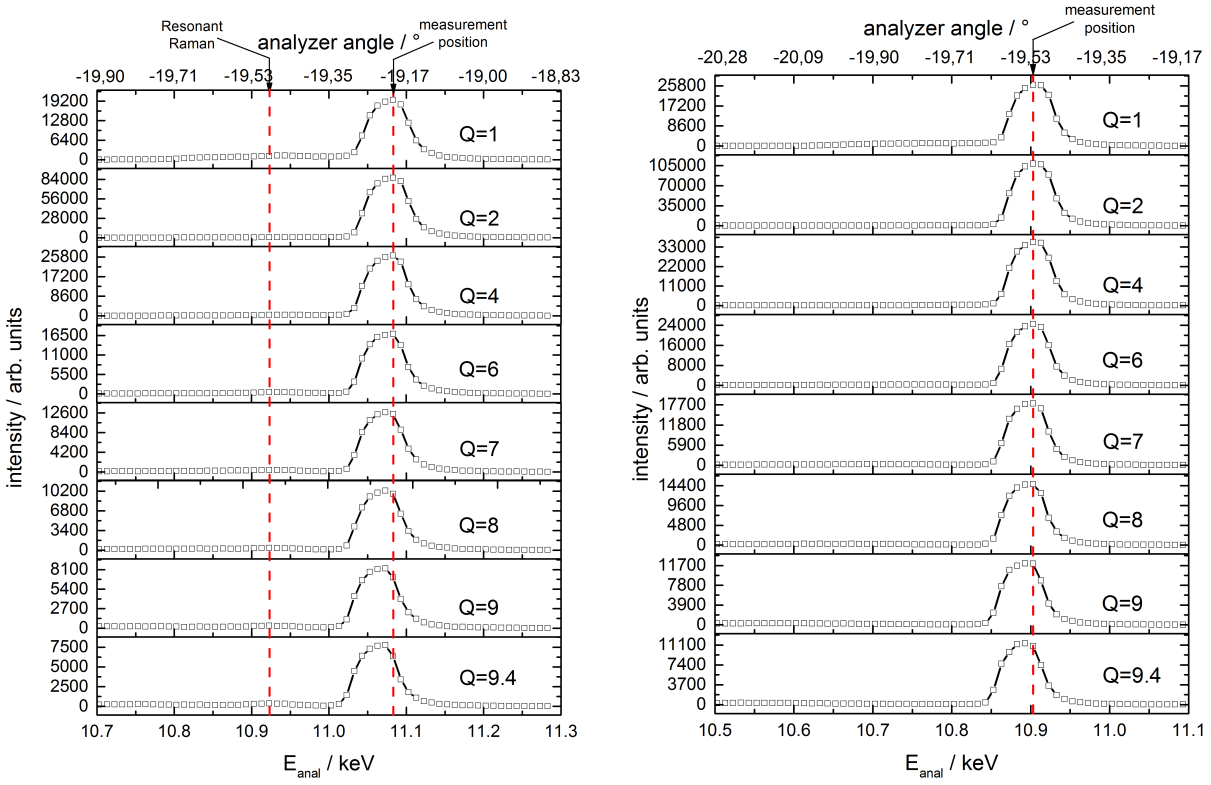

Figure 14: Analyzer scans at the Ge near (left) and far (right) edges for $Ag_{0.50}(GeSe_3)_{0.50}$ using a bent graphite crystal. The analyzer position during the measurement and the position of the resonant Raman scattering are marked with dashed lines. The energy axis is only strictly applicable for the scan at $Q = 2$ Å^{-1} (see text).

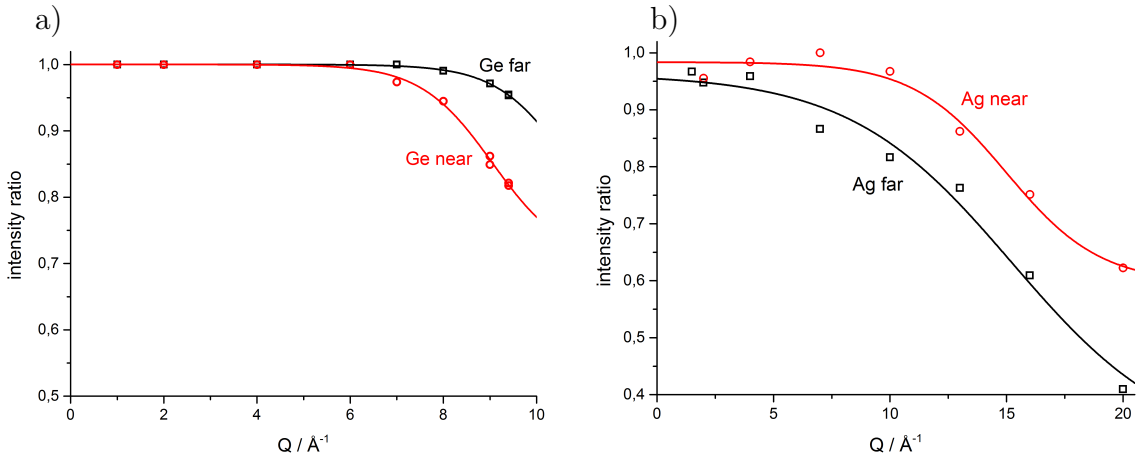

Figure 15: Ratio of the intensity at the peak position of the elastic signal and the actual measurement position extracted from fig. 14 (a) and for the Ag edge in $Ag_{0.15}(GeSe_3)_{0.85}$ (b).

LiF crystal The lithium fluoride crystal currently employed at BL13XU/SPring-8 offers a much higher energy resolution, see tab. 3. This is beneficial in order to completely discriminate the inelastic scattering contributions, but was found to produce a more complex behavior of the analyzer scans. An example is shown in fig. 16; the intensity ratios described above are depicted in fig. 17 and they are fitted with simple polynomial functions. In this case, the correction of this effect is crucial for the data reduction and would be difficult to perceive in the resulting structure factor. Note that neither the resonant Raman signal nor the Compton scattering can be seen in fig. 16 due to the high energy resolution of the LiF analyzer crystal. This is emphasized in fig. 18, which provides a full view of the analyzer scan at 2 $Å^{-1}$; the peak width is about 9 eV, whereas the resonant Raman signal is expected about 130 eV below the incident energy.

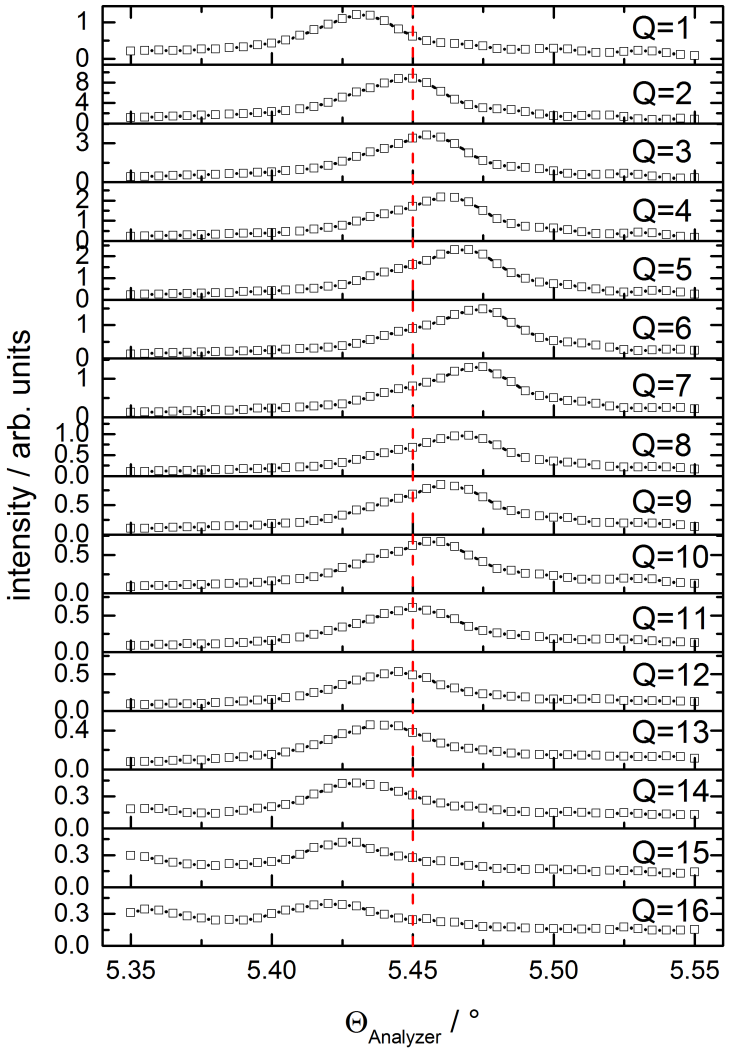

Figure 16: Analyzer scans at the Te far edge for $Ge_1Sb_4Te_7$ using a LiF analyzer. The analyzer position during the measurement is marked with a dashed red line.

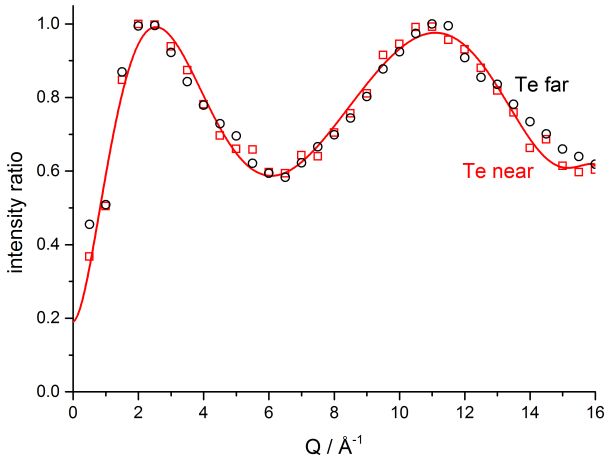

Figure 17: Ratio of the intensity at the peak position of the elastic signal and the actual measurement position extracted from fig. 16. Similar curves are obtained for Te near and far edge.

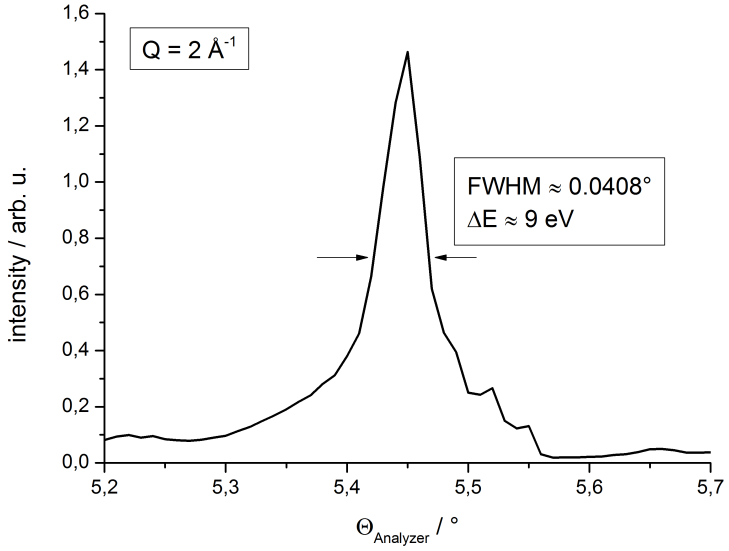

Figure 18: Full view of the analyzer scan at 2 $Å^{-1}$ from fig. 16.

3.3 Methodology

For the **RMC modeling** procedure, the RMC_POT program package by Gereben et al. was employed [20–22]. This program is a C++ implementation of the Reverse Monte Carlo algorithm and was already outlined in section 2.3.

Ring statistics offer the possibility to characterize the topological connectivity of a given network, and were calculated using the R.I.N.G.S. program v1.2.6 (Rigorous Investigation of Networks Generated using Simulations) [48]. A "ring" is defined as a closed path of covalent bonds originating from and leading back to the same atom. For the ring statistics analysis, irreducible rings were searched in the amorphous network, i.e. closed paths that cannot be decomposed into smaller rings. The basis for the calculations is a section of about 2000 atoms, taken from the configurations obtained by RMC, distributed in a cubic box with periodic boundary conditions. The obtained ring distributions are based on the numbers of rings per atom, normalized to the total number of atoms in the network.

***Ab-initio* Molecular Dynamics simulations** (AIMD) have been performed by Akihide Koura of the group of Prof. Shimojo (Kumamoto University). The simulations were based on density functional theory with a generalized gradient approximation (GGA) using the PBE functional [49] with an empirical dispersion correction term (DFT-D2) [50] for the exchange–correlation energy. The electron-ion interaction was described by projector augmented wave (PAW) potentials [51]. Only the valence electrons were treated explicitly, i.e. the configurations $4s^2\ 4p^2\ 4d^0$ for Ge and $5s^2\ 5p^4\ 5d^0$ for Te. The electronic wavefunctions and electron density were expanded using plane wave basis sets with cut-off energies of 9 and 90 Ry (i.e. 122 eV and 1224 eV), respectively. Only the Γ point was used to sample the Brillouin zone of the MD supercell. An ensemble of 216 atoms (108 Ge and 108 Te) was used with periodic boundary conditions. In a first step, the equilibrium state was obtained by an isobaric-isothermal simulation at 300 K and ambient pressure. In a second step, a canonical ensemble was simulated for 20 picoseconds using the number density obtained from the previous step, which were 0.0315 atoms/Å^3 and 0.0333 atoms/Å^3 for the simulation without and with dispersion correction, respectively. It may be noted that the latter value shows a very good agreement to the experimental value of 0.0337 atoms/Å^3.

3.4 The AXS/RMC approach summarized

The following section gives a summarized overview about the approach of using anomalous scattering in combination with Reverse Monte Carlo simulations. The complete method is illustrated in fig. 19. The experimental data, which have been gathered as an intensity in arbitrary units as a function of the scattering angle 2Θ, are expressed by the scattering vector Q and corrected for intrinsic (absorption, inelastic scattering, normalization) and extrinsic (e.g. imperfect alignment) contributions, yielding a normalized intensity $I(Q, E_k)$ at various incident energies near absorption edges of element k. Using tabulated or measured form factors f, total structure factors $S(Q)$ or differential structure factors $\Delta_k S(Q)$ are calculated. These quantities can already be interpreted in terms of their Fourier transformation, which gives the total pair distribution function $g(r)$ and the differential pair distribution function $\Delta_k g(r)$.

The experimentally obtained data in reciprocal space are used as input for a subsequent RMC simulation, which also requires the matrices of the respective weighting factors $\Delta_k w_{ij}(Q)$ and $w_{ij}(Q)$. The RMC simulation then aims to minimize the difference between the experimental data and a given three dimensional configuration by minimizing the squared sum of errors χ^2. The parameters for the simulations, e.g. the cut-off distances, simulation time, weighting factors σ, system size etc., have to be chosen carefully and adjusted to the considered system. When the simulation is converged, the obtained configuration can be analyzed in real space by the partial structure factors $g_{ij}(r)$ in terms of (partial) coordination numbers, interatomic distances, bond angle distributions etc., and it can also be investigated in reciprocal space by the partial structure factors $S_{ij}(Q)$, e.g. with respect to the first sharp diffraction peaks or other signals at low Q-values which contain information about the intermediate-range order, or with respect to the dominant peak which contains information e.g. about the extended-range order.

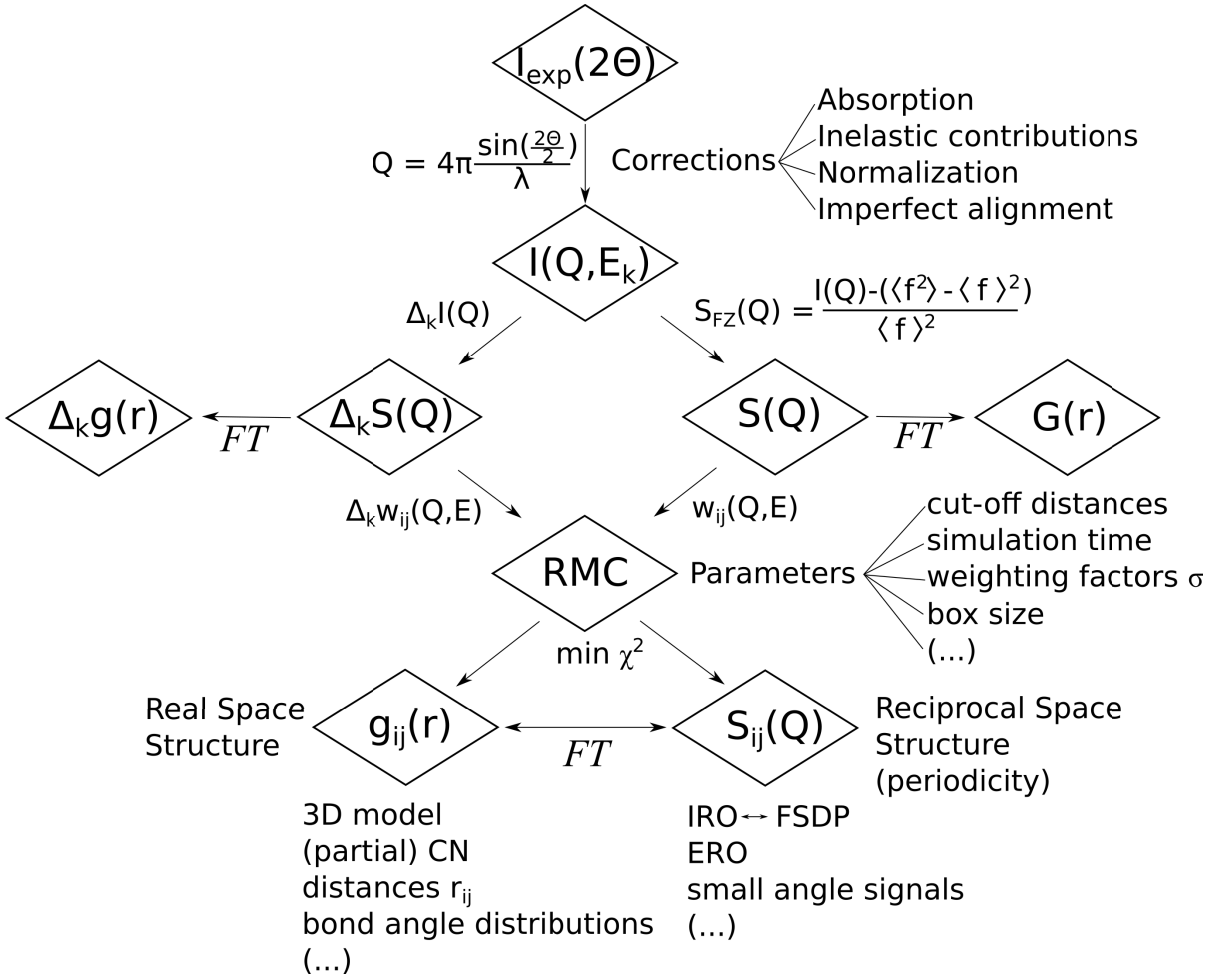

Figure 19: Flow chart of the AXS/RMC method, indicating important steps and parameters.

Part II

Data evaluation and discussion

4 Ag-GeSe$_3$ glasses

The ternary system Ag-Ge-Se has undergone extensive research in the last two decades. Therein, silver can be regarded as an additive to the Ge-Se glassy system, inducing different effects that make the system interesting for the application in data storage devices or as a solid electrolyte. At room-temperature, it is found that glasses are able to form in two distinct regions in the Se rich corner of the Ag-Ge-Se phase diagram as shown in figure 20. These regions, however, do not denote areas of similar properties or structures: Within the disordered state, major changes are observed in the atomic structure and in macroscopic properties like crystallization temperature and electrical conductivity. Of special interest is the pseudo-binary line between Ag and GeSe$_3$. Along this line, compositions exhibiting fast ionic conductivity are found.

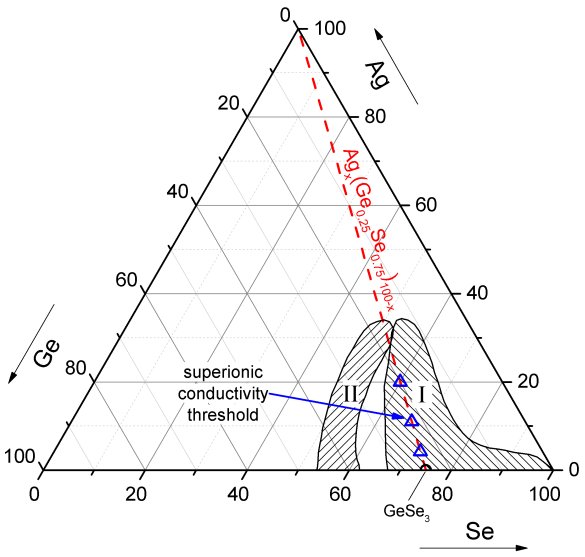

Figure 20: Ternary phase diagram for the system Ag-Ge-Se. Compositions of interest in this study are marked as blue triangles. The hatched areas (denoted I and II) indicate glass forming regions; data were taken from [52].

Such superionic conducting materials are of growing interest in fundamental and applied materials' science, as they can e.g. be employed as electrolytes in solid-state batteries. A different area with high potential for wide-spread application is the so-called programmable metallisation cell or PMC, as proposed by Kozicki [53, 54], which utilizes the unique properties of these glasses. A PMC consists of individual cells of about 100 nm in size, which contain the electrolyte between two solid electrodes. In the initial state, the electrical resistance of such a cell is high, as the glass is a poor electronic conductor. This

is state '0'. Applying an electrical potential in the order of magnitude of a few hundred mV causes the electrical resistance to decrease significantly after a short time. The current view of this process is that the applied potential causes a local reduction of Ag ions to Ag atoms, which subsequently form small metal-like clusters, and eventually generate so-called "nanopaths" from one electrode to the other. Due to its metallic character, the electrical resistance then drops by some orders of magnitude, thus constituting a state '1'. A schematic overview has been given in the introduction (fig. 1), and more detailed description and further information are reported e.g. by Cuello [55].

It is well-known that superionic behavior in Ag containing chalcogenide glasses is observed at room temperature, such as for Ag-$GeSe_3$ alloys, in contrast to high temperatures needed in crystalline superionic conductors like AgI. Another advantage of these glasses as electrolytes is that the glassy state can easily be obtained in a wide concentration range by simple water or even air-quenching due to the high glass-forming ability of these compounds.

In the system $Ag_x(GeSe_3)_{1-x}$, a sharp jump of about eight orders of magnitude in the ionic conductivity is observed for $x > 0.33$ (corresponding to Ag concentrations of about 11 at%), where a superionic conducting phase is formed, cf. fig. 21 [31, 56]. The ionic conductivity of this phase is situated in the region 10^{-5} - 10^{-4} S/cm. The exact position of the jump is somewhat controversial and has been reported with $x = 0.3$ [31] or $x = 0.26$ [56], both determined by impedance measurements.

Based on thermodynamic data (i.e. glass transition and crystallization temperature measurements), Kawasaki et al. propose that three concentration regions should be differentiated: A region with low Ag concentrations and low conductivity between $0 \leq x \leq 0.2$, an intermediate region between $0.2 < x < 0.33$ and a region with high Ag concentrations and high ionic conductivity for $0.33 \leq x$ [31]. A large number of studies focuses on the structure of the superionic conducting phase: For a wide range of Ag contents, the structural properties have been studied by Piarristeguy and coworkers by standard x-ray [57, 58] and neutron diffraction [59]. Ohara, Kumara and coworkers analyzed the structure by means of high-energy x-ray scattering, neutron diffraction and EXAFS [60, 61], and most recently, our group discussed properties of the composition with $x = 0.50$ by anomalous x-ray scattering and reverse Monte Carlo (RMC) modeling [62]. All studies agree that the average coordination number of silver is remarkably high, with a value of

3 or more. Furthermore, chain-like fragments of Ag atoms can be clearly observed. But despite the large number of studies, a detailed analysis of the intermediate range order (IRO) of Ag-$GeSe_3$ glasses is still lacking. The IRO is known to be a dominant feature in the structure of chalcogenide glassy systems, e.g. the Ge-Se network in Ge_xSe_{1-x} glasses [63]. Yet it is difficult to resolve such structures by total scattering and/or EXAFS data alone, as pointed out by Waseda [13].

To achieve a more detailed insight into the structural basis of the superionic conduction threshold on the short- and intermediate length scale, anomalous x-ray scattering (AXS) experiments were performed on $Ag_{0.15}(GeSe_3)_{0.85}$ and $Ag_{0.50}(GeSe_3)_{0.50}$ at x-ray energies close to the Ge, Se and Ag K-absorption edges, combined with Reverse Monte Carlo simulations (RMC). The atomic fractions of silver in these compounds are 4.2% and 20%, respectively. For simplicity, they will therefore correspondingly be referred to with the abbreviations Ag4 ($x = 0.15$) and Ag20 ($x = 0.50$) in the following. For the composition with 11 at% Ag, i.e. $Ag_{0.33}(GeSe_3)_{0.67}$, only measurements at the Ag K-edge were conducted due to a limited amount of beamtime. This composition will therefore not be included into a RMC simulation, but the differential data at the Ag edge will be used to emphasize the trends found in this structure factor along the *tie*-line. The other two compositions, however, already provide a substantial insight into the structural properties that distinguish the fast ion conducting phase from the insulating phase.

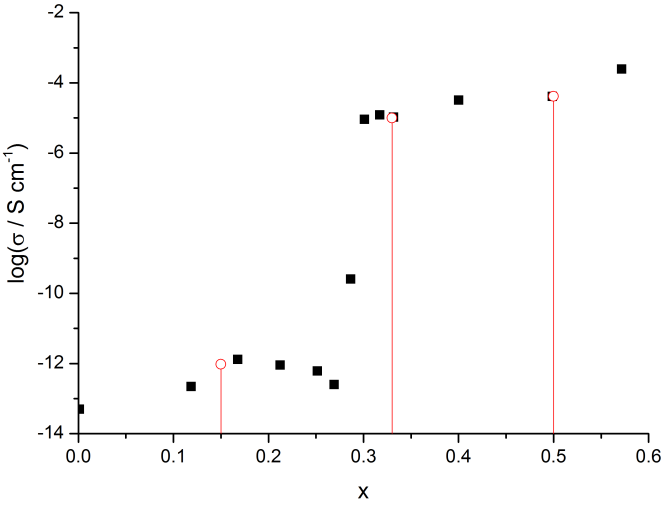

Figure 21: Ionic conductivity σ in $Ag_x(GeSe_3)_{1-x}$ as a function x. Data are taken from [31]. Black squares indicate data measured by Kawasaki et al. and red circles indicate the compositions investigated by AXS.

Table 4: Overview about the AXS experiments conducted for the $Ag_x(GeSe_3)_{1-x}$ glasses.

Composition	Edge (energy)	Experiment	Prim. intensity / data point
Ag4 (x=0.15)	Ge (11.103 keV)	HC-1137	$2.5{\cdot}10^6$ / cts
	Se (12.658 keV)	HC-1137	$1.9{\cdot}10^6$ / cts
	Ag (25.514 keV)	HD-602	$2.5{\cdot}10^6$ / cts
Ag11 (x=0.33)	Ag (25.514 keV)	HD-602	$2.5{\cdot}10^6$ / cts
Ag20 (x=0.50)	Ge (11.103 keV)	HC-1137	$2.5{\cdot}10^6$ / cts
	Se (12.658 keV)	HC-1137	$1.5{\cdot}10^6$ / cts
	Ag (25.514 keV)	HD-602	$2.5{\cdot}10^6$ / cts

4.1 Raw data and applied corrections

The details of the experiments on the AgGeSe glasses are summarized in tab. 4. Figure 22 illustrates the raw data measured at each absorption edge. Since the experiments were conducted in reflection geometry with thick samples, no absorption corrections have been necessary. Corrections due to the analyzer crystal as described in section 3.2.4 are found to vary to some extent between the individual scans, but the intensity ratios can be well described in all cases using a simple sigmoidal function, as shown in figure 23. Major deviations are found in the measurements at the Ge absorption edge, especially in Ag4. Although corrections based on these intensity ratios are possible, the loss in the statistical quality of the data in the high-Q region is not negligible: At the Ag edges, for example, only between 50% and 80% of the nominal intensity is available for $Q > 10$ Å^{-1}. Since the effect adds up for two absorption edges, an additional statistical error is observed for the differential datasets. Further improvement of the experimental method should therefore target this effect in order to achieve a better contrast in the high-Q region.

The total structure factors $S(Q)$ obtained from the corrected data by equation 2.11 and the differential structure factors at the Ag edge calculated by eq. 2.20 are shown in figure 24 for the three measured compositions. All total $S(Q)$'s exhibit a very similar shape, except that the first sharp diffraction peak near 1 Å^{-1} and the intensity of the two following peaks decrease with increasing Ag content. This development is even more pronounced for the $\Delta_{Ag}S(Q)$'s, in which the FSDP decreases more drastically. A detailed discussion of all structure factors for Ag4 and Ag20 follows in the next section, taking into account relevant corrections applied during the RMC modeling scheme.

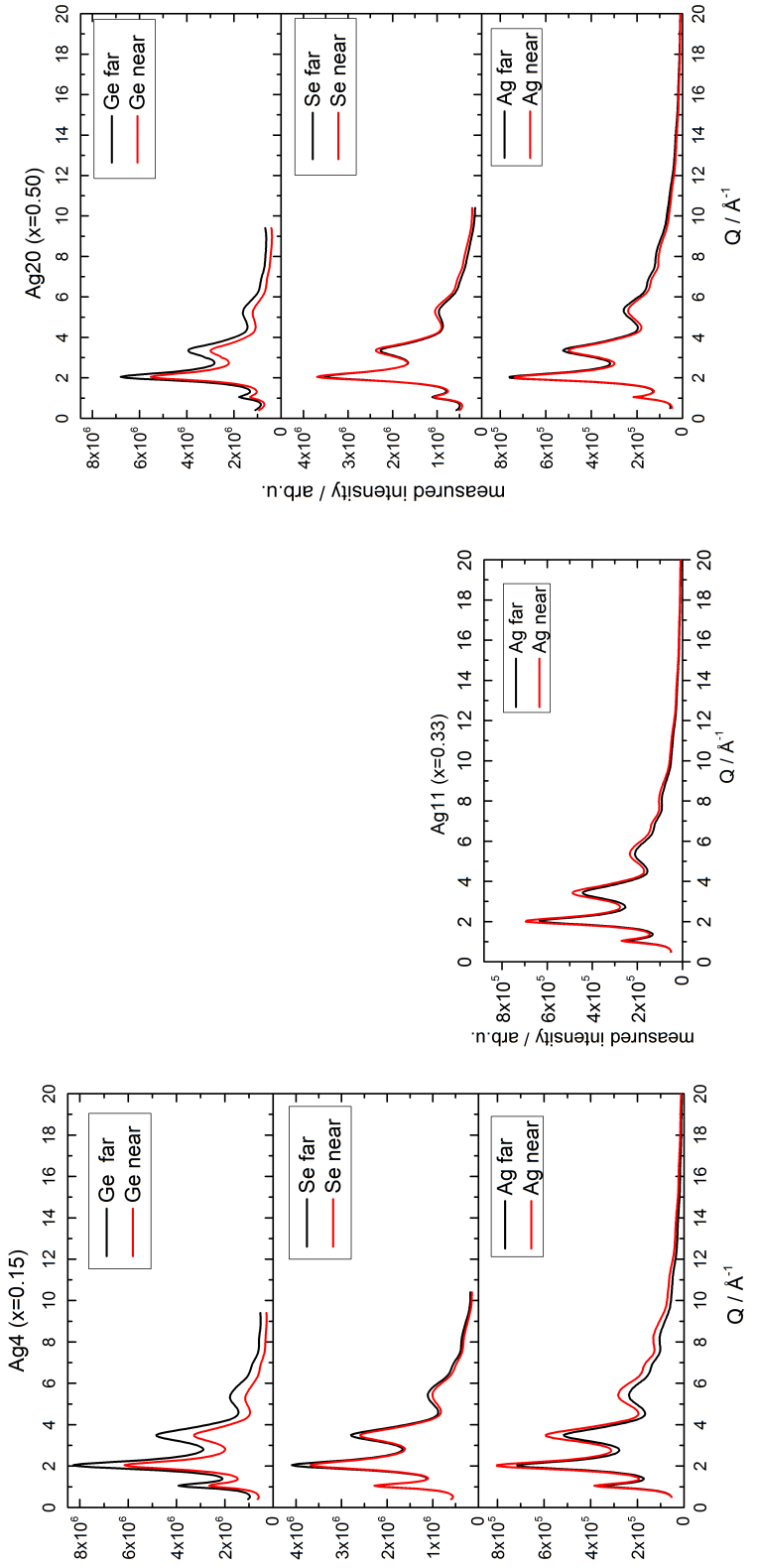

Figure 22: Raw data $I(Q)$ measured for the three Ag-GeSe$_3$ glasses at the Ge, Se and Ag K edges. Note that only the Ag edge was measured for Ag11 (i.e. $x = 0.33$).

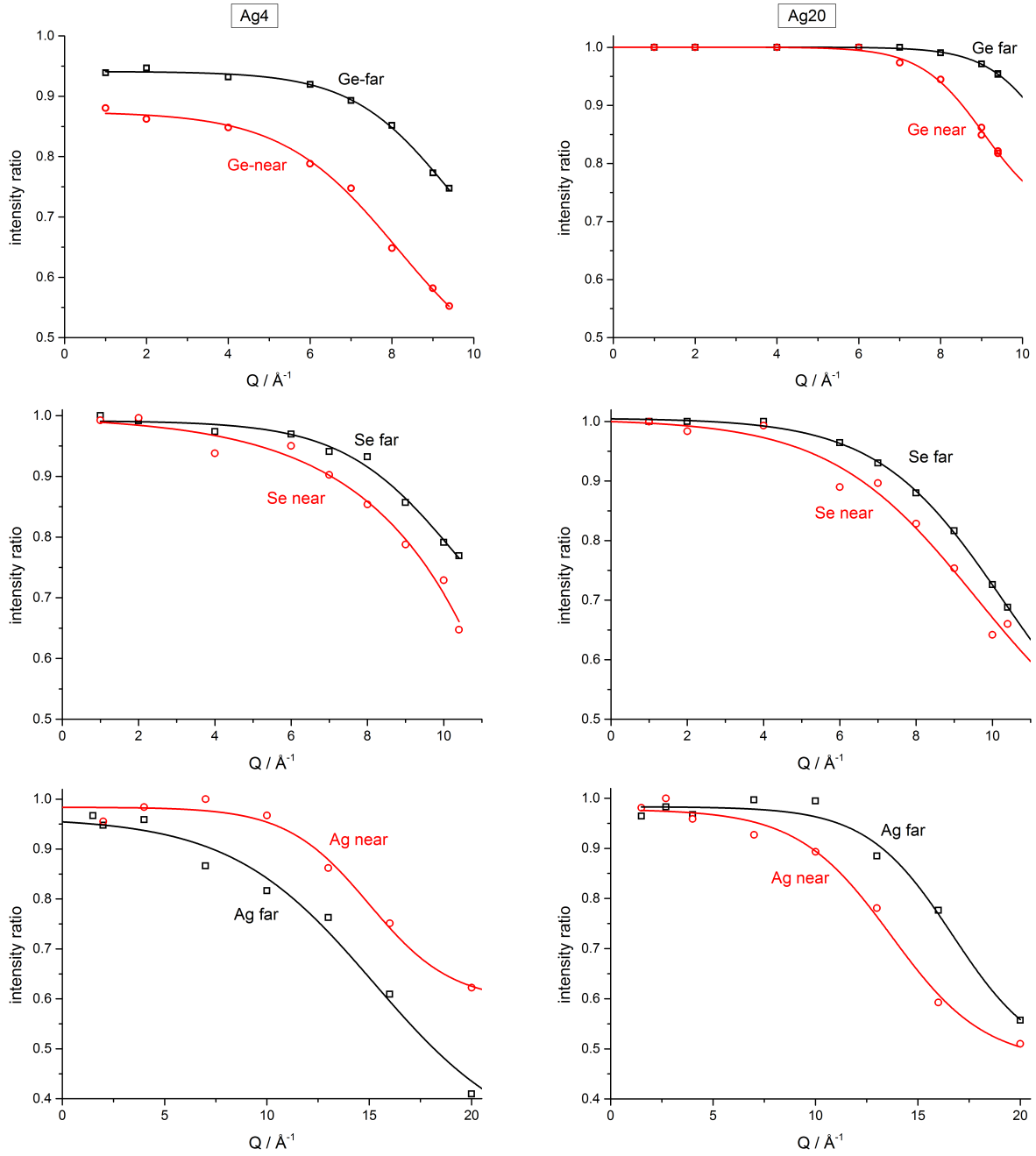

Figure 23: Intensity ratios of the actual measurement and the maximum of the elastic peak as described in section 3.2.4. Respective functions for the compositions $x = 0.15$ (Ag4) are displayed on the left, and for $x = 0.50$ (Ag20) on the right.

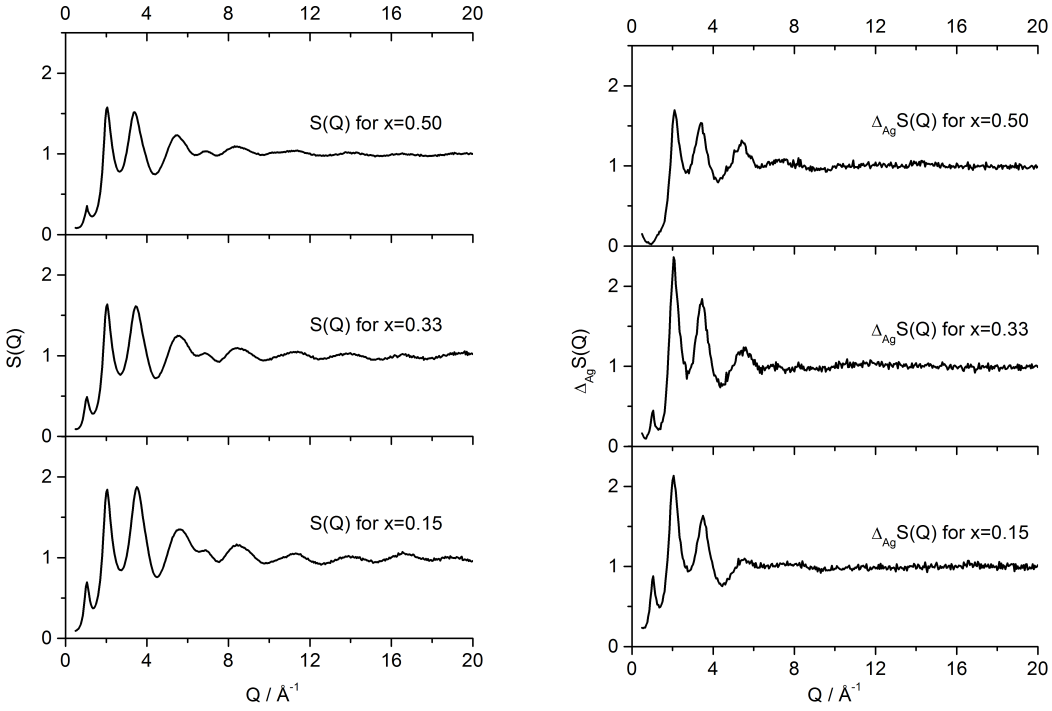

Figure 24: Total structure factors $S(Q)$ and differential structure factors at the Ag edge $\Delta_{\mathrm{Ag}}S(Q)$ calculated from the raw data after complete data correction, for the three compositions.

4.2 Reverse Monte Carlo Simulations on Ag-GeSe$_3$

An input configuration was chosen with proper stoichiometry of 10,000 atoms for Ag20 and 24,000 atoms for Ag4, randomly distributed in a cubic box corresponding to the number density of $\rho_{\mathrm{N,Ag20}} = 0.03758$ and $\rho_{\mathrm{N,Ag4}} = 0.03483$ atoms/Å^{-3} (cf. [57]), respectively. Note that no modeling was performed for Ag11, since measurements at the Ge and Se absorption edges were not conducted. The larger number of atoms for Ag4 was chosen as to appropriately model the Ag based correlations, since the content of Ag atoms is only 4.23%. Minimum atomic distances were defined in order to avoid unphysical configurations as 2.9, 3.1, 2.5, 3.1, 2.1, and 2.1 Å for the Ag-Ag, Ag-Ge, Ag-Se, Ge-Ge, Ge-Se, and Se-Se distance, respectively. The values for the Ge-Ge and Ag-Ge distances were chosen to ensure that these bonds do not contribute to the first coordination shell, marked by the minimum in the total pair correlation function $g(r)$ at 3.0 Å, because the existence of such bonds has been disproved by EXAFS measurements [61]. Both values were increased for Ag20 to 3.3 Å in order to appropriately model the second coordination shell. It was verified in both compositions that the R_w factors of the RMC simulation are

not significantly affected by this constraint. After confirming a coordination number of about 4 for the Ge-Se bond in each simulation, a weak bond angle constraint has been applied subsequently to ensure a tetrahedral bonding coordination of Se around Ge atoms. Furthermore, for Ag4, the number of Se-Se bonds was initially found to be considerably higher than in comparable experiments (cf. table 6), so that a Se-Se coordination number constraint was applied as well.

The total and differential structure factors calculated from the experimental data together with the best fits obtained from the RMC simulation are displayed in fig. 25. The total structure factors obtained from the AXS experiments agree well with the $S(Q)$ data from other diffraction experiments [58, 64]. In all Ag-$GeSe_3$ compositions in ref. [58], a small first sharp diffraction peak can be seen in the low-Q region at $Q_1 \approx 1.05$ Å^{-1}. The intensity of this peak decreases steadily as a function of the Ag content x [58]. There are two peaks of similar intensity located at $Q_2 = 2.0$ Å^{-1} and $Q_3 = 3.4$ Å^{-1}. The last pronounced peak is rather broad and situated at about $Q_4 = 5.45$ Å^{-1}.

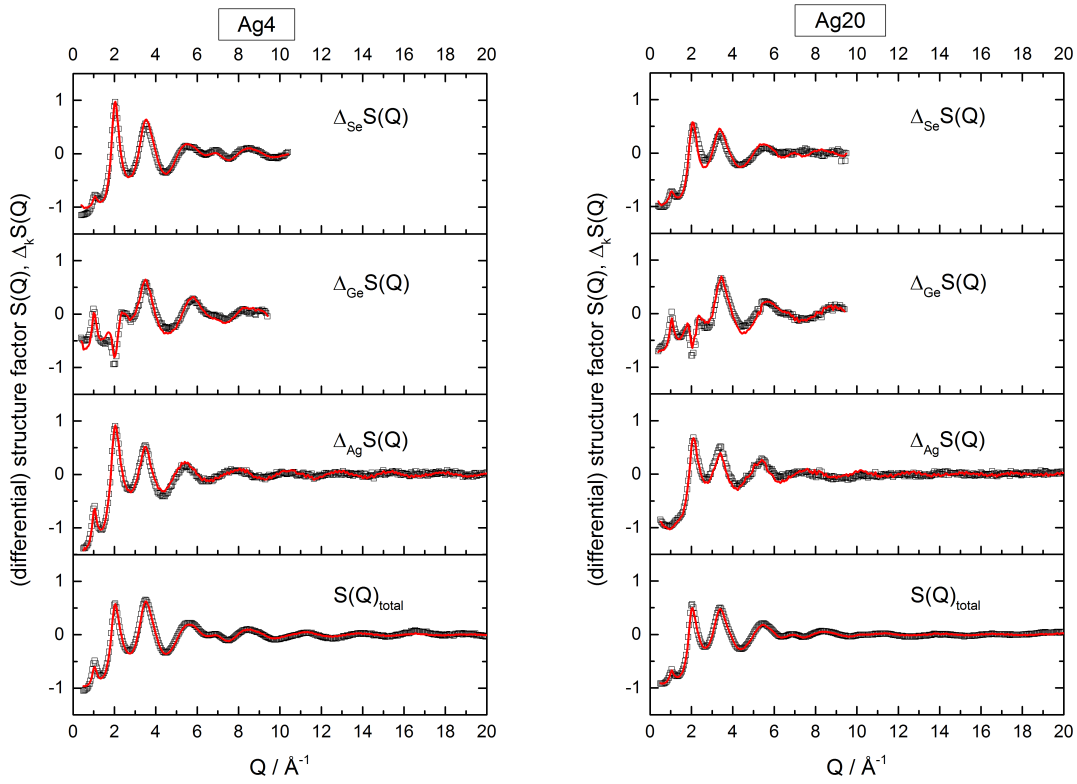

Figure 25: Experimentally determined total structure factor $S(Q) - 1$ at 25.214 keV and $\Delta_k S(Q) - 1$ around the Ag, Ge and Se K edges, for Ag4 (left) and Ag20 (right). Squares indicate data obtained from the AXS experiments, and solid curves denote the best fits by RMC modeling.

The differential structure factors $\Delta_k S(Q)$ coincide in their general form in both glasses. However, an important difference is the FSDP in $\Delta_{Ag} S(Q)$, which is quite pronounced in Ag4, but basically missing in Ag20. Only a small asymmetry towards the low-Q side of the Q_2 peak remains from the FSDP in the latter composition. It is noteworthy that the decrease in intensity of the FSDP as a function of x is well known in the literature only regarding the total structure factor (e.g. [57, 58]). On the other hand, the AXS experiments show that the FSDPs of the $\Delta_{Ge} S(Q)$ and $\Delta_{Se} S(Q)$ functions remain generally unchanged, and only the FSDPs in the Ag related functions decrease with x. Ag-based correlations are therefore expected to be the dominant reason for the reduction of the FSDP in the total structure factors.

The features of the $\Delta_{Se} S(Q)$ and the $\Delta_{Ge} S(Q)$ closely resemble the corresponding functions in pure $GeSe_3$ [63], except that the FSDP in the $\Delta_{Se} S(Q)$ of $GeSe_3$ is only visible as a small shoulder of the first structure factor peak. Otherwise, only slight differences are observed in the two Ag-$GeSe_3$ glasses under consideration, i.e. compared with Ag20, the minimum in $\Delta_{Ge} S(Q)$ at the Q_2 position is more pronounced for Ag4, and the peaks at Q_2 and Q_3 in $\Delta_{Se} S(Q)$ are more intense.

4.2.1 Partial structure factors

The partial structure factors obtained from the RMC modelling procedure are displayed in fig. 26. The weighting factors $W_{ij}(Q)$ for the different datasets are tabulated exemplarily for the position $Q = 2$ Å^{-1} in table 5, highlighting the enhancement of the edge-related partial contributions $S_{ij}(Q)$ to $\Delta_k S(Q)$ and the suppression of the other partials. It is found that the general form of the Se-Se and Ge-Se correlation coincides well for both compositions, indicating that the corresponding partial structural motives do not change considerably. The most notable contrast is that the signals at the Q_2 position (i.e. the peak in Se-Se and the dip in Ge-Se) are more pronounced in Ag20. The other $S_{ij}(Q)$'s, in contrast, exhibit major differences: whereas the Ag-Se correlation is very similar to the total $S(Q)$ in Ag4, it exhibits a minimum at the Q_2 position in Ag20. In addition, the peaks in the Ge-Ge, Ag-Ge and Ag-Ag correlations at the Q_2 position become much narrower in Ag20, and the Ag-Ag correlation also displays a more intense signal in the low-Q region. This low-Q feature of Ag20 can be interpreted as a sign for an emerging phase separation tendency, which has been a point of some debate in the superionic conducting

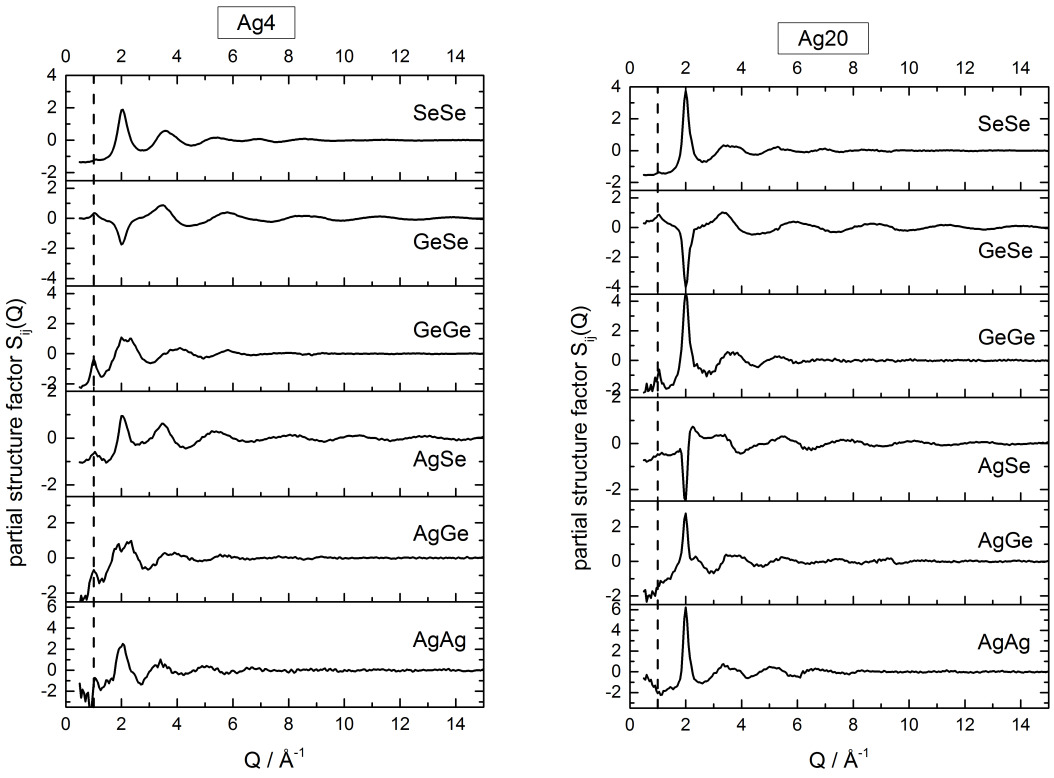

Figure 26: Partial structure factors $S_{ij}(Q) - 1$ obtained by RMC, for Ag4 (x=0.15) (left) and Ag20 (x=0.50) (right). The dashed line at $Q = 1$ Å^{-1} is a guide for the eye.

phase [61], and will be outlined in more detail in section 4.2.3.

The most striking difference, however, is the behaviour of the FSDP. Below the superionic conductivity threshold at about 11 at%, the FSDP is visible in every $S_{ij}(Q)$, though only with a small intensity in the Se-Se correlation. Such FSDPs are absent in all Ag based correlations for Ag20; nonetheless, they can be observed in the Se-Se, Ge-Se and Ge-Ge correlations, though they are less pronounced compared to those for Ag4. This indicates a high degree of intermediate range order in the low ionic conducting phase.

In GeSe$_3$, the FSDP was found to be majorly attributed to the Ge-Se and Ge-Ge correlations and has been considered to represent chains of GeSe$_4$ tetrahedra, which form a glassy network structure on the intermediate length level [58, 63]. Such a network, interspersed with Ag atoms, is also observed in the configurations obtained by RMC in the Ag-GeSe$_3$ glasses, and will be discussed in section 4.2.3. Piarristeguy et al. [58] interpreted the decrease of the FSDP in the total $S(Q)$ as a fragmentation of these GeSe$_4$ tetrahedra chains with rising content of Ag, based on the assumption that the FSDP is majorly related to the Ge-Ge correlation of neighbouring tetrahedra. The AXS/RMC results

presented here indeed reveal a slight reduction in the Ge-Ge related FSDP. However, it should be emphasized that the Ge-Ge correlation is not the major reason for the decrease of the FSDP in the total $S(Q)$. This effect is rather constituted by the reduction of the FSDPs in the Ag-based correlations. It may also be pointed out that a reduction of the FSDP upon addition of Ag is also observed in comparable systems, like germanium-sulfide glasses of similar composition (i.e. the Ag-GeS_3 system) [65].

Table 5: Weighting factors W_{ij} for each dataset, exemplary at Q=2.0 Å^{-1} near the first peak position in $S(Q)$, for Ag4 and Ag20.

	Dataset	AgAg	AgGe	AgSe	GeGe	GeSe	SeSe
Ag4	$S(Q)$	0.003	0.024	0.077	0.051	0.326	0.518
	$\Delta_{\mathrm{Ag}}S(Q)$	0.051	0.228	0.723	0.001	0.001	-0.003
	$\Delta_{\mathrm{Ge}}S(Q)$	0.000	0.058	0.008	0.181	0.677	0.077
	$\Delta_{\mathrm{Se}}S(Q)$	0.000	-0.001	0.070	-0.005	0.240	0.697
Ag20	$S(Q)$	0.059	0.088	0.280	0.033	0.209	0.331
	$\Delta_{\mathrm{Ag}}S(Q)$	0.234	0.184	0.582	0.000	0.000	0.000
	$\Delta_{\mathrm{Ge}}S(Q)$	0.003	0.251	0.034	0.138	0.516	0.058
	$\Delta_{\mathrm{Se}}S(Q)$	0.001	-0.005	0.298	-0.004	0.182	0.528

4.2.2 Partial pair correlation functions

The partial pair correlation functions $g_{ij}(r)$ obtained by RMC are displayed in fig. 27. Two coordination shells can be clearly distinguished: the first extends to about 3 Å (or 3.3 Å for the Ag-Ag correlation), and the second extends to about 4.5 Å, with maxima between 3.5 and 4.0 Å. Major differences in the $g_{ij}(r)$'s are observed in the homopolar Se-Se and Ag-Ag correlations: Firstly, $g_{\mathrm{SeSe}}(r)$ in Ag4 exhibits a sharp first coordination sphere around 2.4 Å, whereas the peak decreases in intensity and is partly superimposed by the second coordination sphere centered at 3.85 Å in Ag20. Secondly, the coordination number for the Ag-Ag correlation considerably increases from 0.08 to 0.45, with the peak centered near 3 Å. Note that this gain in the coordination number is related to the different concentration of Ag rather than the form of the $g_{\mathrm{AgAg}}(r)$'s.

Both compositions exhibit a distinct signal at 2.35 Å in the Ge-Se correlation with a coordination number of $n_{\mathrm{GeSe}} \approx 4$, indicating the tetrahedral coordination of Se around Ge atoms. Indeed, four-fold coordinated Ge atoms represent the dominant structural

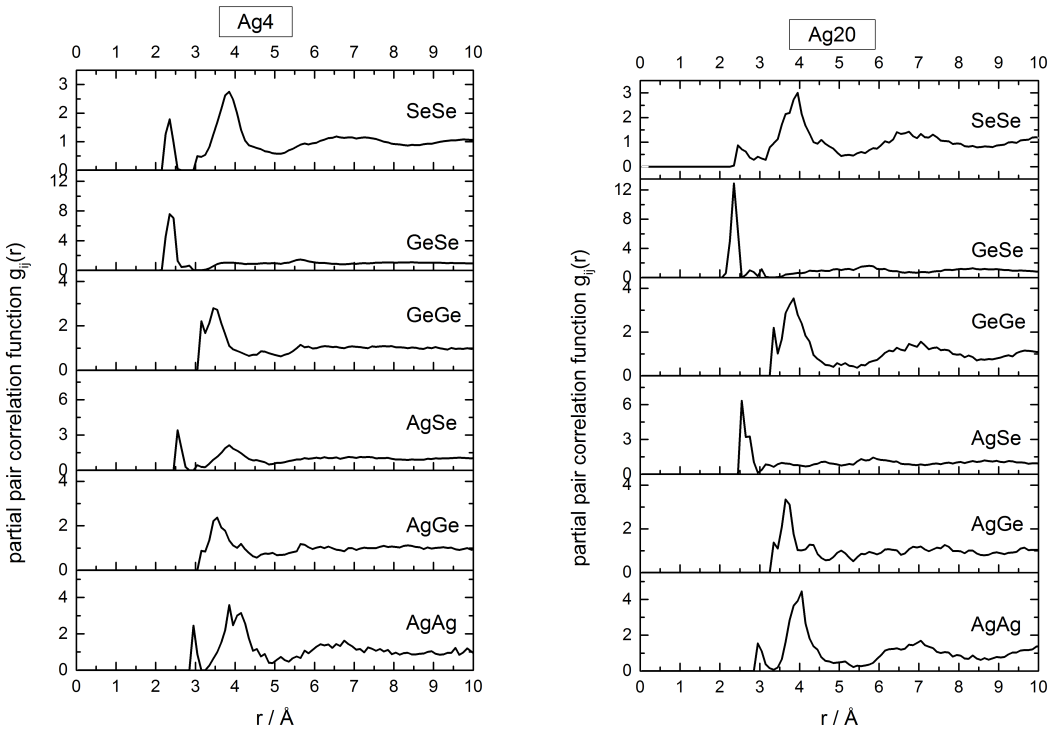

Figure 27: Partial pair correlation functions $g_{ij}(r)$ obtained by RMC, for Ag4 (left) and Ag20 (right).

feature: in Ag4 about 65% of all Ge atoms belong to this class, another 18% are five-fold coordinated. Comparable values are found in Ag20, where 68% of the Ge atoms are four-fold and 21% are five-fold coordinated. Also observed in both compositions is a peak at 2.6 Å in the Ag-Se correlation, though it is broadened in Ag20. Due to the applied constraints, Ge-Ge and Ag-Ge correlations only contribute to the second coordination sphere. The result of this SRO is a network of Ge-Se$_4$ tetrahedra, which is interspersed with Ag atoms. Figure 28 visualizes this network for both compositions.

Total coordination numbers for Ag and Se are much larger in Ag20 than in Ag4. Whereas the value for N(Se)=2.26 in Ag4 is comparably close to the value expected by the $8-N$ rule, Se adopts a coordination number close to 3 in Ag20. A similar trend is also observed for the Ag atoms. The resulting total average coordination number increases from 2.7 in Ag4 to 3.19 in Ag20.

A complete overview of all coordination numbers and interatomic distances extracted from the $g_{ij}(r)$'s is given in tables 6 and 7. The coordination numbers have been calculated by integrating the corresponding radial distribution functions to the respective minima after the first coordination shell. Figure 29 provides an example of the partition of the

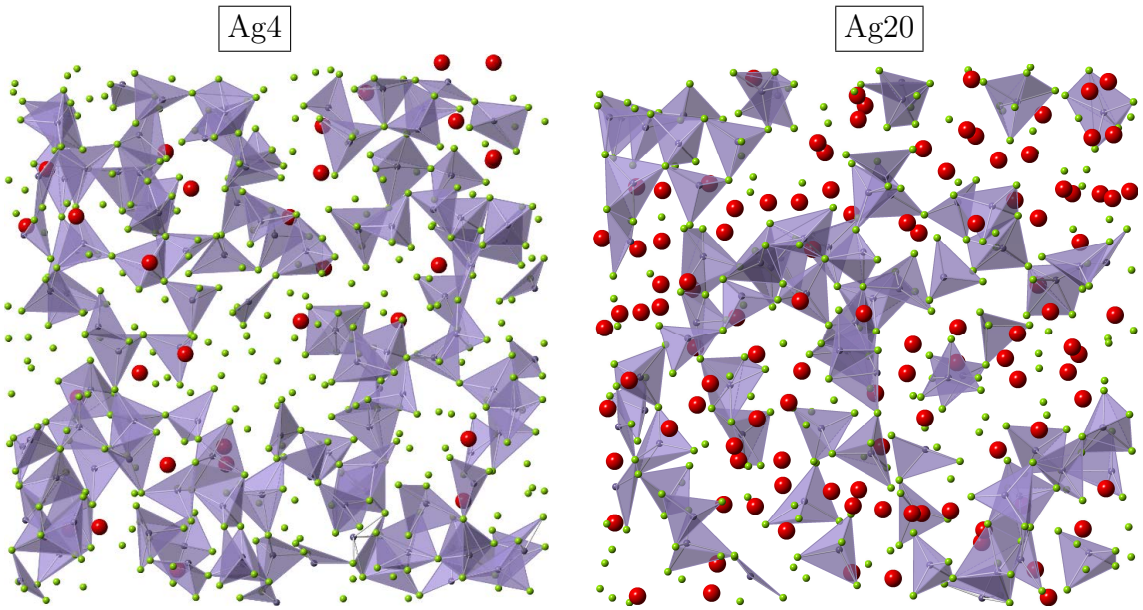

Figure 28: 32×32 Å^2 sections of the configuration of Ag4 (left) and Ag20 (right) obtained by RMC, showing Ge-Se coordination polyhedra (red: Ag, green: Se, blue: Ge).

RDF for the Se-Se and Ge-Ge correlation. It is easily seen that the small differences in the coordination numbers arise from a broadening of the first peak and from the slight asymmetry of the second peak in Ag20. The $n_{\mathrm{GeGe}}(r)$ show the missing "first" coordination shell and emphasize the higher degree of order in the third coordination shell of Ge-Ge. The results in tables 6 and 7 for all correlations are compared with other experimental data as follows:

1) For the low conducting phase (Ag4), the data are compared with results from AXS experiments on pure $GeSe_3$ [63] and from a total scattering experiment on a composition with 10 at% Ag [58].

2) For the superionic conducting phase (Ag20), a total scattering experiment on Ag20 [57, 58] and an EXAFS/RMC experiment on the composition $x = 0.565$ (24.5 at% Ag) [61] are taken as comparison.

It should be noted that though the focus of the study in [57, 58] is on the superionic conducting phase, it can be questioned whether the composition denoted $(Ge_{0.25}Se_{0.75})_{90}Ag_{10}$ is really part of this phase. According to [31], this composition would be situated in the intermediate phase between $0.2 < x < 0.33$. Though it is not explicitly discussed in [58], a transition of short-range order (SRO) parameters is observed between the compositions

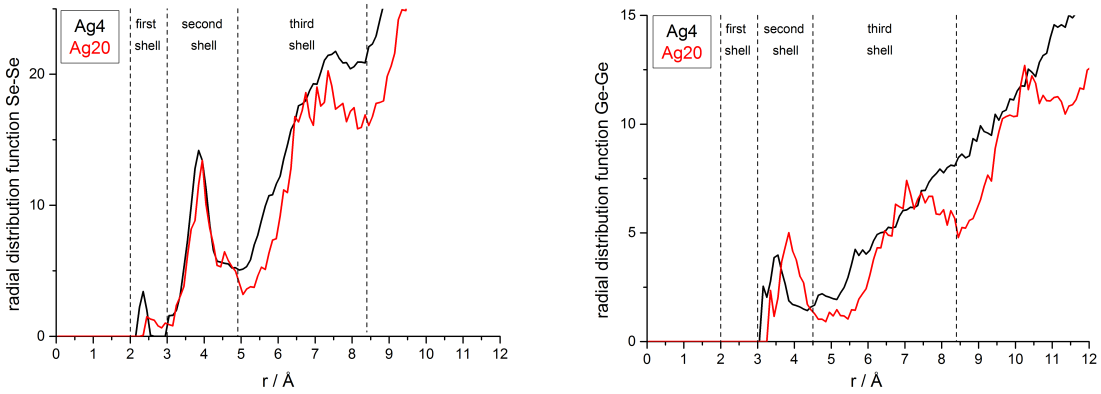

Figure 29: Radial distribution functions of the Se-Se (left) and Ge-Ge correlation (right); the coordination spheres assumed in the analysis are marked with dashed lines. Correlations of the Ag4 glass are displayed in black, and for the Ag20 glass in red.

containing 10 at% Ag (corresponding to $x = 0.31$) and compositions above 15 at% Ag ($x = 0.41$), mainly related to the Ag coordination which changes from 2 to 3. Due to a reasonable agreement with the parameters obtained for AXS on Ag4, it will be assumed in the following that the respective data in [58] refer to an insulating phase. It is interesting at this point to compare again the change in the short range order of the Ag-$GeSe_3$ glasses with the trends observed in the corresponding sulfide glasses Ag-GeS_3. In the pure GeS_3 glass, sulfur is two-fold coordinated, but the coordination number rises as a function of the Ag content and reaches 3 for 20 at% Ag [65]. The total coordination number of Ag rises as well, but is already as high as 2.9 at low concentrations of Ag [65].

In general, coordination numbers and distances in tables 6 and 7 are in reasonable agreement with the reference data. Coordination numbers obtained from EXAFS appear to be somewhat underestimated. It should also be taken into account that the total scattering experiments provide only a comparably low information content, thus explaining some differences in the obtained partial coordination numbers. It appears that Se obeys the $8 - N$ rule in pure $GeSe_3$ with a coordination number of 2, but becomes increasingly over-coordinated as a function of the Ag content. This trend is reproduced by Piarristeguy et al. [57, 58]. In addition, the increasing coordination of Ag was also found as well by Piarristeguy [57, 58] and by Kumara et al. [61], though their actual values are smaller. A notable exception from the generally good agreement is the total coordination number of Ge reported by Piarristeguy with N(Ge)=4.5. Such a high coordination is very unusual for Ge and indeed, this value also contradicts findings from EXAFS experiments [61].

Table 6: Partial and total coordination numbers of the first and second coordination shell obtained by AXS/RMC in comparison with other studies (see text). Coordination numbers have been calculated by integrating the respective coordination shells in the $g_{ij}(r)$ up to 3 and 4.5 Å, respectively (3.3 Å in case of the first CN of Ag-Ag).

	low conductivity phase			high conductivity phase		
	AXS[63]	this work	Mo-K_α[57, 58]	this work	Mo-K_α[57, 58]	EXAFS[61]
x	0	15	30.7	50	50	56.5
at%Ag	0	4.2	10	20	20	24.5
correlation	partial coordination numbers n_{ij}					
Ag-Ag		0.08	0.20	0.45	0.60	0.60
Ag-Ge		0.00	0.45	0.00	0.60	
Ag-Se		2.17	1.35	2.80	1.80	2.20
Ge-Ag		0.00	0.20	0.00	0.60	
Ge-Se	4.00	4.07	3.91	3.98	3.90	3.70
Se-Ag		0.13	0.20	0.93	0.60	0.90
Se-Ge	1.33	1.36	1.30	1.33	1.30	1.20
Se-Se	0.67	0.78	0.61	0.65	0.60	N/A
$Ag\text{-}Ag_{2nd}$		0.7		3.6		
$Ag\text{-}Ge_{2nd}$		2.9		2.6		
$Ag\text{-}Se_{2nd}$		8.5		(4.6)		
$Ge\text{-}Ge_{2nd}$		3.2		3.5		
$Se\text{-}Se_{2nd}$		10.5	11.0	9.2	10.7	
correlation	total coordination numbers $N(i)$					
N(Ag)		2.25	2.00	3.25	3.00	2.80
N(Ge)	4.00	4.07	4.11	3.98	4.50	3.70
N(Se)	2.00	2.26	2.11	2.91	2.50	N/A
$\langle N \rangle$	2.50	2.70	2.56	3.19	3.00	

Table 7: Interatomic distances in Å for the pairs ij obtained by AXS/RMC in comparison with other experiments.

	r_{ij}, low conductivity phase			r_{ij}, high conductivity phase		
	AXS[63]	this work	Mo-K_α[57, 58]	this work	Mo-K_α[57, 58]	EXAFS[61]
x	0	15	30.7	50	50	56.5
at%Ag	0	4.2	9.7	20	20	24.5
correlation	first neighbour distance r_{ij} / Å					
Ag-Ag		2.95	3.05	2.95	3.05	2.8-2.9
Ag-Ge						
Ag-Se		2.6	2.67	2.6	2.67	2.6
Ge-Se	2.35	2.35	2.37	2.35	2.39	2.34
Se-Se	2.2	2.35	2.37	2.45	2.39	2.5
	second neighbour distance r_{ij} / Å					
$Ag\text{-}Ag_{2nd}$		3.9		3.9		3.6
$Ag\text{-}Ge_{2nd}$		3.55		3.65		
$Ag\text{-}Se_{2nd}$		-		3.9		
$Ge\text{-}Ge_{2nd}$	3.4	3.45		3.85		3.8
$Se\text{-}Se_{2nd}$	3.9	3.85	3.85	3.85	3.88	

4.2.3 Intermediate range order

The second neighbour Se-Se bond distance of about 3.85 Å is usually interpreted as the Se-Se distance inside the Ge-Se_4 tetrahedra [63, 64]. Analogously, the Se-Se distance at 2.35 Å can be regarded as the inter-tetrahedra connections, which exhibit a similar coordination number and distance in both compositions. The coordination number of the second neigbour Se-Se correlation decreases from 10.5 for Ag4 to 9.2 for Ag20, exhibiting the same trend as in [57]. The differences to the values in [57] may result from the difficulty to unambiguously define the borders of the second coordination sphere. The coordination number of the second coordination shell of the Ge-Ge correlation remains nearly constant, but the interatomic distance increases from 3.45 to 3.85 Å. The former distance agrees well with the value found for the corner-sharing configuration of $GeSe_4$ tetrahedra in Ge_ySe_{100-y} glasses of about 3.4 Å [58, 66]. In this respect, the coordination number of the second neighbour Ge-Ge correlation can be interpreted as a measure for the strength of the $GeSe_4$ tetrahedral network, indicating the strong connectivity in both the materials. The elongation of the Ge-Ge distance is accompanied by a shift of the maximum in the Ge-Se-Ge bond angle distribution from 90° to nearly 109°, as illustrated in fig. 30.

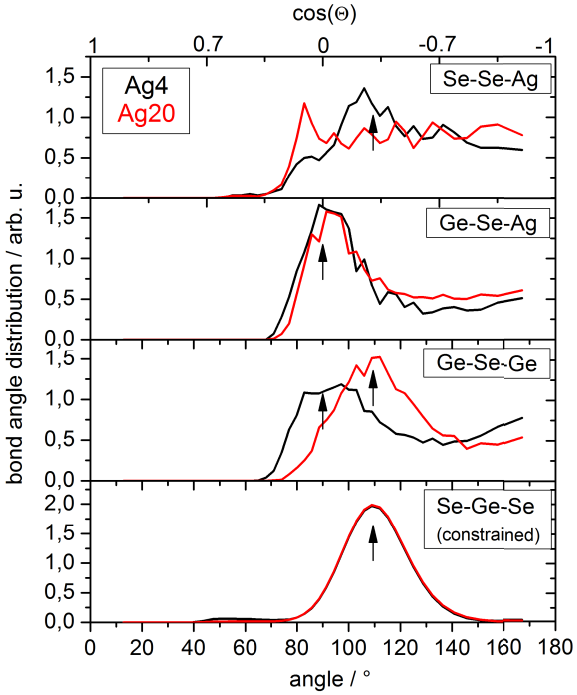

Figure 30: Bond angle distributions of Se-Ge-Se, Ge-Se-Ge, Ge-Se-Ag and Se-Se-Ag (from bottom to top) in Ag4 (black) and Ag20 (red). Arrows indicate angles of 109.5° and 90°, respectively. Note that the Se-Ge-Se angle was constrained during the RMC simulation.

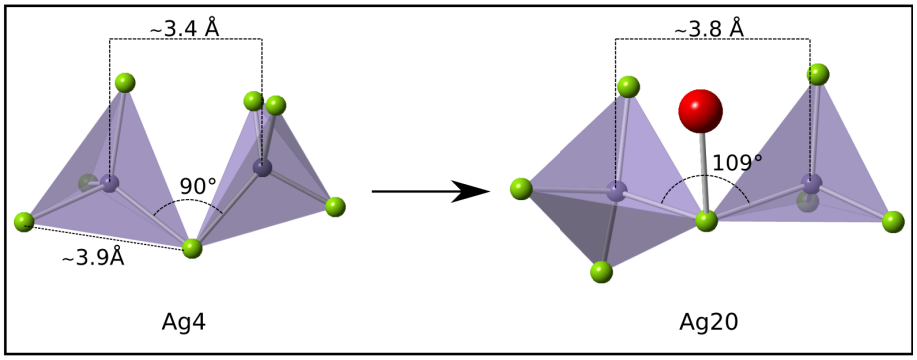

Figure 31: Schematic view of the expansion in the $GeSe_4$ network upon increase of Ag content x (red: Ag, green: Se, blue: Ge).

A 90° Ge-Se-Ge bond angle can be regarded as the result of bonding via the p-orbitals of Se, with a lone electron pair in the remaining p-orbital. This is the case in Ag4, possessing a total coordination number $N_{\mathrm{Se}} = 2.26$. For Ag20, however, N_{Se} rises to 2.91, mainly due to an increased number of Se-Ag bonds. The interaction of the Ag atom with the lone pair at Se thus causes the Ge-Se-Ge bond angle to increase. This effect is important for understanding the nature of the tetrahedral network and it is schematically depicted in fig. 31: Two corner-sharing Ge-Se_4 tetrahedra, which are the main structural building block, adopt an angle towards each other given by the Ge-Se-Ge bond angle. The intra-tetrahedra bonds are not affected by the compositional change from Ag4 to Ag20. Now, it is important to realize that the number of Ag-Se bonds is quite small in the former glass, but in the latter, nearly every Se atom is surrounded by one Ag atom (on average), cf. tab. 6. If a Se-Ag bond is formed, the Ge-Se-Ge angle rises from 90° to about 109°, causing the Ge-Ge distance to increase from about 3.4 Å to 3.8 Å in Ag20, while retaining nearly the same coordination number. The Ge-Se-Ag angle itself is about 90°, as seen in fig. 30.

In addition, it is found that the Ag-Se bonds in the first coordination shell are formed at the expense of the second coordination shell at 3.9 Å, which is clearly developed only in Ag4; this is reflected not only in the $g_{\mathrm{AgSe}}(r)$, but also in the Se-Se-Ag bond angle distribution in fig. 30, which shows a distinct peak around 105° only for Ag4. This correlation thereby illustrates the principal contribution to the loss of IRO in the Ag based correlations in Ag20.

The final structural aspect to be discussed is the Ag-Ag correlation. At first glance, the partial pair correlations $g_{\mathrm{AgAg}}(r)$ in both glasses are surprisingly similar, as seen in fig. 27. The first and second coordination shells increase proportionally to the Ag concentration in terms of the coordination number, and also the interatomic distances remain the same. However, there are major differences in the distribution of the Ag atoms over the simulation box, as suggested by the low-Q features of the partial $S_{\mathrm{AgAg}}(Q)$ functions shown above in fig. 26. Their real-space equivalents are illustrated as the Ag distributions over a wide range in fig. 32. It is found that regions of high concentrations of Ag atoms (shown in red) are clearly bordered by regions of low Ag concentration against a background of Se (green) and Ge (blue) in Ag20. In contrast, the Ag atoms in Ag4 are found to be statistically distributed among the other atoms. Thus, Ag20 tends to form cluster-like configurations of Ag atoms on a nanometer length scale.

A closer inspection can be achieved by a statistical analysis as shown in fig. 33, which displays the probability of finding an Ag ion with the indicated number of neighbouring Ag ions. The distributions are separately shown for the first, second and third coordination shells, respectively. It is found that on the next neighbour scale, the majority of Ag atoms do not form homopolar bonds in both glasses. Only 7% (in Ag4) and 23% (in Ag20) of the Ag atoms possess one neighbour of the same type. The number of two-fold coordinated atoms, which may act a a basis for chains of Ag atoms, is basically negligible in Ag4 (0.2%) and only 6.3% in Ag20. On the other hand, the distributions shown for the second coordination shell suggest the formation of a pronounced network of Ag atoms on the intermediate length level in Ag20. The insets in fig. 33 illustrate the Ag network on the level of the second neighbours. A similar finding was reported by Ohara and coworkers [60]. This intermediate network is characterized by bond angles of 60° and a broad distribution around 110°, as displayed in fig. 34, majorly differing from the bond angles observed on the next neighbour level, possessing a peak around 80°.

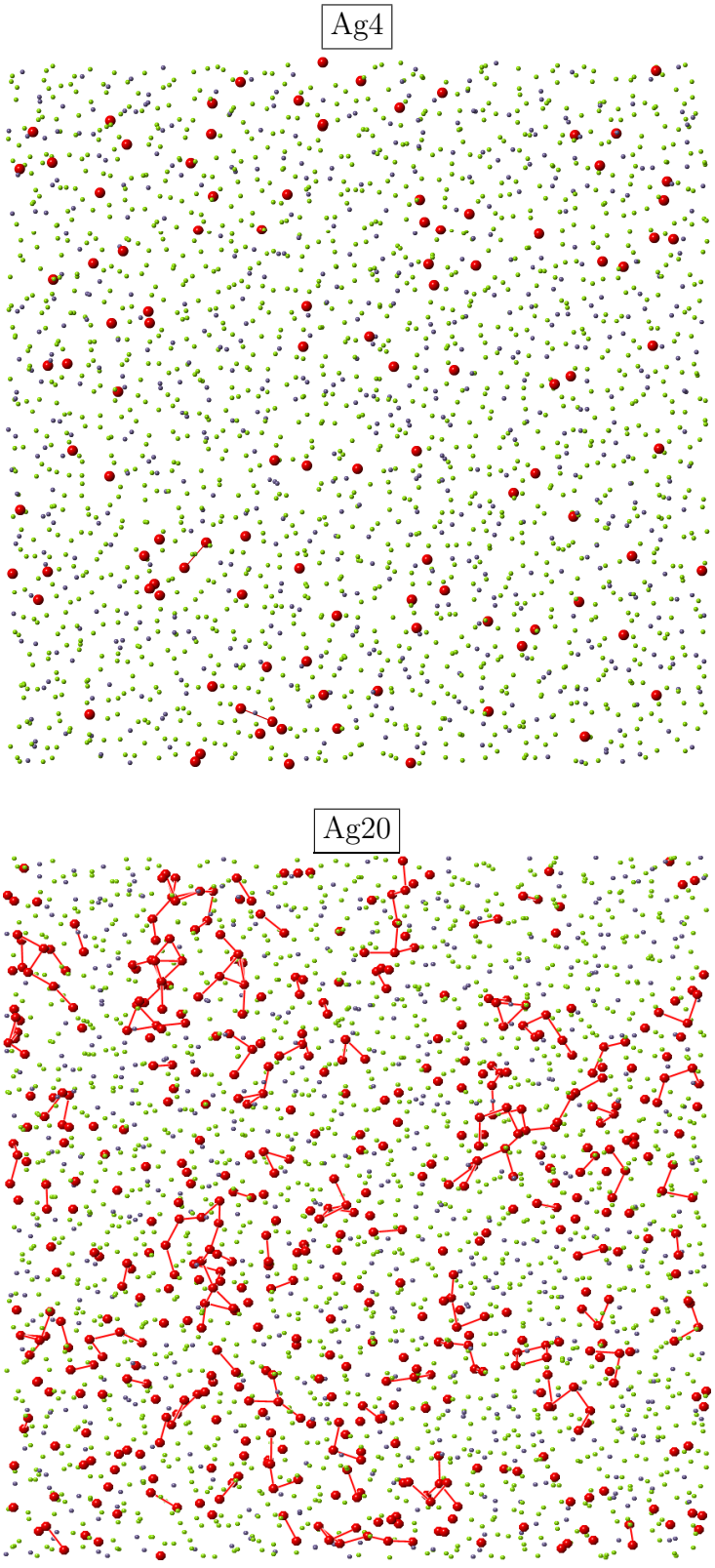

Figure 32: 64×64 Å^2 sections of the configuration of Ag4 (top) and Ag20 (bottom) obtained by RMC. The latter shows distinct regions with high or low density of Ag atoms, respectively (red: Ag, green: Se, blue: Ge).

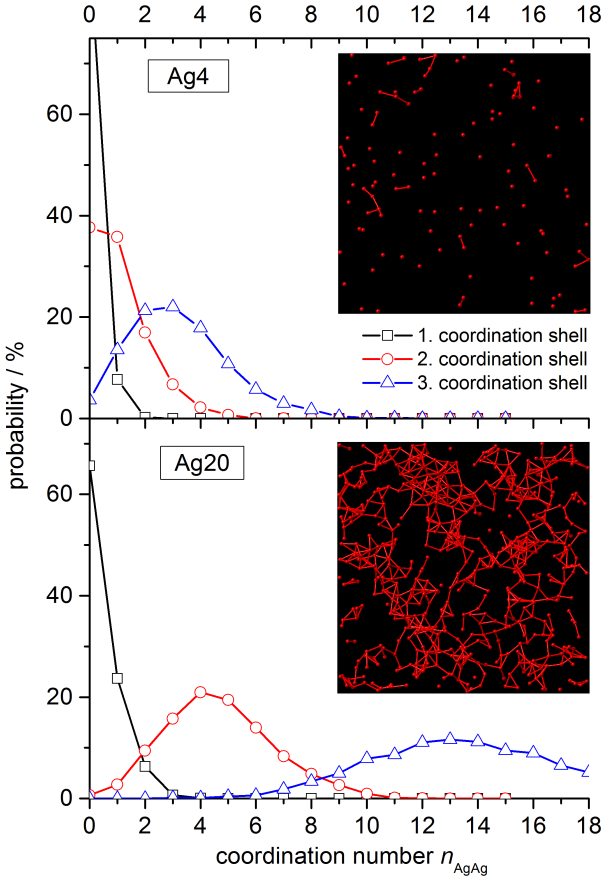

Figure 33: Probability of finding an Ag ion with the indicated number of neighbouring Ag ions in the respective coordination shells of Ag4 (top) and Ag20 (bottom). The insets illustrate the Ag distribution in a 64x64 $Å^2$ section on the level of the second coordination shell.

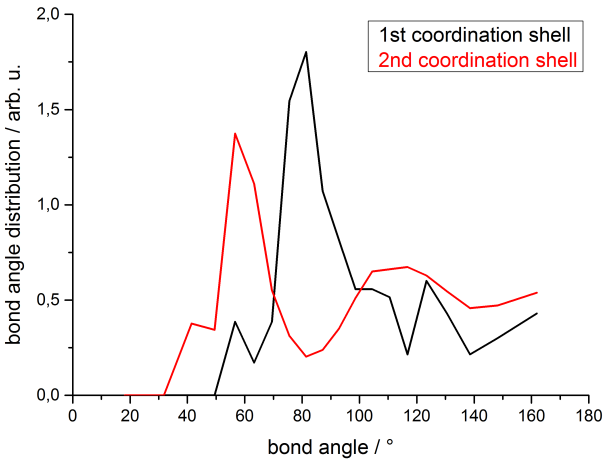

Figure 34: Bond angles of Ag-Ag-Ag chains on the level of the first and second coordination shell.

4.2.4 Extended range order

Oscillations in the partial distribution functions on length scales extending to 30 Å or more are found in both Ag-$GeSe_3$ glasses under consideration. The functions $\rho_{ij}(r)$ defined by eq. 2.25 in section 2.4 are illustrated for the individual correlations in fig. 35. The $\rho_{ij}(r)$'s are fitted with a damped sine function. It can readily be observed that the agreement to the $\rho_{ij}(r)$ in most correlations is good above a value of approximately 7 Å. Below this distance, the atomic arrangement is dominated by the correlation of next neighbours and the IRO. It is also observed that the oscillations in $\rho_{ij}(r)$ are more distinct, the sharper the extremum in $S(Q)$ is shaped. For example, the peak in $S_{\mathrm{GeGe}}(Q)$ is rather broad, causing a large contribution of different wave functions to the extended range order (ERO) in the pair correlation functions.

The observed oscillations possess a period of about 3.1 Å, corresponding to the position of the principal peak at $Q_2 \approx 2\text{Å}^{-1}$ in the partial structure factors with a period $p = 2\pi/Q_2$. This confirms the view of Salmon et al. [29], that the ERO represents a propagation of SRO and is connected to the main signal in the respective structure factor (see section 2.4). However, it has to be noted that the period of 3.1 Å that is found in basically all correlations does not directly relate to any single first neighbour distance.

As an interesting side note, the previous considerations enable us to interpret the meaning of the minima in the reciprocal space functions, which are observed e.g. at the Q_2 position in $S_{\mathrm{GeSe}}(Q)$, in contrast to the maxima found in the other correlations. That is, in the real space structure, they represent a phase shift in the oscillations of the corresponding pair distribution functions. As can be seen in fig. 35, the $\rho_{ij}(r)$ functions resulting from correlations with peaks at the Q_2 position can be fitted with sine functions that are in-phase; correlations with a minimum at this position are phase shifted by half a period of oscillation. The corresponding partial structure factors are exemplarily shown again in fig. 36 for the Se-Se and Ge-Se correlations.

This finding, however, is not surprising given the nature of the Fourier transformation, yet it is rarely discussed in publications concerning the structure of amorphous systems, as the main focus is usually limited to the short-range order of nearest neighbours. It is therefore useful to illustrate this effect using simple model functions, as shown in fig. 37. The two damped sine functions with a period of 3.1 Å on the left hand side (representing

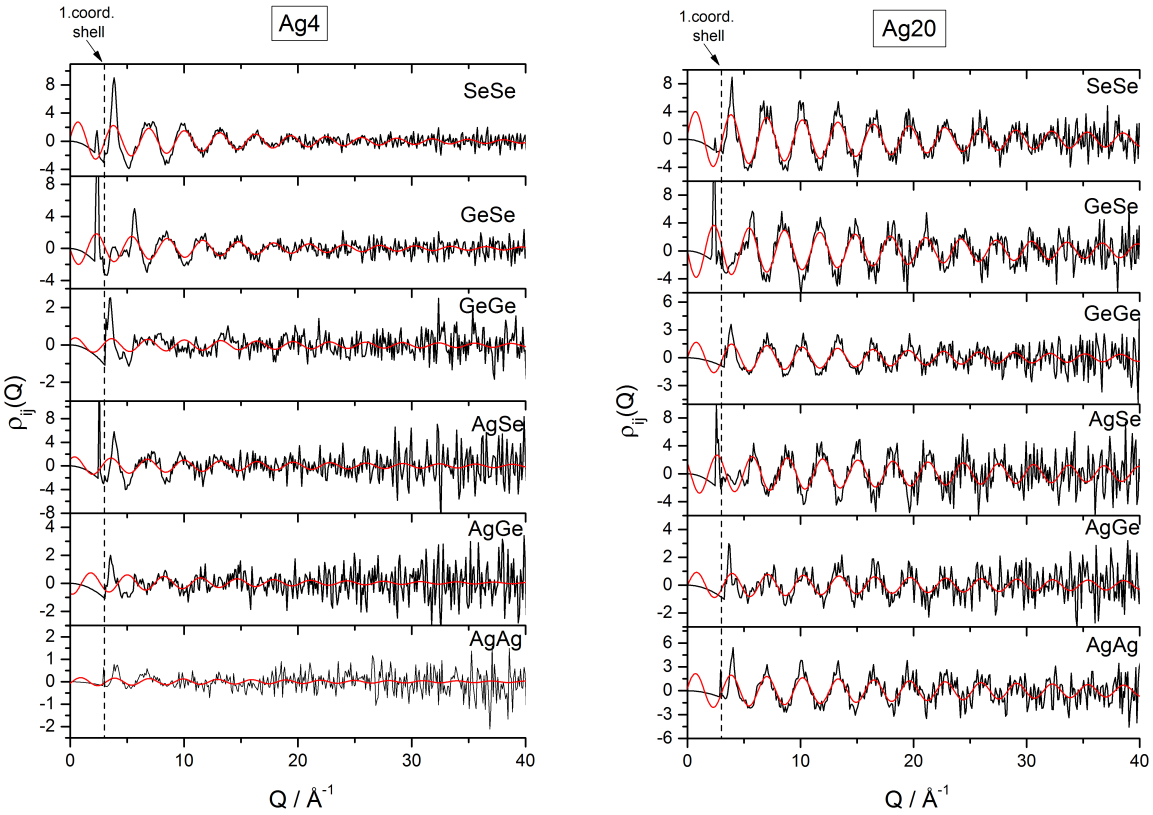

Figure 35: Extended range order for Ag4 (left) and Ag20 (right), as illustrated by the function $\rho_{ij}(Q)$. Data from RMC are coloured black and fits with a single damped sine function are red.

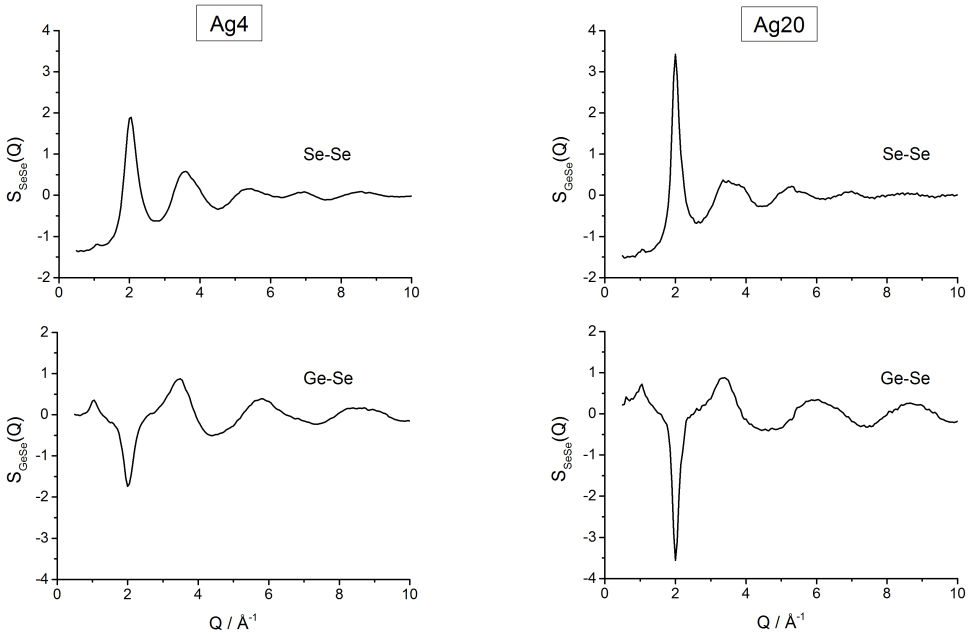

Figure 36: Sections of the partial structure factors from fig. 26 of the Se-Se (upper graphs) and Ge-Se correlations (lower graphs) for Ag4 (left) and Ag20 (right), emphasizing the oppositional amplitudes.

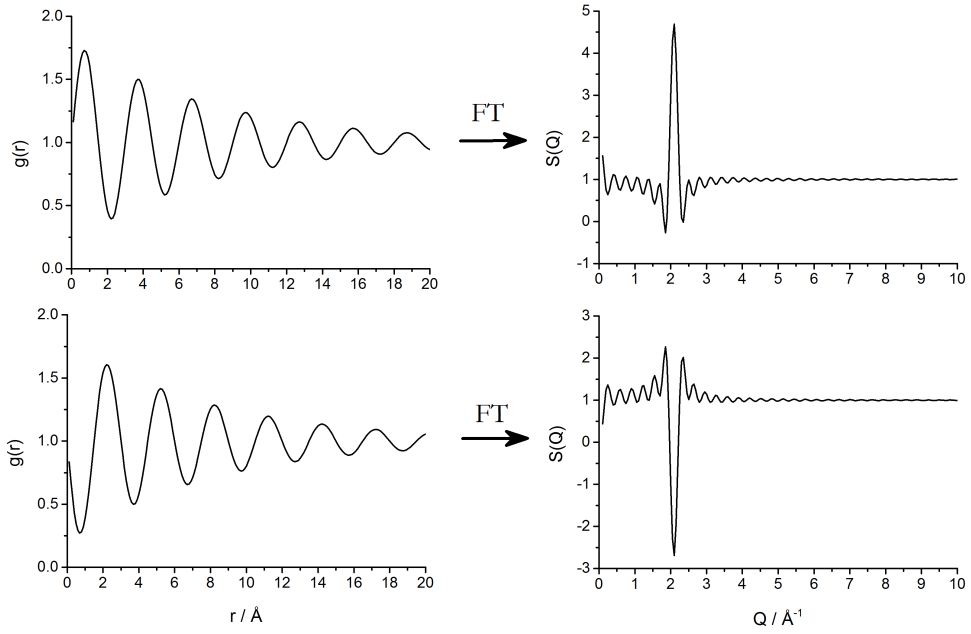

Figure 37: Illustration of the effect of a phase shift in $g(r)$ to the sign of the signal in $S(Q)$: Two damped sine functions, phase-shifted by half a period (left) and the corresponding results of a Fourier transformation (right).

two different ERO $g_{ij}(r)$'s) have a phase difference of exactly half a period, resulting in "mirrored" peaks near 2 Å^{-1} in the Fourier transformed "$S(Q)$" functions on the right hand side. The "Fourier ripples" caused by truncation errors in the real space functions are also unmistakably represented in fig. 37. In the actual experimental functions, SRO and IRO characteristics superimpose these structures and hence result in the typical shape of the structure factors and pair correlation functions.

4.3 Impact of the structure on the ion conduction mechanism

The data presented here permit the discussion of the structural changes enabling the superionic conductivity in Ag-$GeSe_3$ glasses. A substantial change in the short-range order is observed upon increasing the Ag content above the superionic conductivity threshold at $x = 0.33$. On this level, the superionic phase (Ag20) is characterized by high average coordination numbers around selenium and silver and by Ge-Se_4 tetrahedral motifs. On the next level of structural order, it is found that the network of corner-shared Ge-Se_4 tetrahedra widens compared to Ag4 due to the Ag-Se interaction, as indicated by the Ge-Se-Ge bond angle distribution and by the Ge-Ge distances, while the tetrahedra connection remains similarly strong, as indicated by the Ge-Ge second coordination numbers. The expanded network incorporates the higher number of Ag atoms, which form regions of high and low Ag concentrations. As a result, small cluster-like configurations are formed on the nanometer length scale, which act as percolation pathways for the Ag atoms. These clusters lead to the loss of intermediate range order of the Ag atoms as represented by the decrease of the Ag-related FSDPs.

However, from the present data it cannot yet be concluded whether the jump in ionic conductivity is associated with a comparably sharp change in the glass structure, or whether the structural changes are a continuous function of x. Since it is reported that even within one phase (i.e. the fast ionic conducting phase), short-range order parameters can change significantly as a function of the Ag content (cf. [58]), further investigations near the superionic conductivity threshold are necessary in order to study the nature of the jump in ionic conductivity.

Finally, it has to be noted that the ternary $Ag_x(Ge_ySe_{1-y})_{1-x}$ glasses have been reported to be macroscopically phase separated on the entire concentration range of Ag under investigation. Such a structural characteristic would naturally have a tremendous influence on the interpretation of the diffraction data, which inherently can only provide information on the spatially averaged structure of the material and comprise no information about a macroscopic phase separation. It should be taken into account, however, that this finding is based on glass transition temperature measurements (DSC) [67], scanning electron microscopy (SEM) [68] and electric force microscopy (EFM) [69, 70]. The investigations agree in so far as they report a transition from an Ag-rich phase immersed

in a Ge-Se phase for low Ag concentrations to a structure with Ag-poor zones immersed in an Ag-rich network for high Ag concentrations. The size of the respective regions, however, appears to be a point of discussion: For the insulating phase (< 10 at% Ag), the size of the Ag-rich inclusions have been reported to be 1-3 μm [67], 1 μm [69] or 110 nm [68]. The Ag-poor inclusions observed for the phase with 20 at% Ag are reported to be 250-500 nm [69] or 700 nm [68]. The authors of the latter article also report that the composition with 25 at% Ag is nearly homogeneous.

It may be objected that inhomogeneities probed by electron microscopy naturally describe only the surface of the samples, which may differ considerably from the bulk structure. The DSC measurements, on the other hand, indicate a phase separation in the bulk material, but can provide no details on the size of the separated volumes. Correspondingly, an onset of the separation of Ag-rich and Ag-poor phases is observed in the present AXS study, albeit on the nanometer range. Further insight into such structural details can be obtained by small angle scattering data, which should be gathered in a subsequent series of experiments.

5 GeTe-Sb_2Te_3 glasses

Ternary Ge-Sb-Te alloys have found a widespread application in optical data storage devices such as the digital versatile disk (DVD) or blu-ray disk (BD). New fields of application include the electronical storage of data, e.g. in Flash memory or PCRAM (phase change random access memory) devices. Their functionality as rewriteable storage media is based on the ability to switch reversibly back and forth between a meta-stable crystalline and an amorphous phase, thereby substantially changing their optical reflectivity and electrical resistivity. Furthermore, transition times are in the range of only some tens of nanoseconds, allowing fast writing and erasing cycles.

Due to the optimal properties for phase-change applications, the pseudo-binary line $(GeTe)_{1-x}(Sb_2Te_3)_x$ is of particular interest within the ternary system. A first extensive study of this line has been reported by Yamada and coworkers already in 1991 [71]. They investigated the phase transitions occurring in these compounds as a function of the Sb_2Te_3 content x, and report phase transition temperatures for the amorphous to meta-stable crystalline phase ranging between 100-150°C, and for the meta-stable to the stable crystalline phase between 150°C and 300°C. These values are based on differential scanning calorimetry (DSC) experiments. Furthermore they present measurements of the reflectivity of the samples to demonstrate their potential for optical memory applications and show the necessary laser pulse duration required for crystallization. These measurements relate to the crystallization speed which decreases significantly from GeTe (100 ns) to Sb_2Te_3 (30 ns). Note that even shorter transition times have been reported subsequently, but the same trend is consistently observed. For example, Loke et al. report a special setup which reduces the crystallization time to the picosecond domain [72].

These fast transition times and the high reversibility of the phase change process result in conflicting material characterizations, which indicate that the associated phase transitions are not yet fully understood: for long-term stability of the optically written information, the material should be a good glass former and therefore possess a high reduced glass transition temperature. In that case, the activation barrier for the crystalline reorganization would be high, and the recrystallization would thus be slowed significantly. This way, the long-term stability of the written information would be ensured, but a rewrite process would be slow or impossible. However, in order to be able to compete with

conventional magnetic data storage media, the rewrite process must be appropriately fast so that the material can easily be converted back to the polycrystalline phase. This, in turn, requires the characteristics of a bad glass former, and it is currently unclear how both properties are combined at the same time in the PCMs. In addition, the phase transitions have to be fully reversible over many cycles (more than 10^9 write/rewrite operations), and the short-range structural changes associated with the phase change have to be sufficiently large to provide the desired contrast of the electrical and optical properties (a feature that is usually referred to as the optical or electrical contrast).

GeSbTe compounds exhibit a remarkable dependence of these properties as a function of the composition along the *tie*-line between GeTe and Sb_2Te_3 in the ternary phase diagram, which is schematically displayed in fig. 38. Compositions along the pseudo-binary line investigated in this study are marked in red. The origin of this dependence is not yet understood, although these materials have been used in industrial mass production for a long time. One reason for this lack of information is that the structural properties of the amorphous phases are still not well comprehended.

The atomic structure of the crystalline phases of the system GeTe-Sb_2Te_3, on the other hand, is relatively well investigated, and has been solved by powder x-ray diffraction (XRD), extended x-ray absorption fine structure spectroscopy (EXAFS) and theoretical methods [73–77]. The stable crystals adopt a hexagonal symmetry. However, it is not the stable crystalline phase that participates in the phase change process, but a meta-stable *fcc*-type phase that is formed during the fast heating and cooling cycles of the thin films. This meta-stable phase has a rhombohedral symmetry (space group R3m), and can be illustrated by two interpenetrating distorted rocksalt structures, with Te atoms fully occupying the sites on one *fcc*-sublattice and with Ge, Sb, and a distinct number of vacancies forming another *fcc*-sublattice [76, 77]. Convincing evidence for the pronounced distortions of these *fcc*-lattices in GeTe and $Ge_2Sb_2Te_5$ was found in XAFS experiments by Kolobov et al. [74, 75], who discovered that the six Ge-Te bonds originating from an octahedrally coordinated Ge atom separate into three shorter and three longer bonds.

The major factor contributing to the difficulty to gain insight into the amorphous structure is certainly the fact that the industrially employed GST's are three-component systems - and as mentioned in the theoretical introduction in sec. 2.1, it is extremely difficult to reliably determine a complete dataset needed to unambiguously characterize

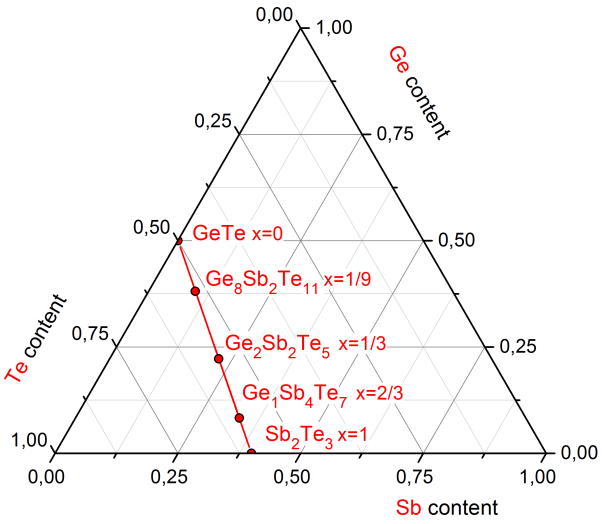

Figure 38: Location of the pseudo-binary line GeTe-Sb_2Te_3 in the ternary phase diagram Ge-Te-Sb. Compositions of interest in this study are marked as red circles.

all structural correlations. Partial information about the atomic ordering in these systems has so far only been obtained from x-ray absorption fine structure investigations. However, this method allows to access only the immediate vicinity around the examined element. Partial correlation functions determined from the combination of RMC and EXAFS data therefore only give an incomplete view of the real structural situation. This also hampers the accuracy of coordination numbers obtained exclusively from EXAFS-investigations in disordered systems [78]. A different approach to investigate the amorphous structure are Molecular Dynamics computer simulations. Such investigations have been conducted for several GeSbTe compositions, but the small system size (typically around 200-400 atoms, resulting in cubic simulation boxes with a length of about 20 Å), set by the need for reasonable computing times, also results in a poor description of correlations in intermediate or extended length scales. Hence, a different approach for the investigation of these compounds is needed, for which the combination of AXS with RMC modelling appears to be ideally suited.

The most exhaustively investigated compound on the pseudo-binary line is $Ge_2Sb_2Te_5$ (also referred to as GST-2,2,5) with $x = 1/3$. This composition also is the first material used in large-scale industrial production for the DVD-RW. It offers less optical contrast than the more GeTe-rich composition, e.g. GST-8,2,11 which is used for Blu-ray disks - thus indirectly limiting the amount of data that can be stored on a given surface - but it

possesses a faster crystallization speed, permitting a good writing/erasing speed. Using the GST-2,2,5 composition as a model system, various (partly conflicting) models aiming to explain the fast phase change process have been proposed. These models were based on experimental techniques like total scattering experiments, EXAFS and neutron diffraction [75, 78–82] and on theoretical methods employing Density Functional Molecular Dynamics calculations [83–87]. An intriguing model in this respect is the "umbrella-flip mechanism" proposed by Kolobov [75]. This model explains the fast crystallization/amorphization speed with the related atomic configurations, which are supposed to change from an octahedral to a tetrahedral environment by an "umbrella-flip"-like motion. This model has been refined by Hosokawa and coworkers [88] with respect to the description of the large number of homopolar bond chains observed in the glass and with respect to an explanation of the origin of the bond angle distribution around the germanium atoms. Other works focus on structural characteristics on the intermediate-range level by investigating the connectivity of the topological network formed by covalent bonds in the amorphous phase. This approach is known as "ring statistics" analysis and searches for closed paths of covalent bonds that originate from and leading back to the same atom. Thereby, the fast phase-change process is explained with the unusual ring statistics observed in these glasses, which exhibit a large similarity between the crystalline and the amorphous phase [82].

However, the AXS/RMC results presented in this chapter call for a re-evaluation of the current state of research. For a comparison with the proposed models, the following sections give a discussion of the implications of the structure probed by AXS for the short- as well as for the intermediate range order.

5.1 Raw data and applied corrections

The anomalous scattering experiments on the GST glasses have been performed both at the ESRF and at SPring-8, including four different compositions along the pseudo-binary line. Germanium telluride (GeTe, $x = 0$) was chosen as a starting point for the investigations. As GeTe constitutes a pure binary compound, it should in principle be possible to measure a complete set of experimental data in $2 \cdot (2 + 1)/2 = 3$ scattering experiments (compare details given in section 2.1). The composition with $x = 1/9$, i.e.

Table 8: Overview about the AXS experiments conducted for the GeSbTe glasses. Near- and far edges were defined -20 and -200 eV for the Ge edge, and -30 and -300 eV for the Sb and Te edge, respectively.

Composition	Edge (energy)	Experiment	Prim. int. / data point
GeTe	Ge (11.103 keV)	HD-603	$2.0{\cdot}10^6$ cts
(x=0)	Te (31.810 keV)	2014A1624	$5.0{\cdot}10^5$ cts
$Ge_8Sb_2Te_{11}$	Ge (11.103 keV)	HD-603	$2.0{\cdot}10^6$ cts
($x = \frac{1}{9}$)	Sb (30.756 keV)	2014A1624	$5.0{\cdot}10^5$ cts
	Te (31.810 keV)	2014A1624	$5.0{\cdot}10^5$ cts
$Ge_1Sb_4Te_7$	Sb (30.756 keV)	2014B1733	$6.0{\cdot}10^5$ cts
($x = \frac{2}{3}$)	Te (31.810 keV)	2014B1733	$5.0{\cdot}10^5$ cts

GST-8,2,11, was chosen for its established technical importance as data storage material on the one hand, and to study the structural changes in the GeSbTe upon the addition of a small amount of antimony on the other hand. Furthermore, it is situated between GeTe and the extensively investigated GST-2,2,5, so that the trends in structural changes upon further addition of antimony may be examined. For GST-2,2,5 ($x = 1/3$), experimental data from [88] will be included in a new RMC modelling procedure to obtain a better comparability. Finally, in order to understand the decreasing crystallization times in the Sb_2Te_3-rich region, the composition GST-1,4,7 ($x = 2/3$) was considered. Due to a lack of available experimental time at the synchrotron facilities, however, only the Sb and Te edge were measured for this compound. The experimental details are summarized in table 8.

The experiments were performed in transmission geometry (see fig. 10) using a specially designed brass container cell described in section 3.1.3. The experimental raw data are illustrated in figure 39 at each absorption edge. Data corrections, i.e. absorption / inelastic scattering corrections and normalization, are carried out as described in section 3.2.2. Corrections due to the analyzer crystal as described in section 3.2.4 are found to vary to some extent between the individual scans, especially for the data gathered at SPring-8 (i.e. experiments denoted 2014A1624 and 2014B1733 in tab. 8), thus greatly complicating the data correction process. However, an approach slightly adjusted to the experimental conditions yields satisfactory results, and will be described in the following subsection.

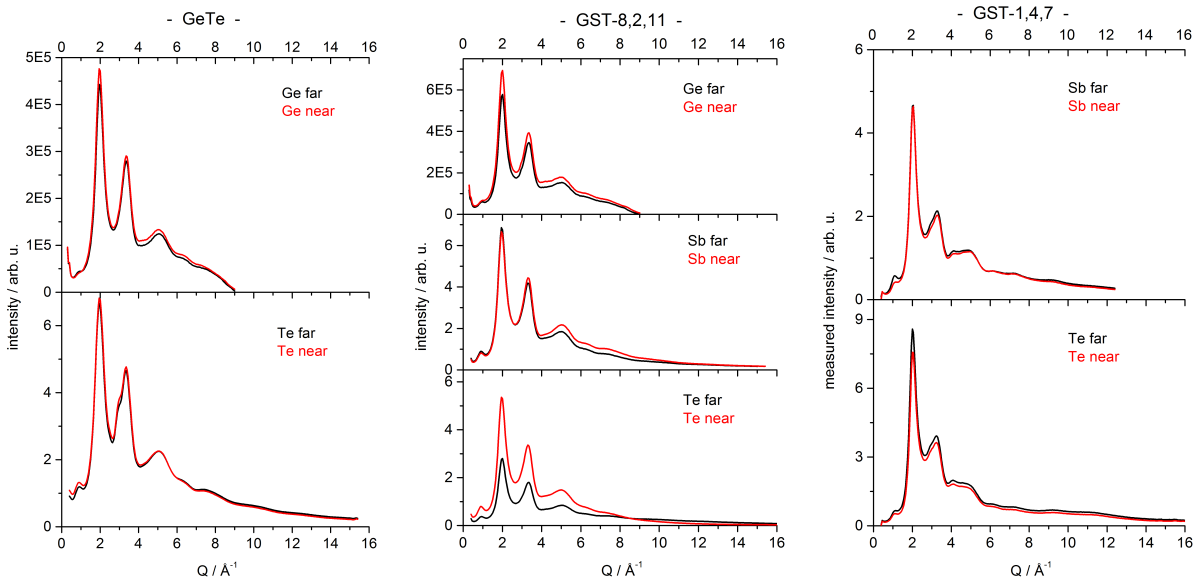

Figure 39: Raw data $I(Q)$ measured for the GeSbTe glasses at the Ge, Sb and Te K edges. Note that the different orders of magnitude of the intensity scale results from the different beamlines.

5.1.1 Analyzer specific corrections

For the scattering data near the Sb edge of GST-8,2,11, which have been measured at BL13XU/SPring-8, a different approach to correct the experimental data than described in section 3.2.4 was tested. The significance of this correction may again be illustrated by inspecting the structure factors calculated from the raw data (after correcting for absorption and inelastic contributions), displayed in fig. 40. Apparently, an important step of the data correction scheme is missing, as the graphs of the near- and far-edge are much more different than expected and neither one oscillates steadily around unity for high Q-values. The reasons for this characteristic are outlined in section 3.2.4.

A possible correction to this phenomenon would be to ensure the correct position of the analyzer and the detector at any measured angle, e.g. by a short scan of the analyzer angle at every step. Such a procedure, however, is currently unfeasible using the experimental setup at hand. Nevertheless, with respect to the time restrictions of a typical synchrotron experiment, it is possible to fragment each measurement into smaller parts, e.g. Q regions of 0.5 Å^{-1}. Then, an analyzer scan is conducted at the end of each segment, and the analyzer crystal is positioned at the center of the elastic signal. We may assume that the movement of the beam on the analyzer crystal and thus a possible

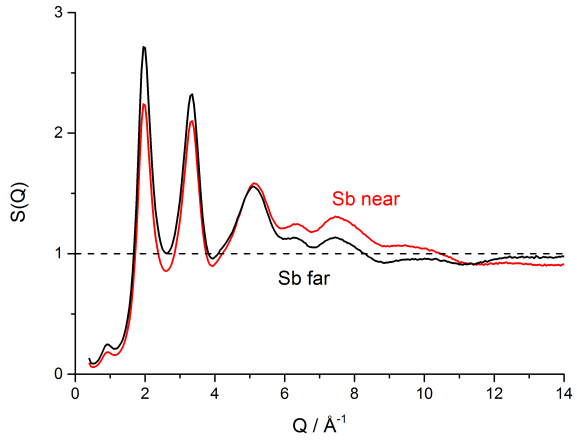

Figure 40: Uncorrected structure factors $S(Q)$ at the Sb absorption edge of GST-8,2,11. The line at $S(Q) = 1$ is a guide for the eye.

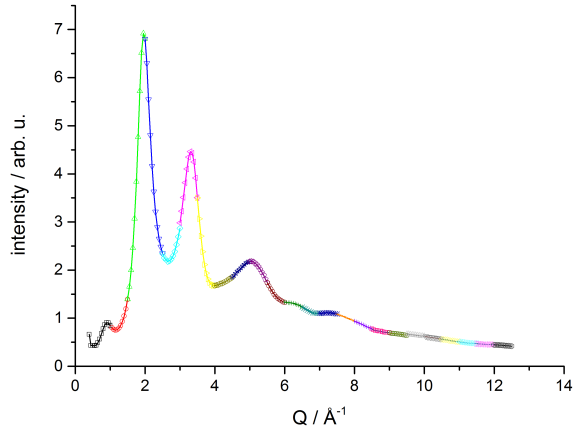

Figure 41: Segmented measurement at the Sb near egde of GST-8,2,11. Each color represents one of 24 individual scans of a 0.5 Å^{-1} segment. The position of the analyzer crystal was optimized after each scan.

intensity loss is negligible in each segment. In the Q-range of interest, 24 individual scans are obtained that can be combined to one total graph, as shown in figure 41.

Unfortunately, such a combination of scans results in sharp features in the $\Delta_k S(Q)$ at the borders of each scan. In order to compensate for this effect, the intensity ratio between the original measurements and the "optimized" scans is calculated, as illustrated in fig. 42. This ratio is then used to correct the data measured in the continuous scan. Thus, in turn, this kind of correction is very similar to the analyzer correction presented in section 3.2.4. The structure factor calculated from such a segmented measurement is shown in fig. 43; the improvement compared to fig. 40 is obvious.

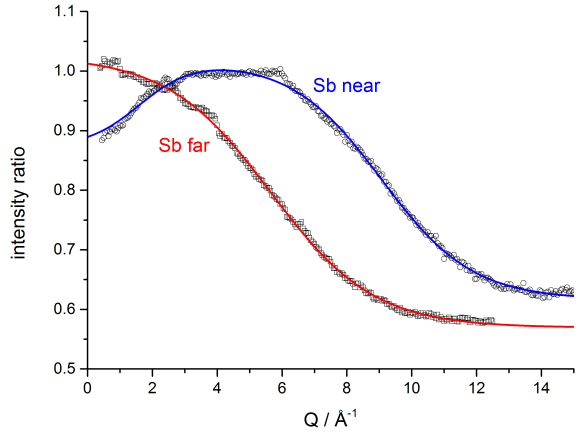

Figure 42: Ratio of the uncorrected intensity to the segmented scans at the Sb edges of GST-8,2,11. Solid lines represent fits of sigmoidal functions.

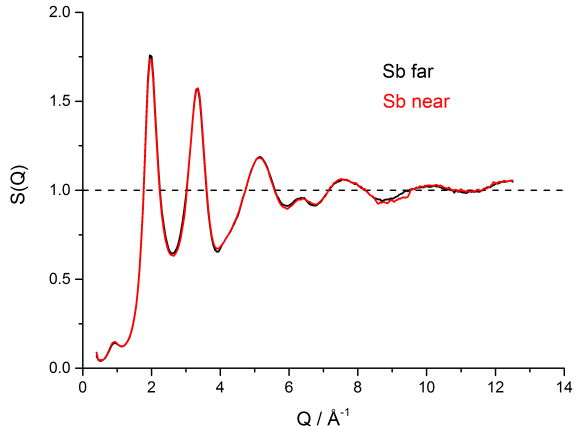

Figure 43: Structure factors $S_{\mathrm{Sb}}(Q)$ of GST-8,2,11 after the correction shown in fig. 41 and 42. The line at $S(Q) = 1$ is a guide for the eye.

5.1.2 Structure from total measurements

The total structure factors and the corresponding total pair distributions functions obtained for the four different GST compositions are displayed in figure 44. It is instructive to investigate the trends observable in these functions, as there are yet no assumptions made concerning structural properties. Such assumptions will necessarily be introduced by a subsequent RMC modelling procedure, as outlined in the following section. As a consequence, the investigation of the total $S(Q)$'s and $g(r)$'s will emphasize the limitations of a structural description with respect to total scattering functions only.

The total structure factors in fig. 44 represent the measurements at each compositions' Te-far edge. The most prominent signals are labeled Q_1 - Q_4, the index counting the relative sequence of the signals. The Q_1 peak at around 1 Å^{-1} is a so-called first sharp diffraction peak (FSDP) and is comparably small in each structure factor, which indicates that the peak is correlated to an element with a minor atomic fraction or to a minor correlation. The principal peak at Q_2=2 Å^{-1} remains constant in its position and only exhibits a small variation in intensity as a function of Sb_2Te_3 content x. The third peak at Q_3, on the other hand, decreases monotonically as a function of x, possessing a similar intensity as the Q_2 peak in pure GeTe ($x = 0$), i.e. around $S(Q) = 1.9$, and decreasing to 1.3 in GST-1,4,7 (see fig. 44). It should be noted that the shoulder visible on the low-Q side of the Q_3 peak vanishes upon addition of Sb to GeTe; it appears again, however, for higher concentrations of Sb_2Te_3, manifested as an asymmetry of the Q_3 peak. The last prominent signal seen in all compositions is the Q_4 peak. The position of this peak decreases from around 5.25 Å^{-1} in GeTe to 5.0 Å^{-1} in GST-1,4,7.

The pair correlations functions in fig. 44 exhibit similar forms, but some distinct trends can be observed. The peaks are labeled r_1, r_2 and r_3, corresponding to the first, second and third coordination shell. With respect to the elemental fractions, the major contributions to the peak at r_1 will be Ge-Te correlations for low values of x, and Sb-Te correlations for higher Sb_2Te_3 fractions. Due to the different atomic diameters of Ge and Sb, the position of the peak should thus increase with x, and indeed it is found that the signal maximum shifts monotonically from 2.6 Å in GeTe to 2.85 Å in GST-1,4,7. These distances are in very good agreement with the interatomic separation length reported for Ge-Te / Ge-Ge and Sb-Te, respectively [88–90]. On the other hand, the r_1 peak is becoming increasingly

asymmetric as a function of x, indicating the presence of Ge-correlated distances near 2.5 Å, which are not completely resolved from the Sb-Sb, Sb-Te and TeTe bonds near 2.85 Å in the total $g(r)$ function. The peak at r_2 near 4.1 Å shifts to higher r as well, but not as much as the r_1 peak. It is, however, interesting to observe that this signal also becomes increasingly asymmetric towards the low-r side. For GST-1,4,7, a distinct peak at 3.7 Å is nearly resolved. The third coordination sphere is situated at around $r_3 = 6.2$ Å, and exhibits only a small signal in the $g(r)$ functions. Nonetheless, such a distinct third coordination sphere is quite noteworthy and will be discussed later within the scope of the RMC simulation in more detail. It is interesting to observe that this sphere is predicted by AIMD simulations as well.

Total coordination numbers have been calculated from the integrals over the r_1 peaks by eq. 2.8 and are also indicated in fig. 44. The clearly developed minimum between the r_1 and r_2 peak was chosen as the upper limit for the integration. The total average coordination numbers $\langle N \rangle$ range closely around 3, with $\langle N \rangle = 3.1$ for GeTe, $\langle N \rangle = 2.9$ for GST-8,2,11, $\langle N \rangle = 3.1$ for GST-2,2,5 and $\langle N \rangle = 3.0$ for GST-1,4,7. Note that the integrated intervals for the calculation of the coordination numbers are not the same due to the different positions of the first $g(r)$ minima.

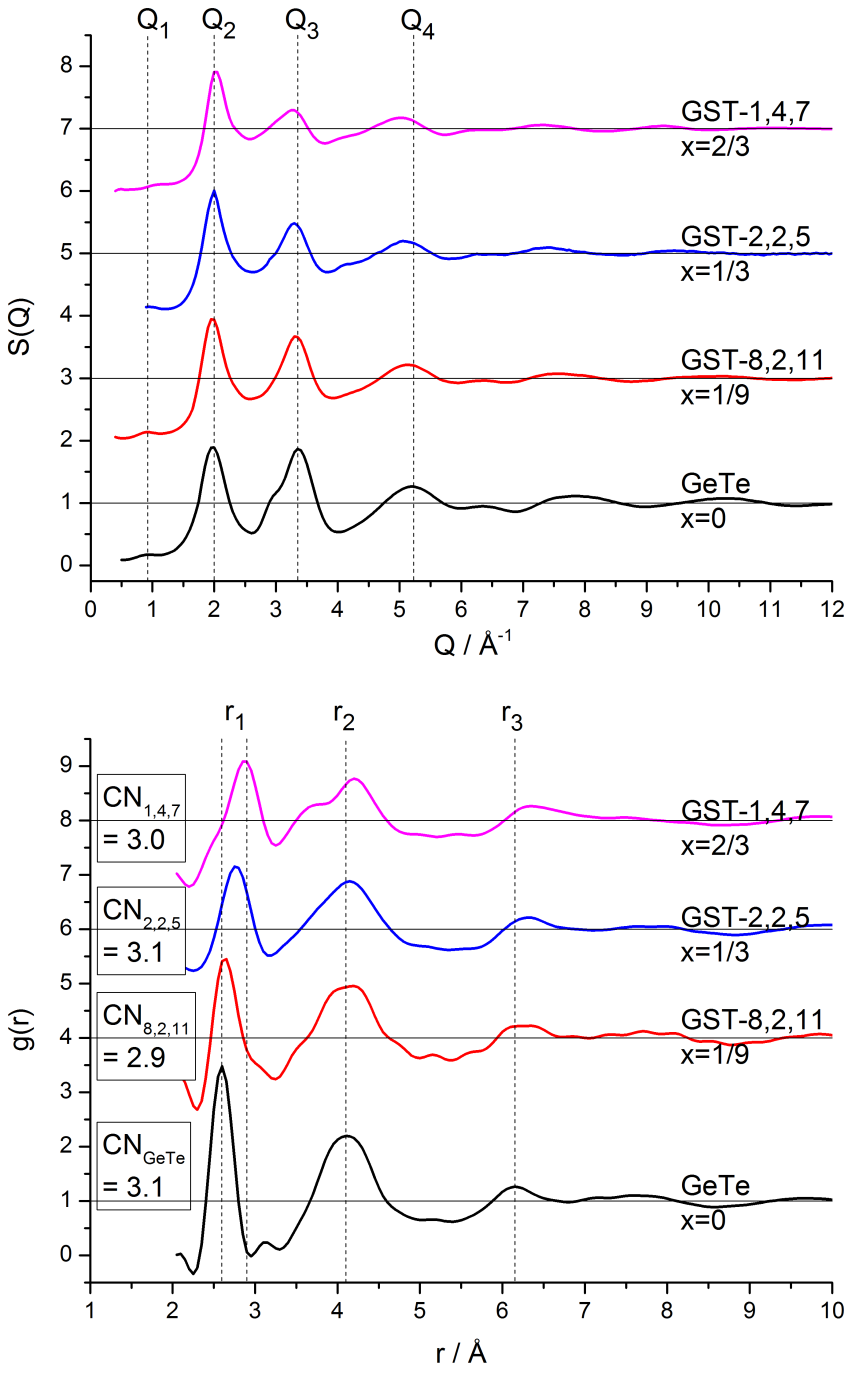

Figure 44: Total structure factors for each composition (top) and the corresponding total pair distribution functions (bottom). Datasets are shifted upwards for clarity, solid lines indicate unity for each graph, and dashed lines indicate positions of prominent peaks as a guide for the eye.

5.2 Reverse Monte Carlo Simulations on GeSbTe glasses

Input configurations with proper stoichiometry were chosen for each composition, with an initial random distribution of the atoms in a box corresponding to the number densities

- $\rho_N(\mathrm{GeTe}) = 0.0337$ atoms/Å^3
- $\rho_N(\mathrm{GST}-8,2,11) = 0.03133$ atoms/Å^3
- $\rho_N(\mathrm{GST}-2,2,5) = 0.0315$ atoms/Å^3
- $\rho_N(\mathrm{GST}-1,4,7) = 0.0279$ atoms/Å^3

Cut-off distances for the individual correlations Ge-Ge, Ge-Sb, Ge-Te, Sb-Sb, Sb-Te and Te-Te have been set to 2.4, 2.5, 2.4, 2.7, 2.5 and 2.8 Å, respectively. These distances have been chosen near the values for the respective sums of the covalent radii as outlined in [90], and adjusted to fit the first coordination shells adequately. Note that by this choice, no specific correlation is excluded in the first coordination shell. A typical starting configuration is shown in fig. 45 for GST-8,2,11, which consists of 10,000 atoms with random distribution in a cubic box. Only the cut-off distance constraint is applied. Characteristic features of these configurations are the atomic agglomerations near the cut-off distances and a fast convergence towards unity. Also visible is the different statistical quality of the graphs due to the different number of atoms for each element in the simulation box; in this case, Sb-related curves are much noisier, since the Sb concentration is only 9.5 at%. For the simulations on GST-1,4,7, a strong coordination number constraint on the germanium atoms was introduced in order to ensure a basic four-fold coordination. This constraint is necessitated by the incomplete set of structure factors for this compound. As will be outlined in the following, this type of coordination is also found in the other GST compositions.

The experimental structure factors for all GST compositions are illustrated in fig. 46 along with the results of the RMC fits. To give an impression on the relative information content of the partial correlations contained therein, the weighting factors are listed in table 9 for the maximum in $S(Q)$ at $Q = 2$ Å^{-1}. Qualitatively, the $\Delta_{\mathrm{Sb}}S(Q)$'s and $\Delta_{\mathrm{Te}}S(Q)$'s resemble the total $S(Q)$'s, though they exhibit larger oscillations and a FSDP around 1 Å^{-1} is seen in $\Delta_{\mathrm{Sb}}S(Q)$ of GST-1,4,7. On the other hand, the $\Delta_{\mathrm{Ge}}S(Q)$'s differ

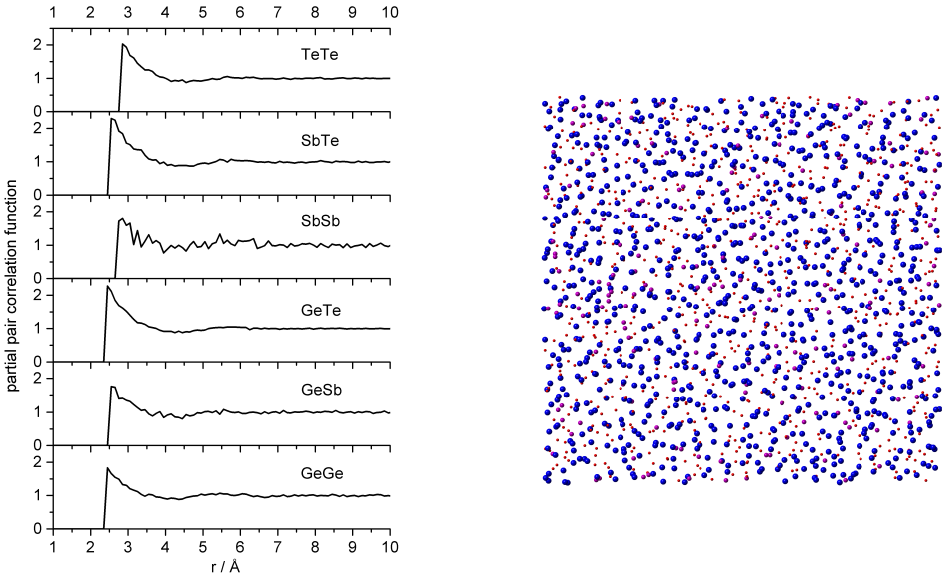

Figure 45: A typical starting configuration of 10,000 atoms with a random distribution in the simulation box, for GST-8,2,11. Only a constraint of nearest-neighbour cut-off distances has been applied. Left: Partial pair correlation function, right: 3D model of a 60x60x15 Å^3 section, Ge atoms are coloured red, Sb: violet, Te: blue.

majorly; they show smaller oscillations in general and exhibit the Q_3 peak as the most intense signal, whereas the Q_2 peak decreases in intensity with rising x. Furthermore, a first sharp diffraction peak around 0.9 Å^{-1} is observed in all compositions.

Table 9: Weighting factors W_{ij} for each dataset, exemplary at Q=2.0 Å^{-1} near the first peak position in $S(Q)$, for the GST glasses.

Composition	Dataset	GeGe	GeSb	GeTe	SbSb	SbTe	TeTe
GeTe	$S(Q)$	0.164		0.482			0.354
	$\Delta_{\mathrm{Ge}}S(Q)$	0.334		0.661			0.005
	$\Delta_{\mathrm{Te}}S(Q)$	0.001		0.411			0.588
GST-8,2,11	$S(Q)$	0.087	0.065	0.351	0.012	0.131	0.354
	$\Delta_{\mathrm{Ge}}S(Q)$	0.235	0.115	0.641	0.000	0.003	0.007
	$\Delta_{\mathrm{Sb}}S(Q)$	0.001	0.199	0.093	0.070	0.448	0.189
	$\Delta_{\mathrm{Te}}S(Q)$	0.000	-0.007	0.306	-0.002	0.101	0.601
GST-2,2,5	$S(Q)$	0.022	0.072	0.183	0.058	0.293	0.372
	$\Delta_{\mathrm{Ge}}S(Q)$	0.124	0.240	0.610	0.002	0.011	0.013
	$\Delta_{\mathrm{Sb}}S(Q)$	0.000	0.138	0.024	0.194	0.555	0.088
	$\Delta_{\mathrm{Te}}S(Q)$	0.000	-0.002	0.168	-0.003	0.243	0.595
GST-1,4,7	$S(Q)$	0.003	0.040	0.069	0.120	0.412	0.355
	$\Delta_{\mathrm{Sb}}S(Q)$	0.000	0.051	0.008	0.285	0.579	0.078
	$\Delta_{\mathrm{Te}}S(Q)$	0.000	-0.004	0.063	-0.025	0.334	0.632

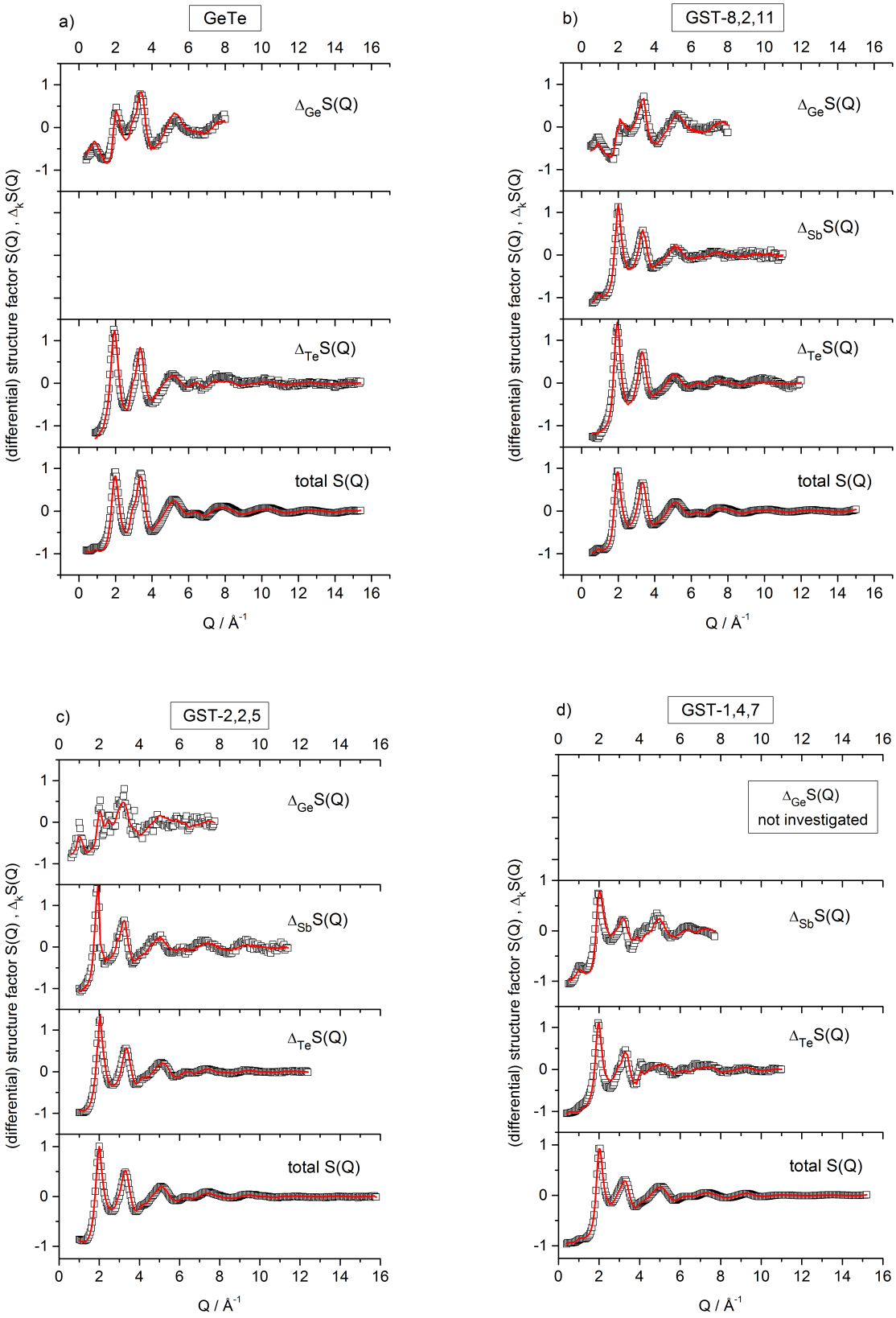

Figure 46: Experimentally determined total structure factors $S(Q)$ (Te far-edge measurements) and $\Delta_k S(Q)$'s for the Ge, Sb and Te K edges. Squares indicate data obtained from the AXS experiments, and red solid curves denote the fits by RMC modelling. a) GeTe, b) GST-8,2,11, c) GST-2,2,5, d) GST-1,4,7.

5.2.1 Partial structure factors of the GeSbTe glasses

The partial structure factors obtained from the RMC simulations are displayed for all GST compositions in fig. 47. Note that the information content of the Ge-based correlations in GST-1,4,7 is quite low. The $S_{ij}(Q)$ functions are sorted by correlation in order to facilitate the overview about the development of the individual partial correlations as a function of Sb_2Te_3 content, which are to be discussed in the following.

Ge-Ge: There is an intense FSDP at 0.95 $Å^{-1}$ of germanium telluride, indicating a high degree of intermediate range order among the Ge atoms. This peak is still visible in GST-8,2,11, but decreases for larger Sb_2Te_3 concentrations. A decreasing trend also applies to the peak at the Q_2 position, whereas the peak at $Q_3 = 3.45$ $Å^{-1}$ only decreases slightly, and broadens in GST-2,2,5. The shoulder observed for the Q_3 peaks is found to represent the main reason for the shoulder of the Q_3 peak in the total $S(Q)$. Note that the Ge-Ge correlation of GST-1,4,7 may not be significant, as the information content on the Ge atoms is too low due to the missing $\Delta_{\mathrm{Ge}}S(Q)$ dataset.

Ge-Sb: In general, the observed peaks in the Ge-Sb correlations are comparably small. Otherwise, the correlations are strikingly different in all three compositions containing antimony. The position of the Q_2 and the Q_3 peak shifts between the compositions. In GST-2,2,5, the Q_2 peak is distorted towards the low-Q side. Apart from that, a FSDP is observed only in GST-8,2,11, indicating that the IRO also extends on the Ge-Sb correlation.

Ge-Te: A small angle scattering signal resulting in a minimum at about 1.5 $Å^{-1}$ is consistently observed in all compositions, though the minimum shifts about 0.2 $Å^{-1}$ for higher contents of Sb_2Te_3. Intensities of the signals at Q_2 and Q_3 decrease similar to the Ge-Ge correlation described above, but the peak intensity at Q_4 remains constant except for GST-1,4,7.

Sb-Sb: Due to the low Sb content in GST-8,2,11, $S_{\mathrm{SbSb}}(Q)$ possesses a high statistical error. Nonetheless, a peak at $Q_2 \approx 2$ $Å^{-1}$ is clearly observed in all compositions, though with a reduced intensity in GST-1,4,7. The Q_3 peak is also found to be comparably small in this composition.

Sb-Te: All graphs resemble the total structure factor. Peaks at Q_2 and Q_3 are consistently observed with similar intensity ratios. On the other hand, the Q_3 peaks becomes

more and more asymmetric towards the low-Q side, thereby constituting the major contribution to the asymmetry in the total $S(Q)$. Furthermore, major oscillations are found to persist in the high-Q region, most notably for GST-2,2,5, which are indicative of a strong SRO. A small FSDP is developing for GST-1,4,7 around 1 $Å^{-1}$; this peak is shifted to higher Q-values compared to the FSDP of the Ge-Ge correlations in the GeTe-rich compositions, and may be regarded as the main reason for the shift of the FSDP in the total $S(Q)$.

Te-Te: All graphs resemble the total structure factor, but exhibit a larger amplitude. A FSDP is missing in all compositions. Peaks at Q_2 and Q_3 are observed consistently with a similar intensity ratio. Oscillations at high Q-values are generally less developed than those in the Sb-Te correlations.

Summarizing the results on the FSDP, it is striking that the most commonly employed and investigated $Ge_2Sb_2Te_5$ possesses a special position within the compositions along the pseudo-binary line: the prominence of the intermediate range order, as represented by the presence of FSDPs at the Q_1 position, is very low. For the more GeTe-rich compositions, a FSDP in the Ge-Ge and also in the Ge-Sb correlations is observed; these features decrease, however, as a function of the Sb_2Te_3 content. For higher Sb_2Te_3 concentrations, on the other hand, an increasing FSDP among the Sb-Te correlation is found. Note that the latter trend will have to be confirmed by a simulation containing the $\Delta_{Ge}S(Q)$ as well.

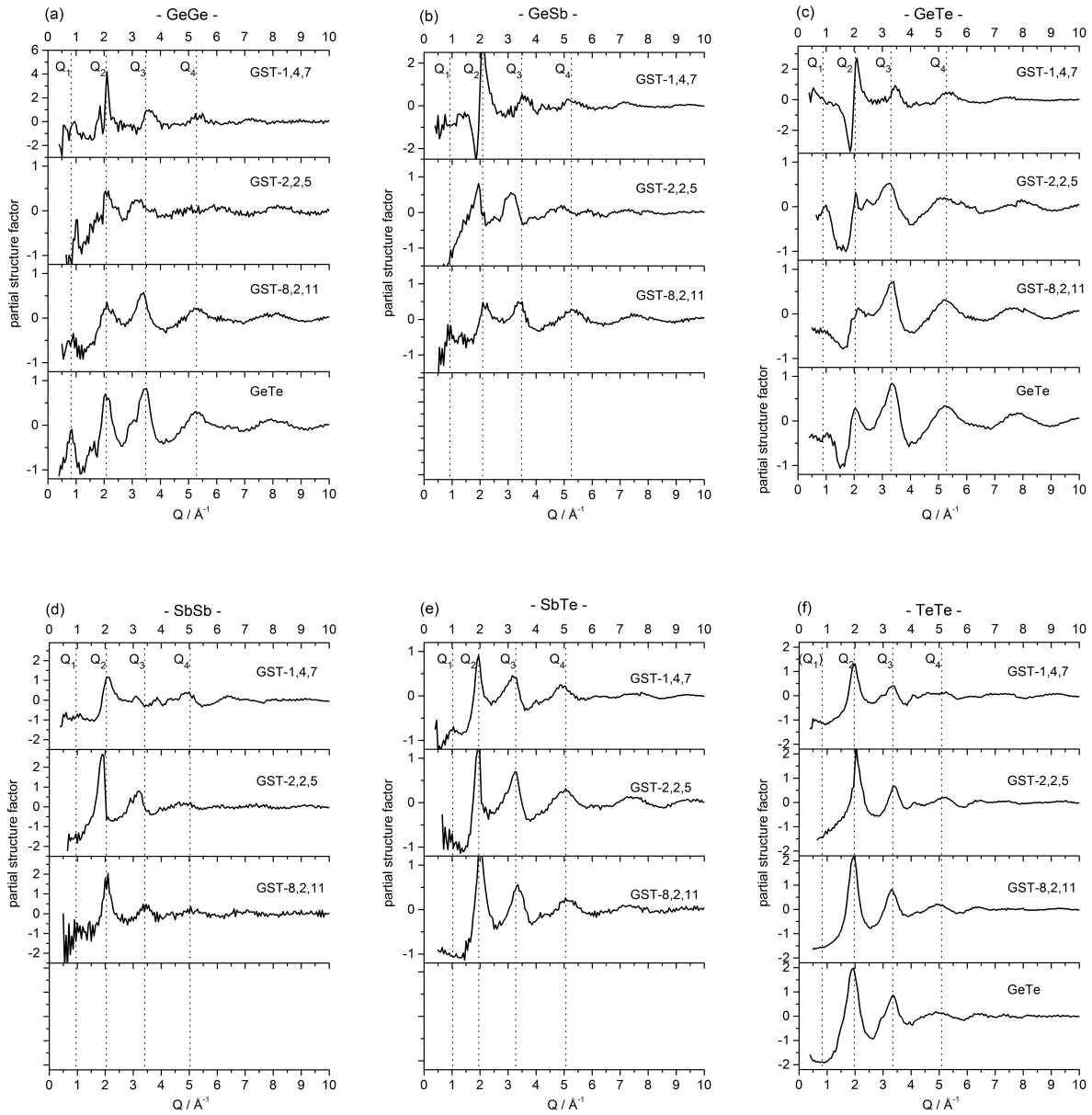

Figure 47: Partial structure factors $S_{ij}(Q)-1$ obtained by RMC for the GST compositions, ordered by correlation: a) Ge-Ge, b) Ge-Sb, c) Ge-Te, d) Sb-Sb, e) Sb-Te, f) Te-Te. Vertical dotted lines indicate distinct peak positions and are a guide for the eye.

5.2.2 Partial pair correlation functions

The partial pair correlation functions obtained from the RMC simulations for the different $(GeTe)_{1-x}(Sb_2Te_3)_x$ glasses are displayed in fig. 48, again ordered by correlation rather than by composition. It can be noticed immediately that the interatomic distances, as represented by the peaks of the first coordination shells, in general remain constant within about ± 0.1 Å (i.e. the r-spacing value chosen for the RMC modelling). A notable exception is constituted by the Ge-based correlations in GST-1,4,7 - but as described above, since the experimental information on these correlations is low, it cannot be decided whether these features are meaningful or not. The other distances are summarized in table 10. The agreement with comparable data on GeTe [89] and GST-2,2,5 [79, 84, 86] is quite good. Distances of second-neighbour coordination are displayed in tab. 11.

The coordination numbers obtained from the pair correlation functions are summarized in table 12. Cut-off values for the calculation of the integrals were set to 3.15 Å for the Ge-Ge and Ge-Te correlations, and 3.25 Å for all other correlations, corresponding to the first minima in the partial pair correlation functions. It is found that the individual average coordination numbers amount to a value near 3 with a decreasing trend, in contrast to the development in the total $g(r)$ functions. This trend qualitatively agrees with the development of the average coordination numbers expected from the $8-N$ rule, as shown in table 12; this rule predicts a decreasing CN as a function of x, ranging from 3 for GeTe to 2.5 in the case of GST-1,4,7.

In the following, I will give a brief summary of the trends observed in the individual correlations, based on fig. 48 and tables 10-13. A detailed comparison with other studies follows for each composition individually in tables 14 to 16.

Ge-Ge: Homopolar Ge-Ge bonds with a bond length of 2.55 Å play a significant role in the configuration of germanium telluride, constituting about 40% of the Ge-based bonds with a CN of 1.57. Their significance decreases, however, as a function of x, and thus the CN is only 0.12 for high Sb_2Te_3 contents. As expected from the relative elemental ratios, this effect is observable already for small amounts of Sb added to the GeTe structure, so that the CN decreases by about 22% from GeTe to GST-8,2,11. The second peak of this correlation is situated constant at 4.1 Å and decreases in intensity from GeTe to GST-1,4,7.

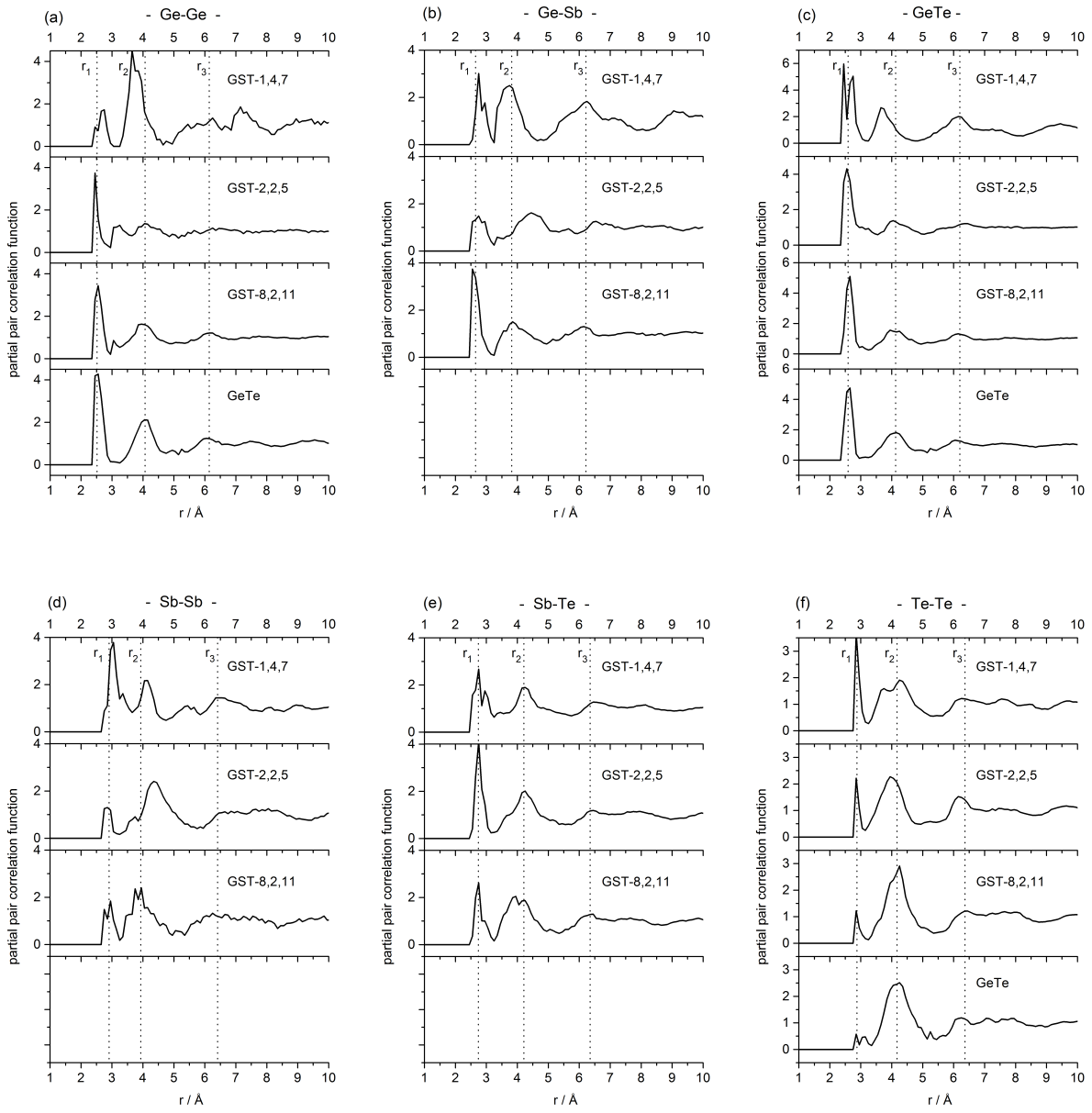

Figure 48: Partial pair correlations functions $g_{ij}(Q)$ obtained by RMC for the GST compositions, ordered by correlation: a) Ge-Ge, b) Ge-Sb, c) Ge-Te, d) Sb-Sb, e) Sb-Te, f) Te-Te. Vertical dotted lines indicate distinct peak positions and are a guide for the eye.

Ge-Sb: The Ge-Sb bond near 2.70 Å increases in its coordination number from 0.31 in GST-8,2,11 to 0.54 in GST-2,2,5 and 0.83 in GST-1,4,7. Analogously, the Sb-Ge coordination number decreases from 1.26 to 0.21, as shown in tab. 12. The position of the second peak varies strongly.

Ge-Te: The first peak at 2.6 Å remains constant in shape and position. The second peak is also constantly located at 4.1 Å (except again for GST-1,4,7), but decreases in intensity. Also visible is a comparably pronounced third peak near 6.1 Å. The Ge-Te coordination number is found to possess the highest value among all partials in all compositions, rising from 2.23 in GeTe to 2.81 in GST-1,4,7. The Te-Ge CN, on the other hand, decreases sharply to 0.40 in GST-1,4,7.

Sb-Sb: The homopolar Sb-Sb distance is 2.85 Å, having a low coordination number of 0.20 and 0.32 in the GeTe-richer compositions, but increasing strikingly in GST-1,4,7 to 1.30. This correlation is sometimes excluded in the investigation of GST-2,2,5 (e.g. [79]) - and the low CN found here supports this assumption - but it is found to be definitely significant in GST-1,4,7. The second peak varies in position between 3.9 and 4.4 Å, and is found to be most prominent in GST-2,2,5.

Sb-Te: The first and second peaks are situated constant at 2.75 and 4.2 Å, respectively, though the second peak exhibits a pronounced shoulder at about 3.6 Å in all cases. The Sb-Te coordination increases from 1.31 in GST-8,2,11 to about 1.96 in GST-2,2,5 and 1.74 in GST-1,4,7. The Te-Sb coordination number rises as well from a negligible value in GST-8,2,11 to about 0.99 in GST-1,4,7.

Te-Te: The CN of the homopolar Te-Te bond at about 2.90 Å is quite small in the GeTe-rich compositions, but rises to 0.77 in GST-2,2,5 and even to 1.14 in GST-1,4,7. Contrary to assumptions of other studies (cf. [78, 81, 88]), it is thus suggested to be a significant correlation. Interestingly, the second peak at 4.2 Å decreases only slightly in intensity, and appears to be split into two separate contributions in GST-1,4,7, with the new peak situated at 3.8 Å. Together with the Sb-Te correlation, Te-Te bonds are thus the major reason for the asymmetry of the r_2 peak observed in the total $g(r)$.

Total coordination numbers deviate significantly from the $8 - N$ rule, which would predict N(Ge)=4, N(Sb)=3 and N(Te)=2. All values are found to be close to N(Ge)=3.8, N(Sb)=2.9 and N(Te)=2.5. Ge atoms therefore appear to be slightly under-coordinated,

Table 10: Interatomic distances in Å obtained by RMC, in comparison with values from other investigations for the GeTe [89] and GST-2,2,5 glasses [75, 81, 84, 86].

correlation	this work	EXAFS [89]	EXAFS [81]	EXAFS[75]	DFT [84]	DFT [86]
Ge-Ge	2.55	2.5	2.48		2.54	
Ge-Sb	2.70		2.69		2.75	
Ge-Te	2.60	2.6	2.6	2.61	2.73	2.70
Sb-Sb	2.85				2.92	
Sb-Te	2.75		2.82	2.85	2.88	2.82
Te-Te	2.90	2.7			2.85	

whereas the Te atoms are found to be over-coordinated by nearly 25%, with the lowest CN observed in GST-8,2,11, where N(Te)=2.39. This behaviour offers an interesting insight into the structural reorganization of the amorphous network of GeTe upon addition of a small amount of Sb_2Te_3. The development of the partial coordination numbers of the Ge-Ge, Ge-Te and Te-Te correlations from GeTe to GST-8,2,11 quantitatively follows the expectations from the respective concentration ratios (Ge 50% to 38%, and Te 50% to 52%). Thus, in the case of germanium, antimony atoms compensate for the overall loss in the coordination sphere (i.e. without Sb, the Ge atoms would be less than fourfold coordinated). On the other hand, the coordination of Sb atoms around Te is not growing sufficiently to preserve a total coordination number comparable to the other GST glasses. Furthermore, it is noteworthy that the difference between the average CN from the experiment to the values from the $8-N$ rule is growing: for low Sb_2Te_3 contents, the difference is about 0.15, increasing to 0.27 (GST-2,2,5) and 0.37 in GST-1,4,7.

Table 13 lists the fractions of homopolar bonds $P_i^{\text{homopolar}}$ (i.e. the homoatomar correlations Ge-Ge, Sb-Sb and Te-Te, but also Ge-Sb, as both are considered as formal cations) extracted from tab. 12. These bonds are also called "wrong bonds" sometimes, as they are not observed in the corresponding crystal. However, these bonds are found to be a dominant characteristic of the amorphous phase with an overall ratio of more than 25% in all compositions. The average contribution even exhibits an increasing trend as a function of x, although the fraction of Ge-based bonds is largely shrinking.

Table 11: Higher order coordination shell distances in Å for the GST glasses. Ge-based correlations in GST-1,4,7 are in parentheses (see text).

correlation	second peak				third peak			
	GeTe	8,2,11	2,2,5	1,4,7	GeTe	8,2,11	2,2,5	1,4,7
Ge-Ge	4.1	4.1	4.1	(3.8)	6.1	6.1	6.1	6.1
Ge-Sb	-	3.9	4.4	(3.8)	-	6.2	6.5	(6.2)
Ge-Te	4.1	4.1	4.1	(3.8)	6.1	6.1	6.1	6.1
Sb-Sb	-	3.9	4.4	4.1				
Sb-Te	-	4.2	4.2	4.2	6.4	6.4	6.4	6.4
Te-Te	4.2	4.2	4.2	4.2	6.2	6.2	6.2	6.2

Table 12: Partial and total coordination numbers of the first coordination shell in the GST glasses obtained by AXS/RMC. Coordination numbers have been calculated by integrating the respective coordination shells in the $g_{ij}(r)$. For comparison, values for the average CN expected by the $8-N$ rule are listed as well.

	GeTe	GST-8,2,11	GST-2,2,5	GST-1,4,7
$x =$	0	1/9	1/3	2/3
correlation	partial coordination numbers n_{ij}			
Ge-Ge	1.57	1.23	0.54	0.12
Ge-Sb	-	0.31	0.54	0.83
Ge-Te	2.23	2.38	2.71	2.81
Sb-Ge	-	1.26	0.54	0.21
Sb-Sb	-	0.20	0.32	1.30
Sb-Te	-	1.31	1.96	1.74
Te-Ge	2.23	1.73	1.08	0.40
Te-Sb	-	0.24	0.79	0.99
Te-Te	0.30	0.42	0.77	1.14
correlation	total coordination numbers $N(i)$			
N(Ge)	3.80	3.93	3.79	3.76
N(Sb)	-	2.77	2.82	3.25
N(Te)	2.53	2.39	2.64	2.53
$\langle N \rangle$	3.16	3.01	2.94	2.87
$\langle N \rangle_{8-N}$	3.00	2.86	2.67	2.50

Table 13: Homopolar bond contributions $P_i^{\text{homopolar}}$ in the GST glasses, for all elements i, and the average value $P_{\text{average}}^{\text{homopolar}}$.

correlation	GeTe	GST-8,2,11	GST-2,2,5	GST-1,4,7
$P_{\text{Ge}}^{\text{homopolar}}$	41.3%	39.2%	28.5%	25.3%
$P_{\text{Sb}}^{\text{homopolar}}$	0%	52.7%	30.5%	46.5%
$P_{\text{Te}}^{\text{homopolar}}$	11.9%	17.6%	29.2%	45.1%
$P_{\text{average}}^{\text{homopolar}}$	26.6%	29.2%	29.3%	43.9%

Comparison with other studies The obtained coordination numbers are compared in tables 14 to 16 with results from experimental [78, 81, 88, 89, 91, 92] and theoretical investigations [83, 84, 86] on GeSbTe. It should be noted that the coordination numbers presented here naturally depend on the chosen cut-off criterion, which may differ between the studies and which is not always stated explicitly.

In the case of germanium telluride (**GeTe**), the best agreement with the current AXS/RMC results is found for the EXAFS investigation by van Eijk [91]. Strikingly, even within the same experimental method, quite different CN are found by Jóvári et al., see table 14. The latter one is the only study that agrees with the $8 - N$ rule reporting a CN of about 4 for Ge and about 2 for Te. Other studies as well as the current AXS/RMC approach result in a considerably higher CN for tellurium. Experimental techniques predict a ratio of Ge-Te to Ge-Ge bonds of about 2 : 2 (i.e. about 2.2 : 1.6 in the present study and in [91], and 1.5 : 2.3 in [89]) and a significant number of Te-Te homopolar bonds. In contrast, the values found by Akola and Jones by *ab-initio* MD predict a quite different coordination of the Ge atoms with n_{GeTe}=3.2 and n_{GeGe}=1.1 and a very small contribution of Te-Te with n_{TeTe}=0.1. With respect to the experimental findings, the DFT calculations may therefore be regarded as underestimating the contribution of homopolar bonds.

For the composition $\mathbf{Ge_8Sb_2Te_{11}}$, few comparable investigations have been published, cf. tab. 15. Both the theoretical work by Akola and the experimental work by van Eijk highly disagree with the $8 - N$ rule, the latter even for Ge and Sb atoms. This trend is not in line with results on other compositions along the *tie*-line (in general, only Te is

Table 14: Coordination numbers of GeTe in comparison with other studies. Note that values in [89] have been extrapolated to $Ge_{50}Te_{50}$, as the study covers only the compositions $12 \leq x \leq 44.6$ in Ge_xTe_{100-x}.

	this work	EXAFS [89]	EXAFS [91]	DFT [84]
correlation	partial coordination numbers n_{ij}			
GeGe	1.57	2.45	1.7	1.1
GeTe	2.23	1.50	2.3	3.2
TeTe	0.30	0.60	0.3	0.1
correlation	total coordination numbers $N(i)$			
N(Ge)	3.80	3.95	4	4.2
N(Te)	2.53	2.10	2.6	3.3
$\langle N \rangle$	3.16	3.03	3.3	3.75

Table 15: Coordination numbers of GST-8,2,11 in comparison with other studies.

	this study	DFT[84]	EXAFS[91]
correlation	partial coordination numbers n_{ij}		
GeGe	1.23	0.7	2.1
GeSb	0.31	0.2	0.4
GeTe	2.38	3.2	3
SbGe	1.26	0.6	1.7
SbSb	0.20	0.2	0
SbTe	1.31	2.8	2.2
TeGe	1.73	2.3	2.18
TeSb	0.24	0.5	0.42
TeTe	0.42	0.1	0
correlation	total coordination numbers $N(i)$		
N(Ge)	3.93	4.0	5.5
N(Sb)	2.77	3.7	3.9
N(Te)	2.39	2.9	2.6
$\langle N \rangle$	3.01	3.4	3.83

found to exhibit major deviations from the $8 - N$-rule) and may therefore be considered with some caution. It is for example not pointed out why van Eijk [91] excluded Te-Te bonds in GST-8,2,11 (x_{Te}=0.52), when at the same time this correlation is reported to be significant in GeTe (x_{Te}=0.50) in the same study. Also, Ge-Ge and Ge-Te bonds appear to be somewhat overestimated. In the DFT study, the ratio of the correlations Ge-Te : (Ge-Ge + Ge-Sb) is 3.2 : 0.9, compared to 2.38 : 1.54 in the current AXS/RMC approach, displaying the same development that was observed in germanium telluride.

GST-2,2,5 gives an interesting example of the importance of allowing homopolar Te-Te and Sb-Sb bonds in the configuration, see tab. 16. These bonds have a major effect on the Ge-Te network via a "cross-talk" between the correlations: Introducing Te-Te bonds in the coordination shell of Te reduces the number of Ge and Sb neighbours, thus concomitantly reducing the CN of Te around Ge. This development can be seen by comparing the results of the present AXS/RMC scheme with the simulations by Hosokawa et al. [88], who used the same sets of experimental data: without Te-Te bonds, a CN of 3.26 is found. It may be noted that Ohara and coworkes report the same number [92]. On the other hand, the lower CN of 2.71 has also been found by EXAFS measurements [78, 81] and is in line with the general trend observed in the *tie*-line compositions. A n_{GeTe} as high as 3.26 would disagree with the steadily decreasing development of the CN as a function of the Sb_2Te_3 content. Furthermore, although technically Te-Te bonds have been allowed in [92], no differential structure factor of the Ge absorption edge was included in the modelling procedure, so that the information content on Ge is rather low. This shortcoming can also be seen in the reported Ge-Sb and Ge-Ge pair correlations functions, which largely deviate from all other studies cited before. Theoretical characterizations of GST-2,2,5 based on DFT simulations again find a high number of Ge-Te bonds and only small contributions from homopolar correlations [83, 84]. However, all average CN are much higher than in the experimental works, representing again the major conflict between both approaches.

Table 16: Coordination numbers of GST-2,2,5 in comparison with other studies.

	this study	AXS/RMC[88]	AXS/RMC[92]	EXAFS[78, 81]	DFT[83, 84]
correlation			partial coordination numbers n_{ij}		
GeGe	0.54	0.70	0.39	0.79	0.4
GeSb	0.54	0.28	0.18	0.60	0.2
GeTe	2.71	3.26	3.26	2.46	3.6
SbGe	0.54	0.44	0.18	0.60	0.2
SbSb	0.32	0.00	0.51	-	0.6
SbTe	1.96	2.51	2.37	2.52	2.9
TeGe	1.08	1.30	1.30	0.98	1.4
TeSb	0.79	1.00	0.95	1.01	1.2
TeTe	0.77	0.00	0.20	-	0.3
correlation			total coordination numbers $N(i)$		
N(Ge)	3.79	4.24	3.83	3.85	4.2
N(Sb)	2.82	2.95	3.06	3.12	3.7
N(Te)	2.64	2.30	2.45	1.99	2.9
$\langle N \rangle$	2.94	2.88	2.89	2.65	3.37

In comparison with the investigations cited above, two further constraints on the RMC simulation were tested. They are compared with the original simulations by the goodness of fit values R_w. These values range between 0.03 - 0.1 for the total and between 0.1 - 0.35 for the differential scattering functions, respectively, for the original simulations.

First, the system was forced to adopt total coordination numbers given by the $8 - N$ rule. For "weak" constraints on the coordination numbers, i.e. using comparably high σ-values, it is found that Ge and Sb easily adopt the required CN, but Te is always over-coordinated. The Te atoms thereby ensure the overall average CN defined by the total correlation functions. This is true for all compositions under investigation. The R_W values of the individual scattering functions $\Delta_k S(Q)$ and $S(Q)$ rise by 5-10%. Since the CN of the Ge and Sb atoms are already close to the $8 - N$ rule value and Te is still over-coordinated, this constraint only has a minor impact on the actual configuration. For a "stronger" constraint, the Te atoms can be forced to adopt a CN of about 2 as well, but only if the strength of the $8 - N$ constraint is increased so far that the agreement between simulation and experimental data is considerably debased.

Secondly, an exclusion of Te-Te bonds was tested. Therefor, the minimal Te-Te distance during the RMC modelling was raised to 3.2 Å. It is found that the R_W values of the

scattering functions raise only slightly for GeTe and GST-8,2,11 (in the order of about 1% for each function). This is not unexpected, because the CN of Te-Te is already quite low in these compositions. The existence of Te-Te homopolar bonds may thus be questioned and their exclusion as assumed e.g. in [91] cannot be rebutted on the basis of the goodness of fit for small Sb_2Te_3 concentrations. In contrast, the R_W values for GST-2,2,5 and GST-1,4,7 increase considerably for this constraint. Whereas the total structure factor in GST-2,2,5 is described nearly equally well (R_W increases only by 0.5%), it is found that the differential structure factors are described considerably worse: the R_W for $\Delta_{\mathrm{Te}}S(Q)$ increases by 25%, and the R_W for $\Delta_{\mathrm{Sb}}S(Q)$ by 16%. Only the value for $\Delta_{\mathrm{Ge}}S(Q)$ remains nearly constant. In the case of GST-1,4,7, even the agreement of the simulation with the total structure factor worsens, with an increase in the R_W value of 23%. Furthermore, the R_W values of the differential structure factors rise as well by about 20%. It may also be noted that the interatomic distance of Te-Te bonds in amorphous elemental tellurium has only recently been reported with $r_{\mathrm{TeTe}} \approx 2.8$ Å [93], which is just slightly smaller than the distance found with the present AXS/RMC approach. It can thus be concluded that the Te-Te bond is definitely necessary in GST-1,4,7 for an accurate structural characterization, and in GST-2,2,5 it is the element specific information provided by the differential structure factors that shows the need for including this correlation in the overall structure.

5.2.3 Bond angle analysis

Bond angle distributions (BAD) are well investigated for GST-2,2,5 and show a remarkable agreement between theoretical and experimental investigations. For example, the Te-Ge-Te angle is reported by Jóvári with a broad distribution peaking around 105°, indicating a dominant contribution of tetrahedrally coordinated (109.5°) Ge atoms mixed with an octahedral coordination (90°) [78, 81]. Kolobov et al. report that the optical properties in GST can only be reproduced if a fraction of 50% of the Ge atoms occupy tetrahedral sites, and the remaining Ge atoms are situated in distorted octahedral sites [75]. They conclude that this kind of coordination would lead to an average coordination number between 3 and 4. Akola and Jones report a peak at 94°, but the peak shifts to higher angles when smaller distances are considered [83, 84]. That is, distributions close to 109.5° are observed if only distances up to 2.7 Å are considered. Both findings are in

agreement with the AXS/RMC study of Hosokawa et al., who find nearly equal portions of octahedral and tetrahedral symmetries [88] for the Te-Ge-Te angle.

Bond angle distributions obtained from the present AXS/RMC study are displayed in figures 49 - 51. The BAD around Ge, Sb and Te atoms are illustrated in fig. 49. Majorly, distributions around 100° are observed, with a tendency to smaller angles in GST-1,4,7, indicating a mix of octahedral and tetrahedral sites. Note that the sharp spikes for GST-1,4,7 in fig. 49 a) result from the small number of Ge atoms and the structural constraints applied during the RMC scheme (i.e. that 90% of the Ge atoms were forced to possess exactly four neighbours). The overall BAD's can be partitioned into individual angle distributions; considering the partial coordination numbers from tab. 12, the bond angles with the highest relative weight are Te-Ge-Te, Te-Sb-Te and Ge-Ge-Ge, which are shown individually in fig. 50 for all compositions. The maximum of the distribution of the Te-Ge-Te bond angles shifts gradually as a function of $x_{Sb_2Te_3}$ from about 108° in GeTe to smaller angles, indicating a growing contribution from octahedral sites. A further partition of this angle is given in fig. 51. In contrast, neither the Te-Sb-Te nor the Ge-Ge-Ge angle exhibits a similar clear trend; the distributions are centered broadly around 100°.

With respect to the findings by Akola et al., the dependence of the BAD on the distance to the central atom is investigated. Fig. 51 shows the results for the Te-Ge-Te bond angle in the GST glasses for a partition of the angle distribution in 0.1 Å segments. It is found that small bond distances adopt a higher angle, and higher distances adopt smaller angles. In particular, the maximum of $g_{GeTe}(r)$ at 2.6 Å provides a separation in so far that smaller distances are closer to a tetrahedral angle and larger distances are closer to an octahedral coordination. Similar developments are found in all compositions, but the BAD maxima above 2.6 Å gradually shift even closer to 90° as a function of the composition, whereas the lower distance BAD's remain comparably constant. These distributions have an interesting effect on the Ge-Te network structure, which will be discussed in section 5.2.4.

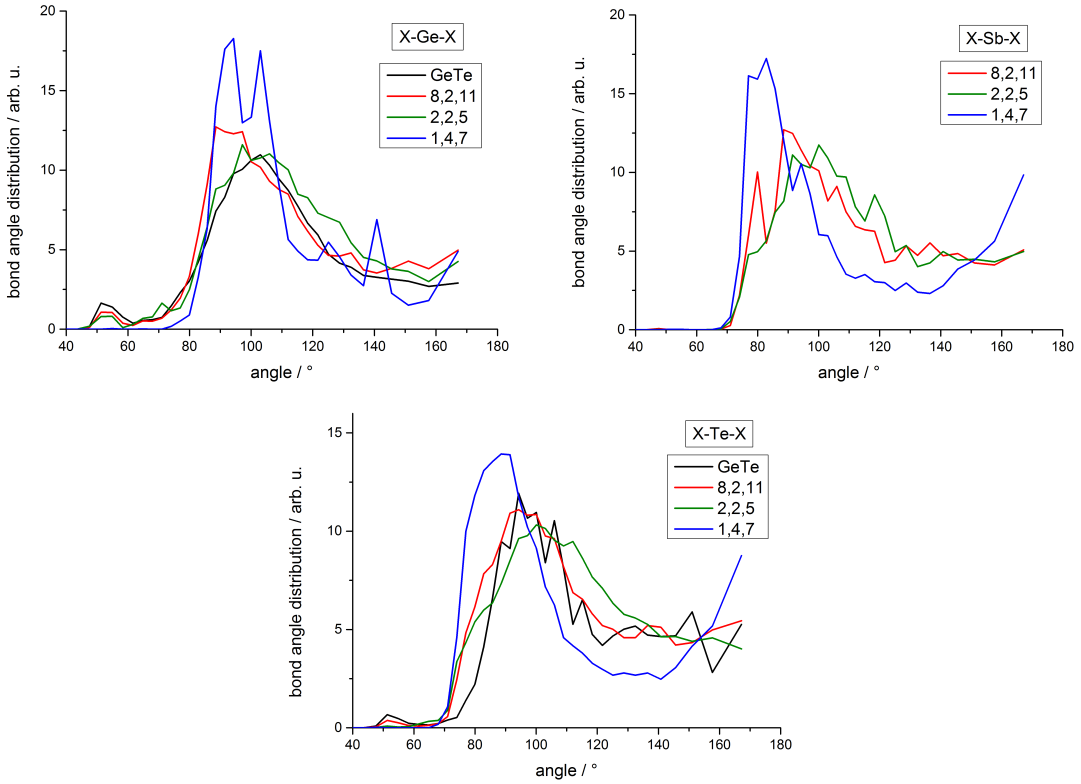

Figure 49: Bond angle distributions around each element in GST glasses. Angles around Ge atoms (a), Sb (b) and Te (c), for all compositions: GeTe (black), GST-8,2,11 (red), GST-2,2,5 (green), GST-1,4,7 (blue).

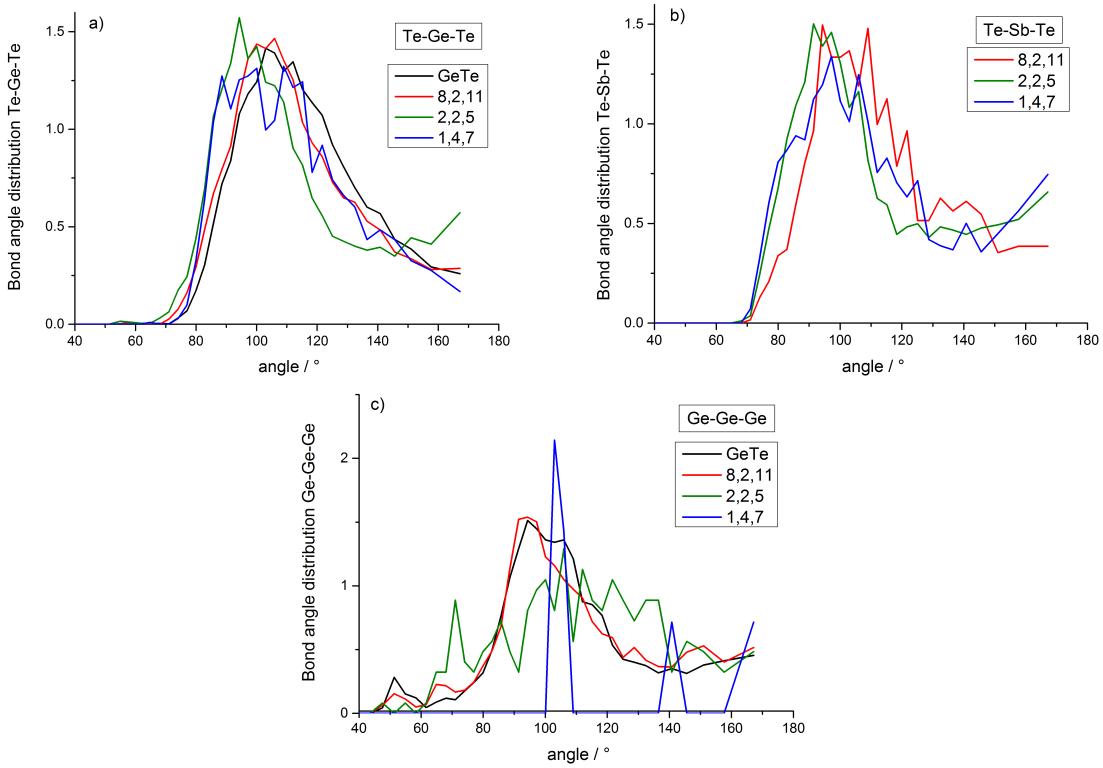

Figure 50: Te-Ge-Te (a), Te-Sb-Te (b) and Ge-Ge-Ge (c) bond angle distributions in the GST glasses. GeTe (black), GST-8,2,11 (red), GST-2,2,5 (green), GST-1,4,7 (blue).

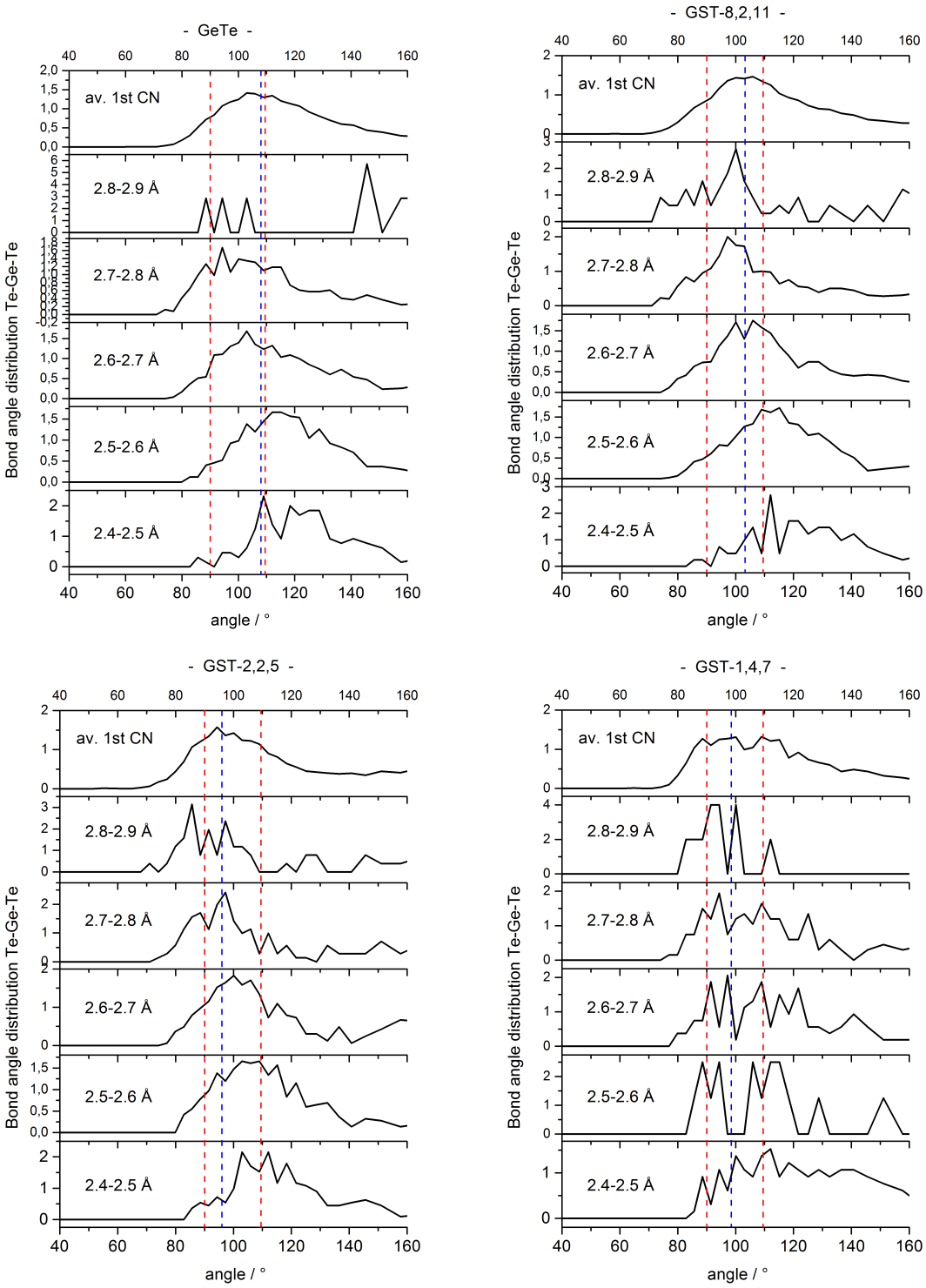

Figure 51: Evolution of the Te-Ge-Te bond angle with the cut-off distance, in GST glasses. Cut-off distances were chosen between 2.5 and 2.9 Å with steps of 0.1 Å. The uppermost graphs shows the overall distribution in the first coordination sphere, and dashed red lines indicate angles of 90° and 109.5°, respectively (red) as well as the position of the maximum in the total distribution (blue).

5.2.4 Intermediate range order

The three dimensional configurations obtained by RMC provide a basis to visualize the network structures forming in the GeSbTe glasses. The following section will give a discussion of the prominent network characteristics and their relation to the SRO parameters discussed above in terms of their structural hierarchy. In this respect, the main correlations forming the amorphous network are Ge-Ge and Ge-X_4 (X = Ge, Sb, Te). A different approach to discuss the IRO is the investigation of distributions of ring structures, which follows in the second part of the section.

As discussed earlier (see section 2.4), the occurrence of a FSDP can be interpreted as a sign for intermediate range order. In this respect, the closer investigation of the Ge-Ge correlation may provide an initial access to understand the IRO in the GST glasses, as it is most pronounced in this correlation.

The Ge-Ge FSDP's have been fitted with Gaussian functions in order to determine their characteristic values, which are summarized in table 17. It should be noted that the values for GST-1,4,7 are not given, as the Ge-Ge correlations especially at low-Q may not be reliable enough without the Ge differential structure factor. It is found that the FSDP position shifts to higher Q-values already for low Sb_2Te_3 concentrations ($Q_{1,\mathrm{GeTe}}$=0.82 Å^{-1} and $Q_{1,\mathrm{GST-8,2,11}}$=0.87 Å^{-1}), thus causing the characteristic length to shorten correspondingly from 7.7 Å to 7.2 Å. The area under the peak decreases slightly from GeTe to GST-8,2,11 but the peak broadens from $\Delta Q_{1,\mathrm{GeTe}}$=0.36 Å^{-1} to $\Delta Q_{1,\mathrm{GST-8,2,11}}$=0.55 Å^{-1}. In GST-2,2,5, the intensity of the Ge-Ge FSDP is highly reduced and its area constitutes only 29% of the peak in germanium telluride. The characteristic length shortens further to 6.3 Å. Whether the Ge-Ge FSDP vanishes completely for Sb_2Te_3 concentrations higher than $x = \frac{1}{3}$ will have to be checked based on the $\Delta_{\mathrm{Ge}}S(Q)$ measurement of GST-1,4,7. Thereby, it should also be possible to investigate the development of the FWHM values, which does not exhibit a consistent trend in the different compositions.

Nonetheless, the impact of the decreasing contribution of this signal from GeTe to GST-2,2,5 can be visualized in the Ge-Ge network structure. These networks are shown as 64x64 Å^2 sections of the RMC configurations in fig. 52 for all GST compositions. The fragmentation of the Ge-Ge bonds shown in red and a reduction of the chain lengths is clearly visible.

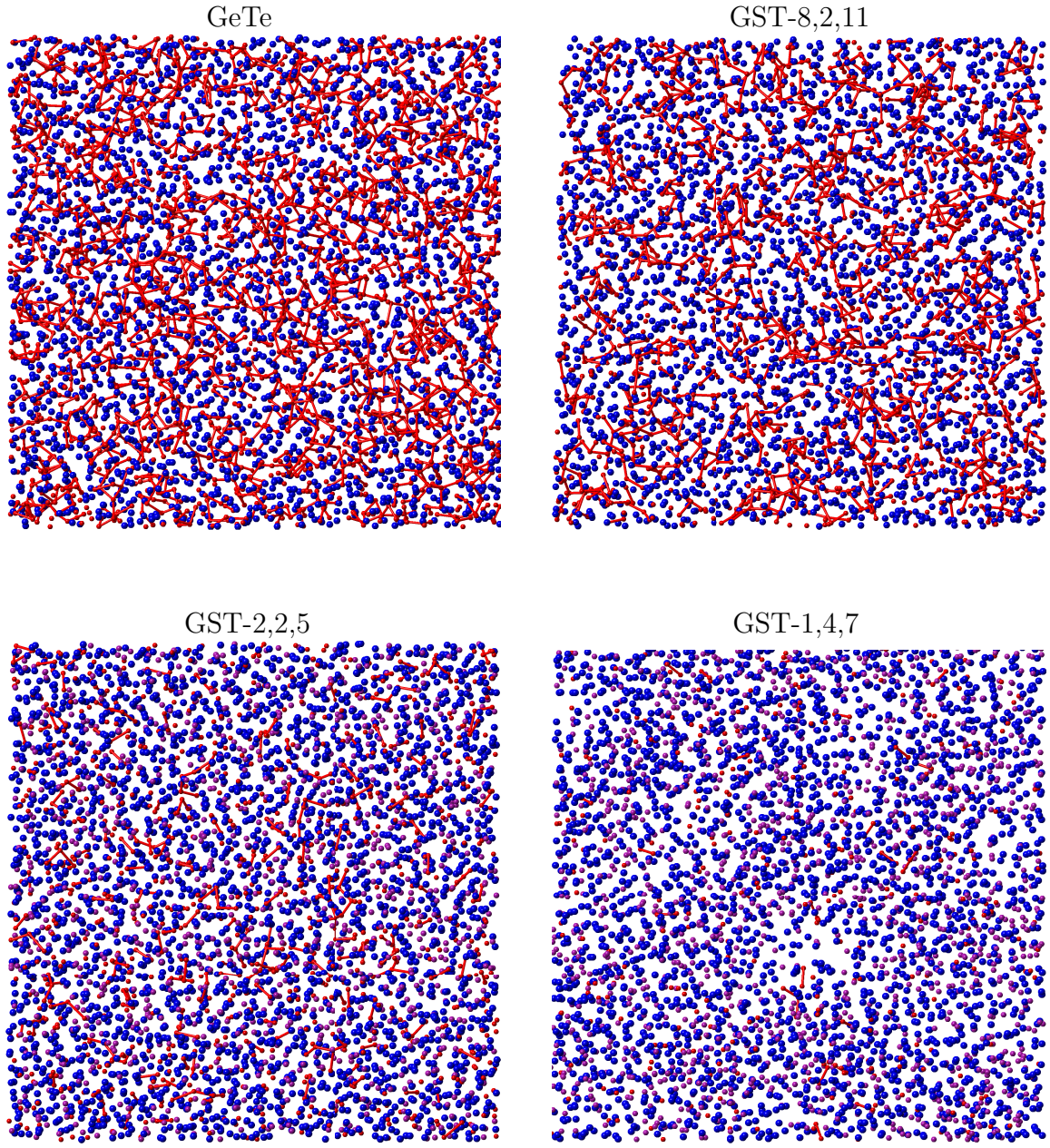

Figure 52: 64x64x15 $Å^3$ sections of the configurations of the four GST compositions, illustrating the Ge network structure in GeTe (upper left), GST-8,2,11 (upper right), GST-2,2,5 (lower left) and GST-1,4,7 (lower right). Ge atoms are displayed in red, Sb: violet and Te: blue. Ge-Ge bonds are marked as red bars.

Table 17: Characteristics of the Ge-Ge FSDP for all compositions. Given are the area of the peak relative to the FSDP in GeTe, the FWHM ΔQ_1 of the peak, the position in $Å^{-1}$ and the corresponding characteristic length R_c.

Composition	Position / $Å^{-1}$	rel. Area	ΔQ_1 / $Å^{-1}$	R_c / Å
GeTe	0.82	1.00	0.36	7.7
$Ge_8Sb_2Te_{11}$	0.87	0.88	0.55	7.2
$Ge_2Sb_2Te_5$	1.00	0.29	0.15	6.3

Another significant aspect of the network structure becomes evident by inspecting the bond angle / bond length division for the Ge-Te correlation (fig. 51). Thereby, two different sub-network structures can be distinguished. One is based on the short Ge-Te bonds adopting higher bond angles, and can be interpreted as a "wide-meshed" network close to a tetrahedral angle, and the other is based on the longer Ge-Te bonds above the distance of the g_{GeTe} maximum, which adopt smaller angles, and may be interpreted as an "close-meshed" network closer to the octahedral angle. Both are illustrated in figures 53 - 55. The total network constituted by the first coordination shell of Ge, which is the sum of both sub-networks, is shown on the right hand side of the figures. Note that all Ge-X (X= Ge, Sb, Te) bonds are included in the coordination polyhedra around Ge, but given from the CN shown in table 12, Ge-Te always constitutes the dominant contribution. It is readily observed that the wide-meshed network accounts for the more dominant contribution in germanium telluride (fig. 53). A similar characteristic is found in the Ag-$GeSe_3$ glasses (see previous chapter), where the tetrahedral Ge-Se_4 building blocks form a strong background network structure. The connectivity of this Ge centered network weakens along the pseudo-binary line due to the decreasing number of Ge atoms. However, keeping in mind the shift of the total BAD around Ge to lower angles as well as the distance dependence of the Te-Ge-Te bond shown in figures 50 and 51, it is not surprising that the wide-meshed network weakens much more than the close-meshed network, as illustrated in figures 54 and 55.

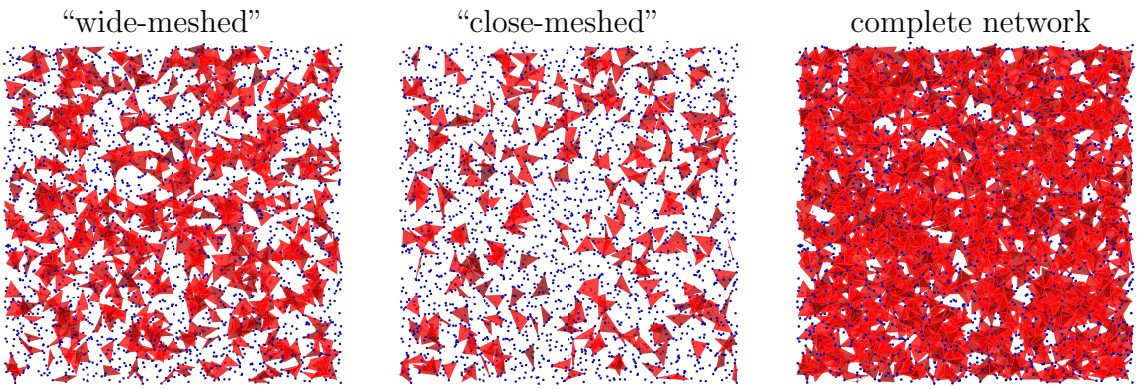

Figure 53: Ge-X network in GeTe. All three figures show the same 64x64 $Å^2$ section of the configuration. Indicated in red are the bonding polyhedra around a central Ge atom. Left: "wide-meshed" network (bond length between 2.4 and 2.6 Å), center: "close-meshed" network (bond length between 2.6 and 3.1 Å), right: Ge-Te network comprising the complete first coordination shell. Ge atoms are displayed in red, Te: blue.

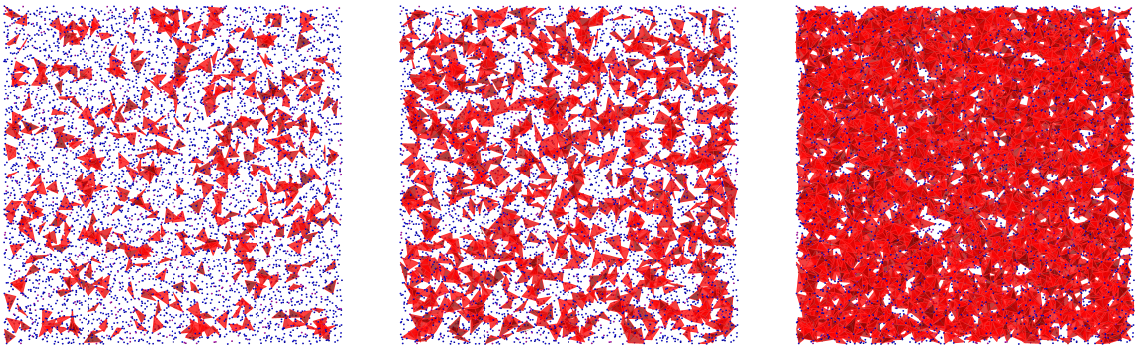

Figure 54: Ge-X network in GST-8,2,11. All three figures show the same 64x64 $Å^2$ section of the configuration. Indicated in red are the bonding polyhedra around a central Ge atom. Left: "wide-meshed" network, center: "close-meshed" network, right: Ge network comprising the complete first coordination shell. Ge atoms: red, Sb: violet and Te: blue.

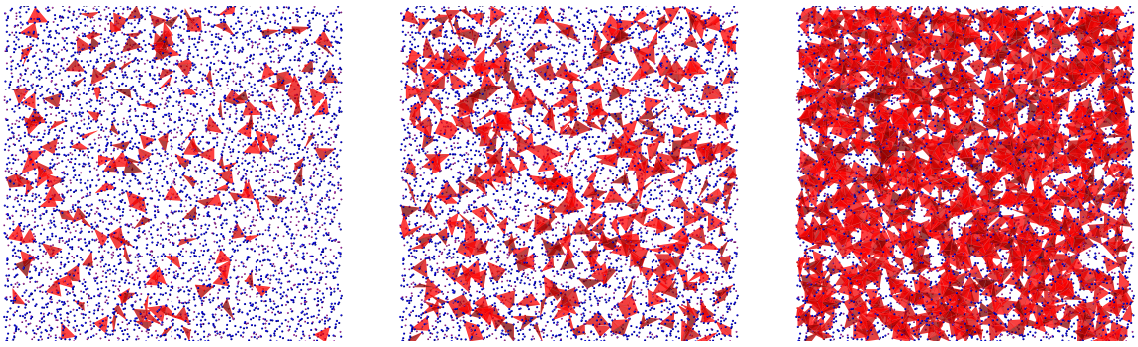

Figure 55: Ge-X network in GST-2,2,5. All three figures show the same 64x64 $Å^2$ section of the configuration. Indicated in red are the bonding polyhedra around a central Ge atom. Left: "wide-meshed" network, center: "close-meshed" network, right: Ge-Te network comprising the complete first coordination shell. Ge atoms: red, Sb: violet and Te: blue.

A different method to interpret the intermediate range order is to calculate the distribution of irreducible ring structures in the amorphous configurations. The possible insights of such ring statistics for GST glasses have been emphasized by Kohara et al. [82] as well as by Akola and Jones [83, 84], who report distinct differences in the ring statistics of GeTe and GST-2,2,5, which are used to explain the enhanced phase change abilities of GST-2,2,5. It is noteworthy that both studies show distinct differences in the actual ring size distributions, and neither is reproduced by the present AXS/RMC approach. Details of this finding are outlined in the following.

Using only high energy x-ray diffraction and a RMC modelling scheme, Kohara et al. compare ring structures of GeTe and GST-2,2,5 in the crystal and in the amorphous form [82]. They find a nearly uniform distribution of rings in GeTe, compared to a strong preference of even-fold rings in GST-2,2,5, with the highest contribution of 6 and 8 membered rings. Since both crystalline phases lack homopolar bonds and thus only contain even-membered rings, most prominently alternating squares, such a ring statistics would explain the higher phase change rate in GST-2,2,5 by the large similarity between the crystalline and the amorphous phase. However, it has to be noted that no element specific information has been included in the modelling procedure of the glasses, so that the results may be ambiguous, especially in so far as they concern the intermediate range order.

Akola and Jones calculated ring statistics for GeTe, GST-8,2,11 and GST-2,2,5 based on DFT simulations [83, 84]. They report a prominent contribution of 4-membered rings in GST-2,2,5 and GST-8,2,11, but rings with a larger number of members are also common. Striking is the strong contribution of strictly alternating $ABAB$ rings (A: Ge, Sb; B: Te), which make up most of the 4- and 6-membered rings, and about half of the 8-rings. On the other hand, GeTe shows a somewhat different ring distribution with nearly equal shares of 4-, 5-, 6- and 7-membered rings, and the highest values for 8-membered rings. Alternating $ABAB$ rings again represent a prominent contribution. This is already suggested by the partial $g(r)$ functions, which indicate a large number of Ge-Te bonds, but a low contribution from homopolar bonds, thus limiting the probability for $A-A$ or $B-B$ bonds in the rings. In the corresponding crystalline phases, only strictly alternating 4 and 6-membered rings are observed; the latter are due to the intrinsic vacancies in the Ge/Sb sublattice. The authors conclude that alternating $ABAB$ rings are an important building

block in the amorphous as well as in the crystalline phase, thus facilitating the phase change process. The growing fraction of 4- and 6-membered rings along the pseudo-binary-line is supposed to explain the shorter crystallization times of the Sb_2Te_3-rich compositions. It may, however, already be pointed out that new AIMD results on GeTe question this finding to some degree. Details of this finding are discussed in section 5.2.5.

Ring statistics calculated from the AXS/RMC configurations are illustrated in fig. 56. The findings are very different from both of the studies described previously. Germanium telluride shows a strong preference for 5- and 6-membered rings. This preference is reduced, but still visible in GST-8,2,11, and nearly disappeared in GST-2,2,5, for which a largely uniform distribution is observed. As shown in e.g. by Kohara et al. [94], we may identify a high degree of preference for a given n-membered ring with a high degree of (topological) intermediate range order; it may thus be stated that the IRO with regard to the ring statistics decreases significantly from GeTe to GST-8,2,11, and then somewhat more to GST-2,2,5. Interestingly, this is the same trend that has also been observed in the FSDP of Ge-Ge. Contrary to other studies [82–84], neither a dominant contribution from even-membered structures for high Sb_2Te_3 concentrations nor a significant percentage of alternating $ABAB$ rings to the overall distribution can be found. The latter contribution is comparably small in general, and even decreases from GeTe via GST-8,2,11 to GST-2,2,5.

The current results suggest a higher topological order for GST-1,4,7, where the ring distribution becomes more ordered again. It should be noted, however, that these statistics are affected by the actual configurations around each element and need to be confirmed by a simulation with a full set of differential structure factors.

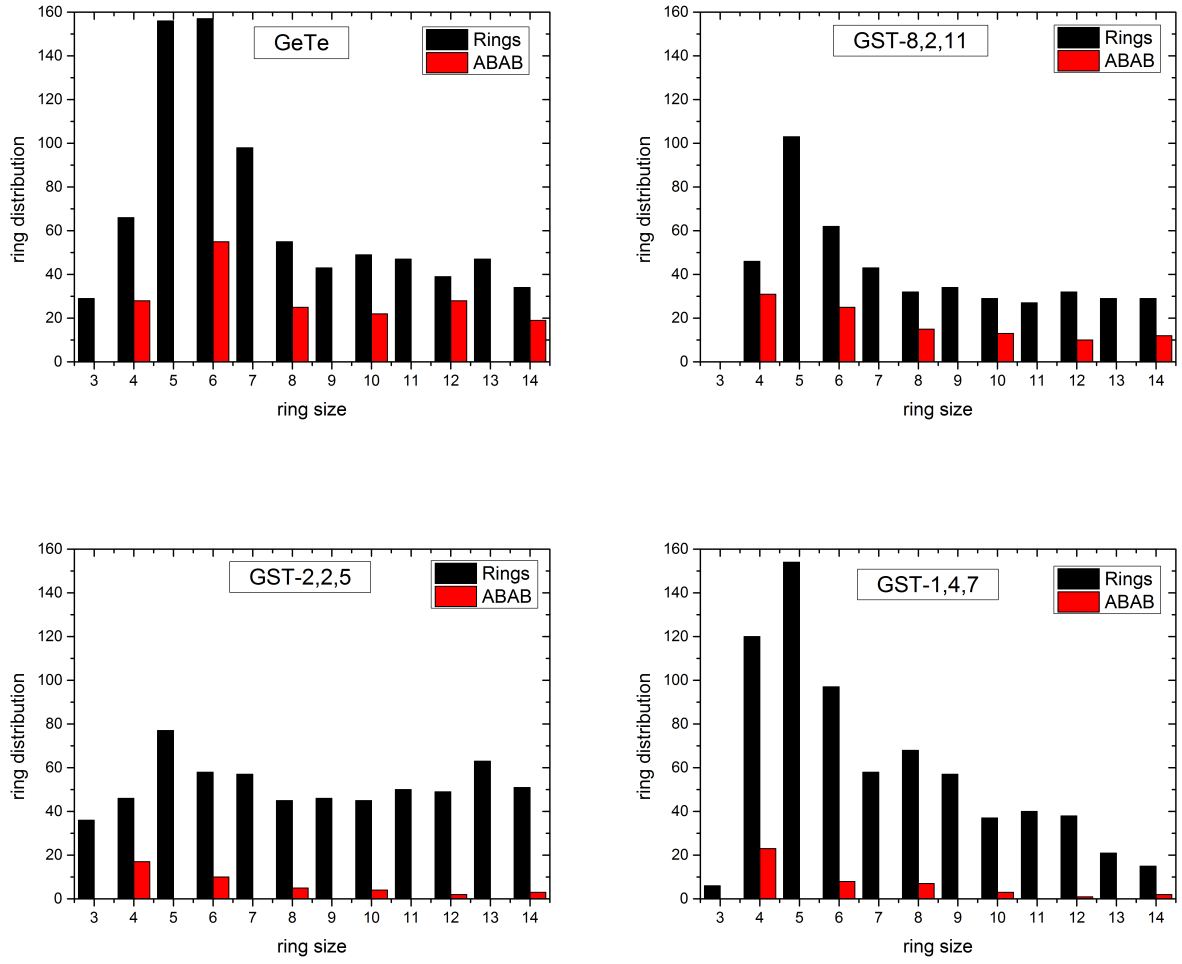

Figure 56: Distribution of irreducible ring structures in GST glasses. Black: number of n-membered rings, red: contribution of alternating $ABAB$ rings (A: Ge, Sb; B: Te). Note that the distribution for GST-1,4,7 may not be as reliable as the others due to the missing dataset of the Ge-related contributions during the RMC modelling.

5.2.5 Comparison with AIMD results

The previous considerations showed that there are some discrepancies between the experimental and the theoretical approaches concerning the structural characterization of the GST glasses. In general, it is found that theoretical methods under-estimate the contribution of homopolar bonds, and interatomic distances are over-estimated compared to the experimental values, especially in the case of the Ge-Te bond. In order to examine these differences, an *ab-initio* molecular dynamics simulation has been performed for the binary composition GeTe. The obtained results are particularly useful to compare the structural properties in reciprocal space, which are not always reported explicitly in the corresponding literature. However, the (partial) structure factors are generally thought of as being especially sensible to subtle structural changes, so that a direct comparison can prove insightful. For example, the order on a length scale larger than the SRO is difficult to visualize from the $g(r)$ data, but may have a direct manifestation in the $S(Q)$'s (e.g. as a FSDP).

The obtained pair correlation functions and the structure factors calculated by Fourier transformation are displayed in fig. 57. An excellent agreement of the AIMD-$g_{ij}(r)$'s is found with comparable simulations by Akola and Jones [83]. A major difference results from the application of a dispersion correction in the DFT scheme (which has not been used in ref. [83]) with an impact on the second coordination sphere of the Ge-Te correlation (see below).

Comparing the (partial) pair correlation functions obtained from AIMD and from the AXS/RMC approach, it can be stated that

- the total $g(r)$'s show major disagreements. The position of the first peak is shifted to larger distances by about 0.1 Å and coordination numbers obtained from the corresponding radial distribution functions differ significantly. The coordination numbers from AIMD are close to those of the study from Akola and Jones and can therefore be taken from table 14.

- The Te-Te pair correlation, on the other hand, is modelled reasonably well, though a somewhat smaller CN (0.1 compared to 0.3 by AXS) is predicted.

- In g_{GeTe}, the first peak is modelled reasonably concerning its shape, but it is shifted by 0.1 Å to higher distances, thus leading to an increased coordination number of about

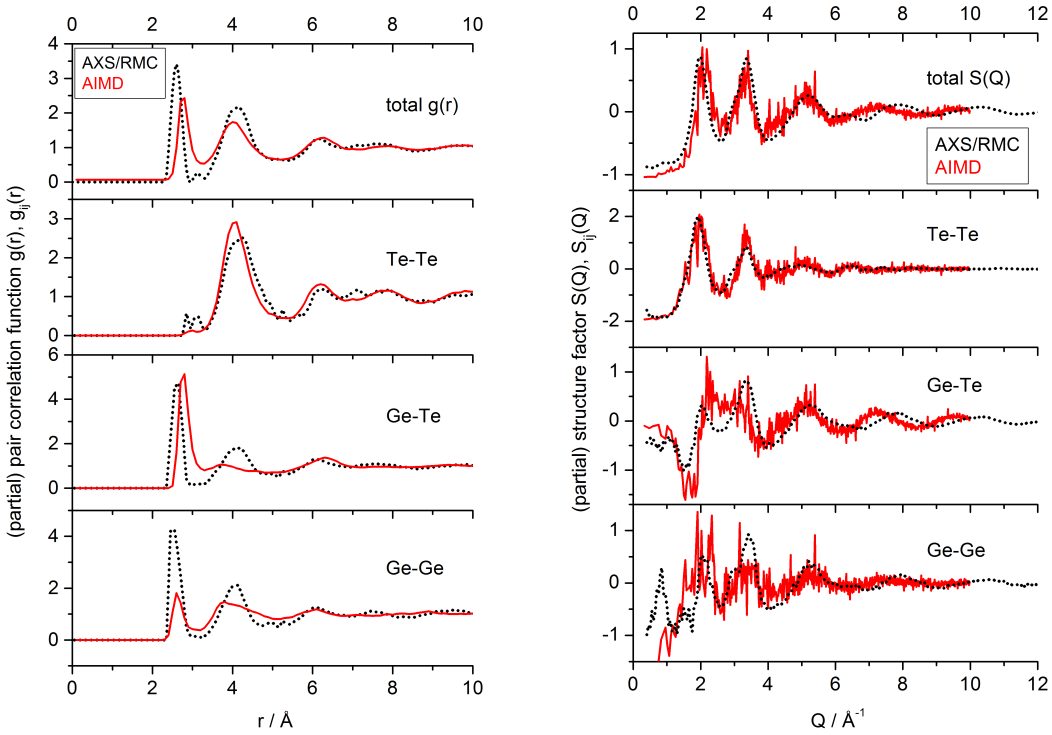

Figure 57: Partial pair correlation functions (left) and structure factors (right) obtained from AIMD (red) in comparison with experimental results (black).

3.2. The second coordination sphere is represented bad in AIMD, though the overall CN, i.e. the integral of the corresponding RDF up to the minimum beyond the second peak at 4.6 Å, agrees well. It can be concluded that the second coordination sphere is heavily smeared out over the entire range. The third peak, however, is modelled surprisingly well as compared to the experimental graph.

- A bad fit again is found for the pair Ge-Ge. The positions of the peaks agree roughly, but the coordination numbers of the first and second peak are highly underestimated.

Similar trends are observed when comparing the structure factors in fig. 57 (right hand side). Note that the comparably bad resolution is owing to the Fourier transformation of the limited simulation box of only a few hundred atoms.

- In the total $S(Q)$, experimental and theoretical data agree well concerning the second and third peak position. A bad agreement, however, is found with the FSDP, and furthermore a shift of the period of the oscillations is visible in the high-Q region.

- The Te-Te correlations show a very good agreement. Additionally, there is no indication of the deviating periods, which are observed in the total $S(Q)$ for high Q values.

- The agreement for Ge-Te is less good. Though the low-Q behaviour is modelled reasonably (i.e. the high intensities at the lowest Q values and the dip between 1 and 2 $Å^{-1}$), a smearing of the Q_2 and Q_3 peaks is observed as well as the shift of the period of the oscillations for higher Q-values.

- The different methods agree quite badly for the Ge-Ge correlation. The FSDP is completely neglected by DFT, other peaks are badly represented, and in addition, the disagreeing behaviour in the high-Q region is indicated as well.

To summarize, there are large discrepancies between the experimental and the theoretical approach. On the one hand, the poor representation of the FSDP in the Ge-Ge correlation by AIMD is not surprising, since the length of the simulation box is only about 13 Å, so that an order on an intermediate or extended length scale cannot be modelled adequately. On the other hand, the deviations concerning the short-range order result in substantially different configurations. Given only the partial functions $g_{ij}(r)$ and $S_{ij}(Q)$, it would be difficult to argue which structure is closer to the "real" glass, as on the one hand, the parameters of the DFT simulation might not be well suited to describe the amorphous structure, but on the other hand, the partial functions obtained from the RMC scheme might also be biased by the applied constraints. However, the disagreement of the AIMD model in the total $S(Q)$, especially the shift of the period of the oscillations for higher Q values, reveals that the former case is more likely, since $S(Q)$ represents direct experimental data. Since the same characteristic is also found in other theoretical investigations and contradicts the AXS/RMC as well as EXAFS results, further development of the MD method appears to be needed before the structures can be adequately compared.

Nonetheless, it can be shown that a dispersion correction can improve the agreement with the experimental data to some extent, as it has a considerable impact on the second coordination sphere in the Ge-Te correlation. This influence is illustrated in fig. 58, which compares all correlations in GeTe for the AIMD simulations with and without the dispersion correction. The influence on the homoatomar correlations appears to be marginal, whereas no peak is observed in Ge-Te at 3.7 Å without this correction. The right hand side of the figure illustrates again in detail the latter correlation as obtained by the different approaches. The effect of the dispersion correction on the first coordination sphere

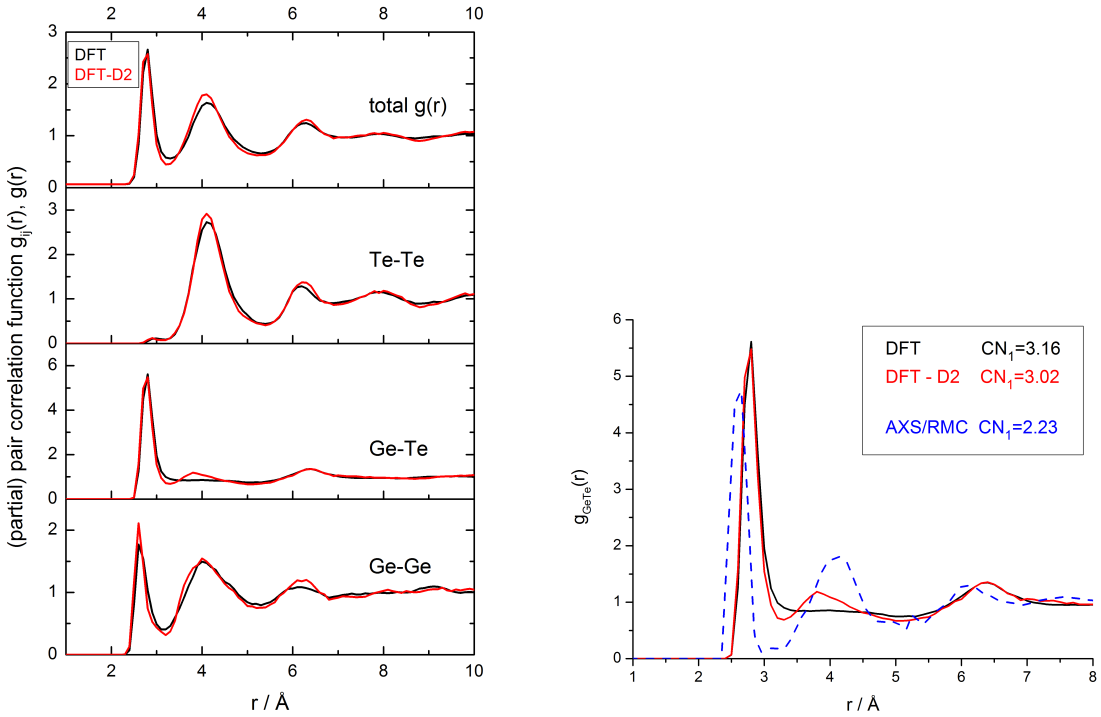

Figure 58: Left: Partial pair correlation functions from AIMD with (red curves) and without dispersion correction (black curves), right: detailed comparison for the Ge-Te correlation (experimental data as blue dashed line). Annotated are the individual coordination numbers of the first coordination sphere of Ge-Te.

is small and only visible in a slight decrease of the coordination number from n_{GeTe}=3.16 to n_{GeTe}=3.02, which still remains considerably higher than the experimental value of 2.23. The effect on the second coordination sphere is larger, though the agreement with the experimental data is still unsatisfactory. However, such a feature has an important effect e.g. on the distribution of ring structures, as illustrated fig. 59. It is observed that the results for the DFT simulation without dispersion correction agree well with the ring statistics reported by Akola and Jones (the data were taken from ref. [84]). The introduction of the dispersion correction somewhat increases the topological order as shown in fig. 59 c), but the effect is not large enough to reproduce the statistics obtained by AXS/RMC, shown in fig. 59 a).

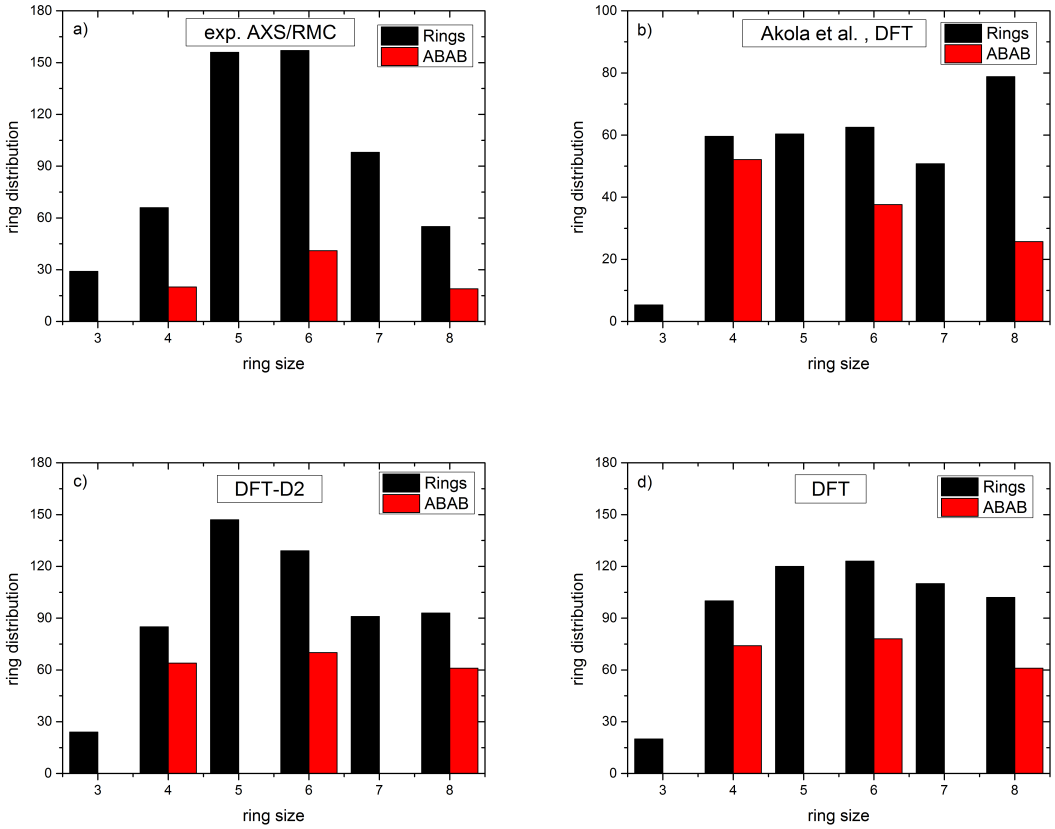

Figure 59: Comparison of the distribution of irreducible ring structures in GeTe by experimental and theoretical approaches. a) Section of the ring statistics from fig. 56, b) ring statistics by Akola and Jones taken from ref. [84], in comparison with ring statistics from the AIMD simulation with (c) and without dispersion correction (d).

5.3 Impact of the structure on the phase change properties

The following section gives a recapitulatory discussion and provides possible interpretations of the data presented for the GeSbTe glasses. Thereby, the relationships between the short- and intermediate range order characteristics and the PCM properties are elucidated, such as the optical contrast, the crystallization time and the temperatures of the glass transition and of the crystallization. The IRO is an important parameter governing these features; prior to the further considerations, it should therefore be noted that the discussion of the IRO in the GeSbTe system may have been suggestive to conclude that the IRO is largely dependent on the relative content of a given element (e.g. the FSDP in the Ge-Ge versus the FSDP in the Sb-Te correlation). However, this is not necessarily true, as demonstrated by a short comparison with the AgGeSe glasses in the previous chapter. The opposite trend is observed in these compounds, namely that the Ag-based FSDPs decrease from Ag4 to Ag20, although the Ag content is increasing.

5.3.1 Temperature of the glass transition and crystallization

The structural data gathered by the RMC modelling can be used to gain insight into the development of the glass transition temperature T_g and the crystallization temperature T_c in the system $(GeTe)_{1-x}(Sb_2Te_3)_x$. The glass transition temperature (or simply "glass temperature") marks a transition from a rigid to a floppy, ductile structure and is a measure for the thermal stability of the amorphous phase. Below T_g, the amorphous structure is "frozen", i.e. atomic mobilities are very low and the structure is rigid. Above T_g, structural reorganization is possible, though the atomic mobility is not necessarily large enough to adopt the energetic minimum structure (i.e. the crystal). However, most amorphous materials crystallize readily at a temperature T_c not very high above the glass temperature. Thus, both parameters are used for describing the glass forming ability (GFA) of a given compound. See for example the study by Li et al. for a discussion of the various methods to define the GFA [95].

Lankhorst provides a model to calculate T_g from enthalpies of atomisation, with special regard to phase change materials [96]. The values calculated by this model are displayed in fig. 60, and agree fairly well with measured T_g values, e.g. by Morales-Sánchez et al., who report the glass temperature of GST-2,2,5 to be about 100°C [97]. Values for T_c

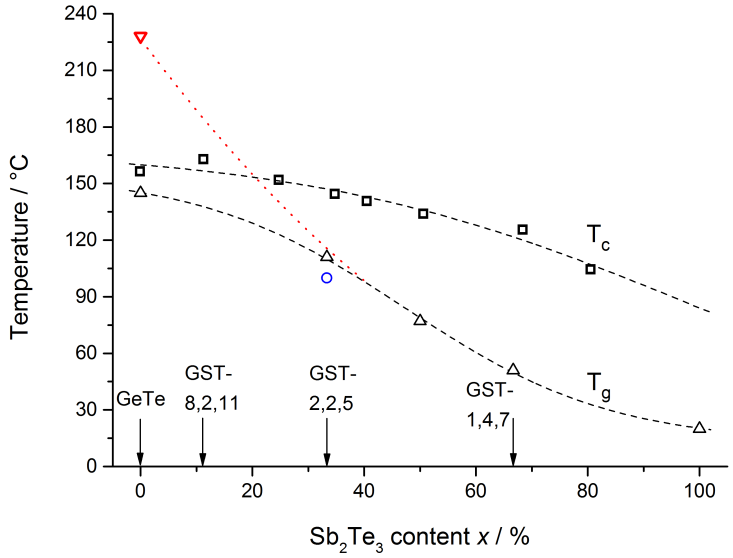

Figure 60: Temperature of the glass transition T_g (triangles) [96] and crystallization T_c (squares) [71] in GeTe-Sb_2Te_3. Dashed lines are a guide for the eye. The red dotted line is an extrapolation to the T_g value predicted by the Lankhorst model, and the blue circle indicates a measurement of T_g by Morales-Sánchez et al. [97].

are reported by Yamada et al., measured by differential scanning calorimetry [71]. It is readily observed that the glass temperature for GeTe predicted by Lankhorsts simple model (red triangle at 228°C) is high above the crystallization temperature. Based on DSC measurements, however, a value of about 145°C, i.e. only a few degrees below T_C, is more realistic. These values also give an indication why the Sb_2Te_3 sample exhibited a spontaneous crystallization during the sputtering process, as the material may have been heated up above T_g due to the temperature of the Argon plasma.

T_g and T_C are generally thought to be closely connected to the average coordination number $\langle N \rangle$. Materials with a high value for $\langle N \rangle$ usually possess a high T_g and are more "rigid" than compounds with lower $\langle N \rangle$. More specifically, the mean-field constraint theory [98, 99] relates $\langle N \rangle$ to the rigidity of a given glass, and predicts a "topological threshold" of $\langle N \rangle = 2.4$, where the character of the glass undergoes a transition from a floppy to a rigid structure. Since the lowest value for the average coordination number along the pseudo-binary line was 2.87 for GST-1,4,7, all examined compositions belong to this rigid region. However, within the short-range order, not only the number of bonds, but also the bond strength is important to characterize the transition temperatures. In the following, we may consider these quantities more closely based on the data presented in this work:

Above T_g, weak cohesive forces in the material can be overcome, such as structural constraints given by the IRO or weak covalent bonds. And above T_c, also tight constraints given by the stronger bonds are surmounted and considerable structural reorganization takes place, i.e. the transition to a thermodynamically more stable phase. Following the reasoning of Kolobov et al. [74], the temperatures of crystallization of the "pure" phases as well as their melting temperatures T_m can be taken as a measure for the strength of a bond. This consideration gives the following order of bond strengths (from weak to strong):

Te-Te:	T_c(a-Te)=30°C,	T_m(Te)=425°C	[74]
Sb-Sb:	T_c(a-Sb)=20°C-80°C,	T_m(Sb)=630°C	[100]
Sb-Te:	T_c(a-Sb_2Te_3)= 100°C,	T_m(Sb_2Te_3)=630°C	[71]
Ge-Te:	T_c(a-GeTe)=129°C-150°C,	T_m(GeTe)=725°C	[71, 74]
Ge-Sb:	T_c(a-$Ge_{15}Sb_{85}$)=230°C,	T_m($Ge_{15}Sb_{85}$)=592°C	[101]
Ge-Ge:	T_c(a-Ge)=450°C,	T_m(Ge)=938°C	[74]

Of course, the binary phases GeTe, $Ge_{15}Sb_{85}$ and Sb_2Te_3 are not an unambiguous measure for the heteroatomar bonds, since they contain a certain contribution of homoatomar bonds; but since the Ge-Te, Ge-Sb and Sb-Te contributions are supposed to be dominant, the qualitative order may still be valid. For the binary system Ge-Sb, only transition temperatures for the eutectic composition $Ge_{15}Sb_{85}$ could be found, explaining the low melting temperature.

The short range order characteristics based on the coordination numbers from tab. 12 and the qualitative order of bond strength provide a reasonable model to describe the development of the crystallization temperature T_c. This temperature decreases more softly than T_g, but nonetheless it declines more strongly than expected from the soft reduction of the average coordination numbers, which decrease from $\langle N \rangle = 3.16$ in GeTe by a value of 0.29 to $\langle N \rangle = 2.87$ in GST-1,4,7. From measurements of the total structure factors only, this development is not recognizable (see section 5.1.2). In contrast, the $8-N$ rule would predict a reduction by a much higher value of 0.5, which is not observed. The main effect on the development of T_c is therefore not the reduction of the number of bonds, but it is rather related to the nature of the bonds. The most stable bonds are Ge correlations, which are reduced significantly with the loss of Ge atoms along the pseudo-binary line (50% in GeTe to about 8% in GST-1,4,7).

The development of T_g shown in fig. 60, on the other hand, can be explained by taking into account the IRO characteristics described in sec. 5.2.4. Recalling the theories on the IRO described by Elliott [24, 28] and Uchino [25] (see sec. 2.4), we may consider the occurrence of a first sharp diffraction peak around 1 $Å^{-1}$ as a sign for intermediate range order in the amorphous phase. The FSDP in the GST glasses is seen already in the experimentally accessible differential structure factors and it is quantified by RMC modelling in the partial $S(Q)$'s shown in fig. 47. The development is observed most pronounced in the Ge-Ge correlation, where the FSDP decreases steeply as a function of the Sb_2Te_3 content. The real-space counterpart of the Ge-Ge FSDP is illustrated as the Ge network in fig. 53. Thereby, it is seen that the strong intermediate Ge-Ge network as well as the Ge-Te network fragment rapidly along the pseudo-binary line. The remaining weaker correlations can already be broken at lower temperatures, thus causing the steep decline of T_g. Antimony and tellurium related correlations can only partly compensate for the overall loss of bonding strength by forming an intermediate range Sb-Te network and an increasing number of Sb-Te bonds.

It may be noted that a similar trend is observed in the binary Ge_xSe_{1-x} glasses, which have been investigated between $x = 0.15$ and 0.333 by Hosokawa et al. using the AXS/RMC method [63]. These glasses are found to adhere strictly to the $8 - N$ rule, resulting in a largely increasing $\langle N \rangle$ as a function of x, with a so-called "stiffness transition" at the critical composition $x = 0.20$, for which $\langle N \rangle = 2.4$. In addition, a growth of the FSDP at 1 $Å^{-1}$ is observed in the total structure factors. Employing the AXS/RMC technique, it can be shown that this FSDP is mainly related to the Ge-Ge and also to the Ge-Se correlation. Both contributions to the FSDP decrease with decreasing amount of Ge. Furthermore, the Ge-Se correlation exhibits very similar low-Q features as the Ge-Te correlation in the GeSbTe glasses. These developments suggest that the formation of a strong background network of the Ge-Ge and Ge-Chalcogenide correlations, which contributes to the rigidity of the glasses, can be regarded as a general rule in chalcogenide glasses.

5.3.2 The optical contrast in GST

The optical contrast of a phase-change material is defined as the difference in reflectivity between the two involved phases. A high contrast is desirable, as the different amorphous or crystalline "bits" e.g. on a DVD surface can be distinguished better and thus they can be moved closer together. Indirectly, this property thereby controls the amount of data that can be written on a given surface, and it is a factor that contributes to the superior performance of the Blu-ray Disk (using $Ge_8Sb_2Te_{11}$) versus the DVD (using $Ge_2Sb_2Te_5$). It is well known that the optical contrast decreases along the pseudo-binary line from GeTe to Sb_2Te_3, so that generally compositions with a high GeTe content exhibit a superior performance as far as this property is concerned. The discussion of this phenomenon is usually based on the optical dielectric constants ε_∞, which are reported e.g. by Shportko et al. for various GeSbTe materials, among them the *tie*-line compositions GeTe and GST-2,2,5 [102], which are listed in table 18. The increase of ε_∞ from the amorphous to the crystalline phase is a measure for the optical contrast in these compounds. Also listed in table 18 are the ε_∞ values for elemental germanium and tellurium.

In agreement with Yamada et al. [71], Shportko et al. report a decreasing optical contrast between the amorphous and crystalline phase along the pseudo-binary line. The given ε_∞ values indicate, however, that the optical permittivity of the crystalline phases of GST remains constant irrespective of the composition; the difference in contrast is solely related to the different ε_∞ values of the amorphous phase. This considerable change in the optical permittivity of about 21% within the amorphous state is actually completely uncomprehended at present.

The large difference in the optical dielectric constants between the amorphous and crystalline phase, on the other hand, is well studied, and has been explained by Huang and Robertson via a loss of medium-range order: In the crystal, *p*-orbitals can align between different layers and thus form a "resonantly bonded" structure (see [103] and [104] for further details). In the case of a GST crystal, these are lone *p*-orbitals of Te, which are able to arrange in linear chains. In an ideal crystal of octahedrally bonded atoms, these *p*-orbital chains can in principle extend over very large distances - however, due to the pronounced lattice distortions in the crystal structure, they are only observed on "medium-range" length scales [102, 103].

Table 18: Experimentally obtained optical dielectric constants ε_∞ of GeSbTe and related elements [102, 103, 105] and their increase in %, which is a measure for the optical contrast of the PCM's. Annotated are the respective crystal structures as *oct* for a distorted octahedral (i.e. rhombohedral or trigonal) and *tet* for a tetrahedral (i.e. diamond-structure or zincblende) environment, see text.

Compound	ε_∞(Amor.)	ε_∞(Cryst.)	percentage increase
GeTe [102]	13.2	33.2^{oct}	152%
GST-2,2,5 [102]	16.0	33.3^{oct}	108%
Te [103]	11	33.4^{oct}	
Ge [103, 105]	16.0	16.0^{tet}	
Si [103]	11.6	11.6^{tet}	
GaAs [103]	12	12^{tet}	

At this point, a comparison with the situation in the pure elements Ge and Te is worthwhile. It is well known that Ge adopts the diamond structure in the stable crystal. The local environment does not change dramatically upon amorphization, resulting in a very similar arrangement of about 3.8 Ge atoms (on average), which are tetrahedrally coordinated around a central Ge atom in amorphous Ge [106]. As seen from table 18, ε_∞ does not change at all upon crystallization. Both characteristics (i.e. a tetrahedral environment in the crystal as well as in the amorphous form and a negligible change in the dielectric constant) also apply to elemental silicon or to GaAs (see e.g. [107]). Elemental tellurium, on the other hand, adopts a trigonal crystal structure, which can be rationalized as a distorted octahedral coordination around each Te atom. In this case, the transition to an amorphous state has a rather large impact on the structure, which has recently been analysed by Ikemoto and Miyanaga using EXAFS measurements [93]. They demonstrate that amorphous Te consists of otherwise disordered chains of Te atoms with a coordination number N(Te)=2, compared to a 2+4 distorted octahedral coordination in the crystal. This rearrangement is accompanied again by a pronounced difference in the dielectric constant ε_∞.

To summarize, in the crystalline phase, an octahedral arrangement generally leads to a "resonantly bonded" state, in which p-orbitals can align in linear chains, whereas a tetrahedral arrangement disfavours this kind of bond. Thus, tetrahedral structures in general possess a lower ε_∞ and cannot lose the "resonance bond" contribution upon amorphization. Generalizing the theory by Huang and Robertson, it is possible to discuss the development of the optical contrast along the pseudo-binary line in the GST glasses:

The crystalline phases all adopt a distorted rocksalt structure (in the meta-stable state that is involved in the phase-change process) and thus exhibit a similar degree of IRO, resulting in very similar values for ε_∞. Upon amorphization, a large degree of IRO is lost, explaining the large optical contrast in general. However, there are pronounced differences for the IRO in the amorphous structures for the different compositions, which cause the compositional dependence of ε_∞. More specifically, as shown in section 5.2.4, the character of the underlying network in the amorphous phase shifts from a wide-meshed (i.e. a more tetrahedral) type to a close-meshed (i.e. a more octahedral) type with increasing amount of Sb_2Te_3 (see figs. 53-55). The "octahedral" network on the intermediate length level can be interpreted as being responsible in a similar way for the remaining (increasing) optical permittivity.

It is easily explained why this effect has not yet attracted attention in comparable investigations. Experiments on the structure of GST's have usually been focused on the EXAFS technique, which cannot probe the IRO, or on total XRD, which gives no element specific information and thus provides only an average over all structure factors. Theoretical methods like AIMD in general fail to describe the IRO adequately, also because the systems under consideration are too small to give reliable results on the corresponding length scale. AXS, on the other hand, is well suited to reveal the compositional dependence of the IRO and thereby to explain the decreasing optical contrast along the pseudo-binary line GeTe-Sb_2Te_3.

5.3.3 Crystallization time

The time that is needed for crystallizing an amorphous spot and vice versa is the most important property to enable reasonable fast data writing and erasing cycles. The actual crystallization time τ_{cryst} can be influenced by the measurement conditions, but a significant reduction of τ_{cryst} along the *tie*-line is consistently observed for the same method. Yamada and coworkers report values for τ_{cryst} between 100 ns for GeTe and 30 ns for the Sb_2Te_3-richest compositions. As outlined above, possible models aiming to explain the fast phase change process are the (modified) umbrella-flip model [75, 88] or the ring statistics analogy [82]. As discussed in sec. 5.2.4, experimental as well as theoretical models based ring statistics so far intrinsically lack information on the (element specific) intermediate range order, and conclusions on the ring statistics may therefore be ambiguous.

The current AXS/RMC results cast a quite different light on the interpretation of the crystallization process. In part, the same reasoning as given in sections 5.3.1 and 5.3.2 is applicable, that is that the weaker bonds in the Sb_2Te_3-rich compositions can be broken more easily, thus facilitating the phase-change process. With respect to the IRO, however, special attention should be laid on the development of the "wide-meshed" versus the "close-meshed" network based on the Ge-Te bonds, shown in the bond angle distributions in section 5.2.3 (fig. 50 and 51) and in the network structures in section 5.2.4 (figs. 53-55). The close-meshed contribution, which has a closer resemblance to the crystal structure (where only octahedral bond angles are found), dominates the Sb_2Te_3-rich compositions. Furthermore, for higher Sb_2Te_3 contents, the coordination number of the comparably strong Ge-Te correlation is near 3, preforming half of the 3+3 coordination found in the crystal. In addition, the number of the strong homopolar Ge-Ge bonds, which are absent in the crystal, decreases strongly.

The ring statistics calculated in section 5.2.4 fit well into the picture. A comparably high topological order is found in the GeTe-rich compositions. This order, however, is markedly different from that of the crystal. The pure crystalline GeTe is composed nearly entirely of 4-fold rings, and the Sb_2Te_3-richer GST-2,2,5 consists of 4- and 6-membered rings [82]. The ring statistics of the amorphous compounds calculated within the AXS/RMC approach, on the other hand, show high contributions from all ring sizes, but most prominently from 5- and 6-fold rings. Unlike proposed by Kohara et al. [82] and by Akola and Jones [83, 84], a dominant fraction of alternating $ABAB$ rings could not be reproduced in the current configurations. This may be attributed to the fact that homopolar bonds have been excluded in ref. [82] and are underestimated in ref. [83, 84]. However, the pronounced difference of these IRO parameters compared to the crystal implies that considerable structural reorganization is necessary. Starting from less ordered configurations, as the one obtained for GST-2,2,5, may therefore accelerate the phase-change process.

In other words, Sb_2Te_3-rich compositions are structurally closer to the crystal in terms of the SRO and the network structure, and they are less dissimilar from the crystal in terms of the distribution of irreducible rings. In combination, these features appear to be the main reason for the considerable reduction of τ_{cryst} as a function of the Sb_2Te_3 content.

6 Summary and outlook

This dissertation explores the nanoscopic structures of the amorphous pseudo-binary systems Ag-$GeSe_3$ and GeTe-Sb_2Te_3 via an approach of anomalous x-ray scattering coupled with Reverse Monte Carlo modelling. It is demonstrated that the AXS/RMC method can reveal structural features of the amorphous system that are invisible or difficult to perceive by other comparable methods. The first part therefore outlines the theoretical and experimental basis for this approach. Thereby, it is shown that the method itself can be improved by a detailed investigation of the problems during the experimental alignment, with special regard to the analyzer crystal used to filter the scattered radiation from the sample. It is demonstrated that the data comprise considerably large systematic errors if this effect remains unaccounted for. Nonetheless, the presented correction schemes can compensate for these errors and should prove useful for future AXS experiments. Also elaborated in the first part is the preparation of the GeSbTe samples, and optimized parameters for the preparation process are given.

The second part presents the two chalcogenide glassy systems and discusses the structures probed by AXS. Some of the presented findings have also been made in previous works of other groups, but they have not been interpreted in a unified framework with respect to the compositional dependence. The AXS/RMC approach provides compelling evidence that the ternary amorphous systems cannot be rationalized by simple models like the $8-N$ rule. In addition, they cannot be regarded as uniform, since major changes in the materials' properties are observed within the same amorphous region in the ternary phase diagram, like the decreasing dielectric constant in GeSbTe or the enormous changes in the ionic conductivity in AgGeSe.

These properties are shown to be closely connected to the near- as well as to the intermediate-range order in the amorphous compounds. By contrasting the low-conducting and the high-conducting phase of the AgGeSe glasses, it is confirmed that the SRO in the latter is characterized by high average coordination numbers around Se and Ag. While this characteristic has already been investigated in previous studies, its impact in the IRO has been neglected. However, it is the IRO that provides the main structural prerequisite for the effect of superionic conductivity of Ag ions in these glasses. The increased Ag-Se interaction in the superionic conducting phase expands the $GeSe_4$

network. Concomitantly, Ag atoms form cluster-like configurations in the expanded network, thereby destroying the spatially averaged intermediate-range order in the Ag based correlations. These cluster-like configurations can be regarded as preforming the nano-pathways which are developing in the "metallized" cells of a programmable metallization cell and act as percolation pathways for the conduction of Ag ions.

The IRO also represents the dominant contribution to explain the excellent phase change abilities of the GeSbTe system. The underlying network structure, which is mainly established by the Ge atoms, weakens with increasing content of Sb_2Te_3, thereby increasing the structural similarity to the meta-stable crystal that is involved in the phase-change process. At the same time, this development controls phase-change characteristics like the optical contrast, the glass transition temperature and the speed of the crystallization. In any case, the presented results clearly show that simple models, which basically consider only one unit cell of the crystal (like Kolobov's umbrella-flip model) in order to explain the fast phase-change mechanism, do not grasp the full reality of the complex process of the formation of the amorphous phase.

However, the strong Ge-Ge and Ge-Te networks, that are impeding the transition from one phase to the other, appear to be a universal feature of the amorphous phases, as shown by a comparison between the Ag-$GeSe_3$ and GeTe-Sb_2Te_3 glasses. In both cases, the correlation between germanium and the chalcogenide is an important aspect for the formation of the vitreous network. Ge-Chalcogenide bonds dominate the generally four-fold coordination of germanium and essentially exhibit similar characteristics in the low-Q region of the partial structure factors. The absence of the latter feature in the other correlations indicates the special and probably universal significance of the Ge-Chalcogenide background network.

As a perspective for the ongoing work on these systems, further AXS experiments are needed on $Ag_x(GeSe_3)_{1-x}$ glasses with compositions close to the superionic threshold in order to study the nature of the sharp jump in the ionic conductivity. The data for the composition with $x = 0.33$ should be completed by a measurement at the Ge and Se K absorption edge. Furthermore, small-angle scattering experiments are planned in order to address the problem of a phase separation tendency.

In the case of the $(GeTe)_{1-x}(Sb_2Te_3)_x$ glasses, further experiments are necessary for the Ge edge of GST-1,4,7 as well as for Sb_2Te_3. For the latter, a cooling system will most likely be needed during sample preparation as well as during the experiment, considering the low glass temperature and the heat load deposited by x-rays in the region 10-32 keV over experimental times of several hours. Furthermore, the development of the intermediate-range order can be described in a more quantitative fashion by investigating compositions between $x = \frac{1}{9}$ and $x = \frac{1}{3}$ with special regard to the network structure. To clarify the phase-change mechanism, however, experiments beyond measurements of the static structure need to be considered. The investigation of the dynamic structure factor by inelastic scattering experiments may prove especially useful in this respect. Such experiments are already planned within the process of the ongoing research on the GeSbTe materials.

With respect to the investigation of the optical contrast in GeSbTe and its dependence on the ratio of octahedral to tetrahedral structural units, another material class is of major interest. The compound $Ge_1Cu_2Te_3$, which is part of the pseudo-binary GeTe-CuTe system, was recently proposed as a next-generation data storage material, and exhibits the curious feature of a *negative* optical contrast (i.e. the reflectivity of the amorphous phase is larger than that of the crystal) [108–110]. In this material, the crystalline as well as the amorphous phase were found to be dominated by tetrahedral motifs. This system may thus present a suitable test for the models developed in this dissertation. Further AXS experiments on these compositions are in progress.

7 Appendix

Acknowledgements

Das gute Gelingen dieser Doktorarbeit hing nicht zuletzt an einer Vielzahl von Personen, denen ich zu großem Dank verpflichtet bin.

Zuvorderst meinem Doktorvater Wolf-Christian Pilgrim, der mir die Möglichkeit zu dieser Dissertation gab und stets zu jedweder Diskussion bereit stand. Daneben auch für seine Hilfe bei den Experimenten am ESRF und bei der Dateninterpretation, sowie für die generelle Freude an der Physikalischen Chemie, die er wie kein anderer vermitteln kann.

Mein besonderer Dank gilt natürlich auch Dr. Ralf Tonner für die Übernahme des Zweitgutachtens, sowie Prof. Bernd Harbrecht für das Mitwirken in der Prüfungskommission.

Die vielen durchgeführten Experimente wären darüber hinaus nicht möglich gewesen ohne die beständige Unterstützung von Prof. Shinya Hosokawa, der aktiv bei jedem einzelnen Experiment mitwirkte und der mir überhaupt erst einen Einblick in die Welt der AXS-Experimente gegeben hat.

Ein äußerst herzlicher Dank selbstverständlich auch an die ehemaligen wie aktiven Mitglieder unserer Arbeitsgruppe, Daniel Szubrin, Astrid Höhle und Benjamin Klee. Ich habe die gemeinsame Zeit ungemein genossen!

Im Laufe meiner Doktorarbeit am FB Chemie hatte ich zudem die durchaus große Freude, mehrere Studenten bei ihren Bachelorarbeiten oder Vertiefungsprojekten in unserer Arbeitsgruppe zu begleiten, und nicht selten hatten ihre Forschungen Einfluss auf meine eigene Arbeit. Dies waren Daniel Gies, Dorian Müller-Borges, Anne Nierobisch, Thomas Kreuscher, Vivane Heddinga, Stefan Spannenberger und Lars Pescara.

Für die Herstellung der Proben hat sich die Kooperation mit dem Center of Smart Interfaces in Darmstadt als unschätzbar erwiesen, daher möchte ich an dieser Stelle vor allem Bernhard Kaiser und Jürgen Ziegler für die gute Zusammenarbeit danken.

Darüber hinaus sollen natürlich auch meine Freunde und Kommilitonen nicht unerwähnt bleiben. Der Einfachheit halber möchte ich daher jedem danken, der sich damit angesprochen fühlt! Insbesondere aber Markus Hermann, Phil Rosenow und Nicola Reusch für ihre unersetzliche Hilfe bei der Bearbeitung meines Manuskriptes.

My special thanks also goes to Akihide Koura, who is working in the group of Prof. Shimojo in the university of Kumamoto, and who performed the AIMD simulations on GeTe.

The AXS experiments themselves would not have been possible without the professional help of the beamline scientists. At the ESRF in Grenoble, these are Nathalie Boudet, Nils Blanc and Jean-François Bérar, who assisted us more often than not night and day to bring the experiments to a good end.

At SPring-8 in Japan, I have to thank most prominently Shinji Kohara and Hiroo Tajiri, who just recently made the AXS experiments possible at BL35XU. For their help during the long hours of the experiments at SPring-8, I would also like to thank Koji Kimura and Kenji Kamimura.

Curriculum Vitae

Persönliche Angaben

Name:	Jens Rüdiger Stellhorn
Geburtsdatum:	20. Januar 1987
Geburtsort:	Paderborn
Staatsangehörigkeit:	deutsch

Wissenschaftlicher Werdegang

2012-2015	Promotion an der Philipps-Universität Marburg
2010-2012	Studium des Master of Science in Chemie an der Philipps-Universität Marburg Thema der M.Sc.-Arbeit: Anomale Röntgenstreuung am Phasenwechselmaterial GeTe
2007-2010	Studium des Bachelor of Science in Chemie an der Philipps-Universität Marburg Thema der B.Sc.-Arbeit: Bestimmung des Primärstrahlspektrums einer Anlage zur Energiedispersiven Röntgenstreuung

List of Publications

Results and parts this dissertation have been published in peer-reviewed journals, and have been presented at national and international conferences and workshops:

Publications

- Wolf-Christian Pilgrim, Jens R. Stellhorn, Shinya Hosokawa. X-ray and Neutron Scattering techniques for structure determination in disordered materials: Liquids and Glasses. Bunsen-Magazin 3, 131-146 (2013).
- Jens R. Stellhorn, Shinya Hosokawa, Wolf-Christian Pilgrim, Microscopic Structure Analysis in Disordered Materials using Anomalous X-ray Scattering, Z. Phys. Chem. 228(10-12), 1005-1031 (2014).
- J. R. Stellhorn, S. Hosokawa, Y. Kawakita, D. Gies, W.-C. Pilgrim, K. Hayashi, K. Ohoyama, N. Blanc, N. Boudet, Local Structure of Room-Temperature Superionic Ag-GeSe3 glasses, J. Non-Cryst. Solids (2015) 10.1016/j.jnoncrysol.2015.02.027 .
- J. R. Stellhorn, S. Hosokawa, W.-C. Pilgrim, Y. Kawakita, K. Kamimura, K. Kimura, N. Blanc, N. Boudet, Structural Aspects of the Superionic Conduction Mechanism in Ag-GeSe3 Glasses, submitted to Z. Phys. Chem., July 2015.
- J. R. Stellhorn, S. Hosokawa, W.-C. Pilgrim, Short- and intermediate-range order in GeTe, submitted to Phys. Status Solidi B, August 2015.

Conferences and workshops

- ADD 2013, Grenoble, France (Analysis of diffraction data in real space)
  Poster: Determination of Short- and Intermediate Range Atomic Structures in Phase Change Materials via Anomalous X-ray Scattering (J. R. Stellhorn, W.-C. Pilgrim, A. Höhle, S. Hosokawa)
- E\PCOS, September 2013, Berlin, Germany (European Symposium on Phase Change and Ovonic Science)

Poster: Determination of Short- and Intermediate Range Atomic Structures in Amorphous GST-Materials via Anomalous X-ray Scattering (J. R. Stellhorn, W.-C. Pilgrim, A. Höhle, S. Hosokawa)

- LAM-15, September 2013, Beijing, China (15th Liquid and Amorphous Metals Conference)
  Poster: Determination of Short- and Intermediate Range Atomic Structures in Amorphous GST-Materials via Anomalous X-ray Scattering (J. R. Stellhorn, W.-C. Pilgrim, A. Höhle, S. Hosokawa)

- ISKSR 2, May 2014 (2nd International Symposium on Kumamoto Synchrotron Radiation)
  Oral presentation: Exploring Amorphous Structures with Anomalous X-ray Scattering.

- Bunsentagung May 2014, Hamburg, Germany
  Oral presentation: Determination of Short- and Intermediate-Range Structures in Amorphous Solids by Anomalous X-Ray Scattering (J. R. Stellhorn, W.-C. Pilgrim, S. Hosokawa)
  Poster: Short- and Intermediate Range Structures in Amorphous GeSbTe-Materials Studied by Anomalous X-ray Scattering (J. R. Stellhorn, W.-C. Pilgrim, A. Höhle, S. Hosokawa, B. Kaiser)

- ISNOG 2014, Jeju, Korea (International Symposium on Non-Oxide and New Optical Glasses)
  Poster: Local Structure of Room-Temperature Superionic Ag-GeSe3 glasses (S. Hosokawa, J. R. Stellhorn, D. Gies, W.-C. Pilgrim, Y. Kawakita, K. Hayashi, K. Ohoyama, N. Blanc, N. Boudet)

- SNI 2014, September, Bonn, Germany (Deutsche Tagung für Forschung mit Synchrotron-strahlung, Neutronen und Ionenstrahlen an Großgeräten 2014)
  Poster: Determination of Short- and Intermediate-Range Structures in Amorphous Solids by Anomalous X-Ray Scattering (Jens R. Stellhorn, Wolf-Christian Pilgrim, Shinya Hosokawa)

- 588th Heraeus-Seminar “Element Specific Structure Determination in Materials on Nanometer and Sub-Nanometer Scales using modern X-Ray and Neutron Techniques” April 2015, Bad Honnef, Germany

  Oral presentation: Local Structure of Room-Temperature Superionic Ag-$GeSe_3$ glasses Studied by Anomalous X-Ray Scattering (J. R. Stellhorn, W.-C. Pilgrim, S. Hosokawa and Y. Kawakita)

- Bunsentagung May 2015, Bochum, Germany

  Oral presentation: Local Structure of Room-Temperature Superionic Ag-$GeSe_3$ glasses Studied by Anomalous X-Ray Scattering (J. R. Stellhorn, W.-C. Pilgrim, S. Hosokawa and Y. Kawakita)

References

[1] A. Guinier, *X-ray Diffraction in crystals, imperfect crystals, and amorphous bodies*, New York, Dover Pub., **1994**.

[2] J. R. Stellhorn, S. Hosokawa, W.-C. Pilgrim, *Z. Phys. Chem.* **2014**, *228*, 1005–1031.

[3] W.-C. Pilgrim, J. R. Stellhorn, S. Hosokawa, *Bunsenmagazin* **2013**, *15*, 131–146.

[4] H. E. Fischer, A. C. Barnes, P. S. Salmon, *Rep. Prog. Phys.* **2006**, *69*, 233–299.

[5] B. E. Warren, *X-Ray Diffraction*, New York, Dover Pub., **1990**.

[6] P. Debye, *Ann. Phys.* **1915**, *46*, 809–823.

[7] T. E. Faber, J. M. Ziman, *Phil. Mag.* **1965**, *11*, 153.

[8] N. Ashcroft, D. C. Langreth, *Phys. Rev.* **1967**, *156*, 685.

[9] A. B. Bhatia, D. E. Thornton, *Phys. Rev. B.* **1970**, *2*, 3004–3012.

[10] J. Blétry, *Z. Naturforsch.* **1976**, *31 a*, 960–966.

[11] N. E. Cusack, *The Physics of Structurally Disordered Matter*, Hilger, Bristol, **1987**.

[12] F. G. Edwards, J. E. Enderby, R. A. Howe, D. I. Page, *J. Phys. C: Solid State Phys.* **1975**, *8*, 3483.

[13] Y. Waseda, *Novel Application of Anomalous (resonance) X-Ray Scattering for Structural Characterization of Disordered Materials*, Berlin, Springer, **1984**.

[14] D. Waasmaier, A. Kirfel, *Acta Cryst.* **1995**, *A51*, 413–416.

[15] D. T. Cromer, D. Liberman, *J. Chem. Phys.* **1970**, *53*, 1891–1898.

[16] S. Sasaki, *KEK Report* **1989**, 88–14.

[17] P. H. Fuoss, P. Eisenberger, W. K. Warburton, A. Bienenstock, *Phys. Rev. Lett.* **1981**, *46*, 1537.

[18] Y. Waseda, *Anomalous X-ray Scattering for Materials Characterization, Springer Tracts in Modern Physics*, *Vol. 179*, Springer-Verlag, Berlin, Heidelberg, **2002**.

[19] K. F. Ludwig, W. K. Warburton, L. Wilson, A. I. Bienenstock, *J. Chem. Phys.* **1987**, *87*, 604.

[20] R. L. McGreevy, L. Pusztai, *Molec. Simul.* **1988**, *1*, 359–367.

[21] O. Gereben, P. Jóvári, L. Temleitner, L. Pusztai, *Journal of Optoelectronics and Advanced Materials* **2007**, *9*, 3021–3027.

[22] O. Gereben, L. Pusztai, *Journal of Computational Chemistry* **2012**, *33*, 2285–2291.

[23] S. Sato, K. Maruyama, *J. Phys. Condens. Matter* **2013**, *25*, 454208.

[24] S. R. Elliott, *J. Phys. Cond. Matter* **1992**, *4*, 7661–7678.

[25] T. Uchino, J. D. Harrop, S. N. Taraskin, S. R. Elliott, *Phys. Rev. B* **2005**, *71*, 14202.

[26] S. R. Elliott, *Nature* **1991**, *354*, 445–452.

[27] S. R. Elliott, *J. Non-Cryst. Solids* **1995**, *182*, 40–48.

[28] S. R. Elliott in *Properties and Application of Amorphous Materials* (Eds.: M. F. Thorpe, L. Tichý), Kluwer Academic Publishers, **2001**, pp. 1–12.

[29] P. S. Salmon, R. A. Martin, P. E. Mason, G. J. Cuello, *Nature* **2005**, *435*, 75–78.

[30] A. Nierobisch, *Bachelor thesis*, Philipps Universität Marburg, **2012**.

[31] M. Kawasaki, J. Kawamura, Y. Nakamura, M. Aniya, *Solid State Ionics* **1999**, *123*, 259.

[32] N. Ohshima, *J. Appl. Phys.* **1996**, *79*, 8357.

[33] J.-L. Ferrer, J.-P. Simon, J.-F. Bérar, B. Caillot, E. Fanchon, O. Kaïkati, S. Arnaud, M. Guidotti, M. Pirocchia, M. Rotha, *J. Synchrotron Rad.* **1998**, *5*, 1346–1356.

[34] H. Tajiri, Y. Imai, *BL13XU Outline*, http://www.spring8.or.jp/wkg/BL13XU/instrument/lang-en/INS-0000000394/instrument_summary_view, **2014**, last accessed 13.03.2015.

[35] L. Kissel, B. Zhou, S. C. Roy, S. K. S. Gupta, R. H. Pratt, *Acta Cryst. A* **1995**, *51*, 271.

[36] S. Hosokawa, W.-C. Pilgrim, J.-F. Bérar, S. Kohara, *Eur. Phys. J. Special Topics* **2012**, *208*, 291.

[37] G. Goerigk, H.-G. Haubold, O. Lyon, J.-P. Simon, *J. Appl. Cryst.* **2003**, *36*, 425.

[38] B.-K. Teo, *EXAFS: Basic Principles and Data Analysis*, Springer, Berlin, Heidelberg, New York, Tokyo, **1986**.

[39] J. J. Rehr, R. C. Albers, *Rev. Mod. Phys* **2000**, *72*, 621.

[40] W. A. Hendrickson, *Science* **1991**, *254*, 51.

[41] K. Sagel, *Tabellen zur Röntgenstrukturanalyse*, Springer-Verlag, Berlin, Göttingen, Heidelberg, Band VIII, **1958**.

[42] H. H. Paalman, C. J. Pings, *Journal of Applied Physics* **1962**, *33*, 2635–2639.

[43] NIST-Datenbank, http://physics.nist.gov/PhysRefData/FFast/html/form.html, **2015**, last accessed 18.10.2011.

[44] D. T. Cromer, *The Journal of Chemical Physics* **1969**, *50, Nr. 11*, 4857–4859.

[45] P. Eisenberger, P. Platzman, H. Winick, *Phys. Rev. Lett.* **1976**, *36*, 623.

[46] J. Krogh-Moe, *Acta Cryst.* **1956**, *9*, Nr. 11, 951–953.

[47] N. Norman, *Acta Cryst.* **1957**, *10*, 370.

[48] S. L. Roux, P. Jund, *Comp. Mater. Sci.* **2010**, *49*, 70–83.

[49] J. P. Perdew, K. Burke, , M. Ernzerhof, *Phys. Rev. Lett.* **1996**, *77*, 3865.

[50] S. Grimme, *J. Comp. Chem.* **2006**, *27*, 1787.

[51] P. E. Blöchl, *Phys. Rev. B* **1994**, *50*, 17953.

[52] M. Mitkova, Y. Wang, P. Boolchand, *Phys. Rev. Lett.* **1999**, *83*, 3848.

[53] M. Kozicki, M. Mitkova, J. Zhu, M. Park, *Microelectronic Engineering* **2002**, *63*, 155–159.

[54] M. Kozicki, M. Mitkova, M. Park, M. Balakrishnan, C. Gopalan, *Superlattices and Microstructures* **2003**, *34*, 459–465.

[55] G. J. Cuello, *Science in School* **2010**, *15*, 24–28.

[56] A. Piarristeguy, J. M. C. Garrido, M. A. Ureña, M. Fontana, B. Arcondo, *J. Non-Cryst. Solids* **2007**, *353*, 3314–3317.

[57] A. Piarristeguy, M. Mirandou, M. Fontana, B. Arcondo, *J. Non-Cryst. Solids* **2000**, *273*, 30–35.

[58] A. Piarristeguy, M. Fontana, B. Arcondo, *J. Non-Cryst. Solids* **2003**, *332*, 1–10.

[59] G. Cuello, A. Piarristeguy, A. Fernández-Martínez, M. Fontana, A. Pradel, *J. Non-Cryst. Solids* **2007**, *353*, 729–732.

[60] K. Ohara, L. Kumara, Y. Kawakita, S. Kohara, M. Hidaka, S. Takeda, *J. Phys. Soc. Jpn.* **2010**, *79*, Suppl. A 141–144.

[61] L. Kumara, K. Ohara, Y. Kawakita, S. Kohara, P. Jóvári, M. Hidaka, N. E. Sung, B. Beuneu, , S. Takeda, *Eur. Phys. J. Web Conf. LAM14* **2011**, 02007–1–5.

[62] J. R. Stellhorn, S. Hosokawa, Y. Kawakita, D. Gies, W.-C. Pilgrim, K. Hayashi, K. Ohoyama, N. Blanc, N. Boudet, *J. Non-Cryst. Solids* **2015**, *10.1016/j.jnoncrysol.2015.02.027*, year.

[63] S. Hosokawa, I. Oh, M. Sakurai, W.-C. Pilgrim, N. Boudet, J.-F. Bérar, S. Kohara, *Phys. Rev. B* **2011**, *84*, 014201.

[64] R. Suenaga, Y. Kawakita, S. Nakashima, S. Tahara, S. Kohara, S. Takeda, *J. Phys. Conf. Ser.* **2008**, *98*, 012021.

[65] L. Rátkai, I. Kaban, T. Wágner, J. Kolář, S. Valková, I. Voleská, B. Beuneu, P. Jóvári, *J. Phys. Condens. Matter* **2013**, *25*, 454210.

[66] P. Armand, A. Ibanez, H. Dexpert, D. Bittencourt, D. Raoux, E. Philippot, *J. Phys. IV Colloque C2 (2)* **1992**, C2–189.

[67] Y. Wang, M. Mitkova, D. G. Georgiev, S. Mamedov, P. Boolchand, *J. Phys.: Condens. Matter* **2003**, *15*, S1573–S1584.

[68] B. Arcondo, M. Ureña, A. Piarristeguy, A. Pradel, M. Fontana, *Applied Surface Science* **2007**, *254*, 321–324.

[69] A. Piarristeguy, M. Ramonda, A. Ureña, A. Pradel, M. Ribes, *J. Non-Cryst. Solids* **2007**, *353*, 1261–1263.

[70] A. Piarristeguy, M. Ramonda, N. Frolet, M. Ribes, A. Pradel, *Solid State Ionics* **2010**, *181*, 1205–1208.

[71] N. Yamada, E. Ohno, K. Nishiuchi, N. Akahira, M. Takao, *J. Appl. Phys.* **1991**, *69*, 2849.

[72] D. Loke, T. H. Lee, W. J. Wang, L. P. Shi, R. Zhao, Y. C. Yeo, T. C. Chong, S. R. Elliott, *Science* **2012**, *336*, 1566–1569.

[73] N. Yamada, T. Matsunaga, *J. Appl. Phys.* **2000**, *88*, 7020–7028.

[74] A. V. Kolobov, J. Tominaga, P. F. F. Uruga, *Appl. Phys. Lett.* **2003**, *Vol. 82*, 382–384.

[75] A. V. Kolobov, P. Fons, A. I. Frenkel, A. L. Ankudinov, J. Tominaga, T. Uruga, *Nature Mater.* **2004**, *3*, 703–708.

[76] T. Siegrist, P. Merkelbach, M. Wuttig, *Annu. Rev. Condens. Matter Phys* **2012**, *3*, 215–237.

[77] T. Matsunaga, H. Morita, R. Kojima, N. Yamada, K. Kifune, Y. Kubota, Y. Tabata, J.-J. Kim, M. Kobata, E. Ikenaga, K. Kobayashi, *J. Appl. Phys.* **2008**, *103*, 093511.

[78] P. Jóvári, I. Kaban, J. Steiner, B. Beuneu, A. Schöp, A. Webb, *J. Phys.: Condens. Matter* **2007**, *19*, 335212–1–9.

[79] D. A. Baker, M. A. Paesler, G. Lucovsky, S. C. Agarwal, P. C. Taylor, *Phys. Rev. Lett.* **2006**, *96*, 255501–1–3.

[80] D. A. Baker, M. A. Paesler, G. Lucovsky, P. C. Taylor, *J. Non-Cryst. Solids* **2006**, *352*, 1621–1623.

[81] P. Jóvári, I. Kaban, J. Steiner, B. Beuneu, A. Schöp, A. Webb, *Phys. Rev. B* **2008**, *77*, 035202.

[82] S. Kohara, K. Kato, S. Kimura, H. Tanaka, T. Usuki, K. Suzuya, H. Tanaka, Y. Moritomo, T. Matsunaga, N. Yamada, Y. Tanaka, H. Suematsu, M. Takata, *Applied Physics Letters* **2006**, *89(20)*, 201910–1 – 201910–3.

[83] J. Akola, R. O. Jones, *Phys. Rev. B* **2007**, *76*, 235201–1–10.

[84] J. Akola, R. O. Jones, *Physical Review B* **2009**, *79*, 134118.

[85] J. Akola, R. O. Jones, S. Kohara, S. Kimura, K. Kobayashi, M. Takata, T. Matsunaga, R. Kojima, N. Yamada, *Phys. Rev. B* **2009**, *80*, 020201(R)–1–4.

[86] J. Hegedüs, S. R. Elliott, *Nature Mater.* **2008**, *7*, 399–405.

[87] S. Caravati, M. Bernasconi, T. D. Kühne, M. Krack, M. Parrinello, *Appl. Phys. Lett.* **2007**, *91*, 171906–1–3.

[88] S. Hosokawa, W.-C. Pilgrim, A. Höhle, D. Szubrin, N. Boudet, J.-F. Bérar, K. Maruyama, *J. Appl. Phys.* **2012**, *111*, 083517.

[89] P. Jóvári, *J. Phys. Cond. Matter* **2013**, *25*, 195401.

[90] P. Pyykkö, *Physical Review B* **2012**, *85*, 024115.

[91] J. M. van Eijk, PhD thesis, RWTH Aachen, **2010**.

[92] K. Ohara, L. Temleitner, K. Sugimoto, S. Kohara, T. Matsunaga, L. Pusztai, M. Itou, H. Ohsumi, R. Kojima, N. Yamada, T. Usuki, A. Fujiwara, M. Takata, *Advanced Functional Materials* **2012**, *22*, 2251–2257.

[93] H. Ikemoto, T. Miyanaga, *J. Synchrotron Rad.* **2014**, *21*, 409–412.

[94] S. Kohara, J. Akola, H. Morita, K. Suzuya, J. K. R. Weber, M. C. Wilding, C. J. Benmore, *PNAS* **2011**, *108*, 14780–14785.

[95] Y. Li, S. Ng, C. Ong, H. Hng, T. Gob, *Scripta Materialia* **1991**, *36*, 783–787.

[96] M. H. R. Lankhorst, *J. Non-Cryst. Solids* **2002**, *297*, 210–219.

[97] E. Morales-Sánchez, E. F. Prokhorov, A. Mendoza-Galván, J. González-Hernández, *J. Appl. Phys.* **2002**, *91*, 697–702.

[98] J. C. Phillips, *J. Non-Cryst. Solids* **1979**, *34*, 153–181.

[99] F. Thorpe, *J. Non-Cryst. Solids* **1983**, *57*, 355–370.

[100] M. Hashimoto, H. Sugibuchi, K. Kambe, *Thin Solid Films* **1987**, *98*, 197–201.

[101] S. Raoux, J. L. Jordan-Sweet, A. J. Kellock, *J. Appl. Phys.* **2008**, *103*, 114310.

[102] K. Shportko, S. Kremers, M. Woda, D. Lencer, J. Robertson, M. Wuttig, *Nat. Mater.* **2008**, *7*, 653–658.

[103] B. Huang, J. Robertson, *Phys. Rev. B* **2010**, *81*, 081204(R)–1–4.

[104] M. Wuttig, N. Yamada, *Nature Materials* **2007**, *6*, 824–832.

[105] T. M. Donovan, E. Spicer, J. M. Bennett, E. J. Ashley, *Phys. Rev. B* **1970**, *2*, 397–413.

[106] W. Paul, G. Connell, R. Temkin, *Advances in Physics* **1973**, *22*, 531–580.

[107] C. Molteni, L. Colombo, L. Miglio, *Phys. Rev. B* **1994**, *50*, 4371–4377.

[108] Y. Saito, Y. Sutou, J. Koike, *J. Phys. Chem. C* **2014**, *118*, 26973.

[109] P. Jóvári, Y. Sutou, I. Kaban, Y. Saito, J. Koike, *Scr. Mater.* **2013**, *68*, 122–125.

[110] T. Kamada, Y. Sutou, M. Sumiya, Y. Saito, J. Koike, *Thin Solid Films* **2012**, *520*, 4389–4393.